Tatiana Arocha' "Climate Crisis"

TU Delft

Electrowetting-Induced Interfacial Behavior in Nanopores: A Molecular Dynamics Study of CO_2 and Ion Distribution at the Triple-Phase Boundary

by

Aniket Pramod Patil

To obtain the degree of Master of Science
at Delft University of Technology
to be defended publicly on Wednesday August 27th, 2025 at 01:00 PM

Student number:	6028276	
Project duration:	December 5, 2024 – August 26, 2025	
Thesis committee:	Dr.ir. R.M. (Remco) Hartkamp	TU Delft, Supervisor
	Prof.dr.ir. J.T. (Johan) Padding	TU Delft
	Prof.dr. R. (Rene) Pecnik	TU Delft
	Ir. M.F.H. (Fathaah) Ansarul Huq	TU Delft

Acknowledgements

I am deeply grateful to my parents and family for their unwavering patience, support, and encouragement throughout my academic journey. Their faith in my abilities has been a constant source of strength, especially in moments of difficulty, and their belief in me has inspired me to keep pushing forward. I also owe a heartfelt thanks to my friends, whose companionship and encouragement have kept me motivated and grounded over the years. Their presence has made this journey not only productive but also far more enjoyable.

I would like to express my heartfelt gratitude to my supervisor, Dr. Remco Hartkamp, for his invaluable guidance, insightful feedback, and unwavering support throughout this thesis. His readiness to help at any time, and his quick and constructive responses, have been a tremendous source of motivation and clarity in my work. I am equally grateful to Fathaah Ansarul Huq, whose help extended beyond technical matters. His advice, both from a technical perspective and from a student's point of view, provided me with essential insights and encouragement throughout this journey. I would also like to sincerely thank Dr. Johan Padding for his support and constructive feedback during our weekly meetings, which significantly contributed to improving the quality and direction of my research.

I am also very thankful to all the instructors of the Section of Energy, Flow and Process Technology at TU Delft for providing me with the necessary resources for my study and fostering a stimulating academic environment.

The assistance of AI language models for code debugging, clarifying concepts, and drafting outlines is also gratefully acknowledged.

Lastly, I extend my thanks to all those who have supported my work, whether directly or indirectly. Your encouragement, guidance, and help have contributed greatly to the successful completion of this thesis.

Aniket Pramod Patil
Delft, August 2025

Abstract

Electrochemical conversion of CO_2 in electrolyzers is a promising pathway toward sustainable fuel and chemical production. A central component of many electrolyzer designs is the gas diffusion electrode (GDE), which enables efficient delivery of gaseous CO_2 to the catalyst surface. However, understanding the local reaction environment within gas diffusion electrodes (GDEs) remains a major challenge, as nanoscale species organization is difficult to access experimentally. Yet, these confined interfacial regions play a crucial role in governing the performance of electrochemical CO_2 reduction (CO_2RR) systems. In particular, how CO_2 and ions behave near complex solid–liquid–gas interfaces under applied potential remains an open question, especially within confined pores just a few nanometers wide (≈ 6 nm), where continuum models no longer hold. This thesis addresses that challenge using all-atom molecular dynamics (MD) simulations to explicitly resolve the formation and behavior of the electric double layer in a $KHCO_3$–CO_2 system confined within a slit nanopore bounded by substrate walls with alternating hydrophilic and hydrophobic regions. The Constant Potential Method (CPM), based on the Siepmann–Sprik polarizable electrode model, is used to apply different electrode potentials by allowing the electrode to dynamically respond to the surrounding electrolyte environment through fluctuating atomic charges. Spatially resolved one- and two-dimensional profiles reveal that charged surfaces induce strong ionic layering, while CO_2 is repelled from dense interfacial zones and instead accumulates along triple-phase boundaries (TPBs). This localization becomes more pronounced with increasing cathodic bias, indicating a field-assisted enrichment mechanism. Such behavior reflects experimental observations from gas-fed CO_2 electrolyzers, where conversion rates are highest near TPBs. Additionally, lateral heterogeneities driven by surface chemistry and confinement emerge clearly in the MD results: features that are absent in continuum approaches. These findings provide a foundation for future simulation and experimental studies aiming to engineer local CO_2 environments, and contribute to broader efforts in optimizing interface-driven transport in electrochemical and catalytic systems.

Contents

List of Figures

List of Tables

List of Abbreviations

CAH: Contact Angle Hysteresis

CCUS: Carbon Capture Utilization and Storage

CL: Catalyst Layer

CLSM: Confocal Laser Scanning Microscopy

CO_2RR: CO_2 Reduction Reaction

CVD: Chemical Vapor Deposition

DRI: Direct Reduced Iron

EDL: Electric Double Layer

FE: Faradic Efficiency

GDE: Gas Diffusion Electrode

GMPNP: Generalized Modified Poisson–Nernst–Planck

HER: Hydrogen Evolution Reaction

MEA: Membrane Electrode Assembly

MS: Magnetron Sputtered

npAu: Nanoporous Gold

NZE: Net Zero Emission

OER: Oxygen Evolution

PNP: Poisson–Nernst–Planck

PTFE: Polytetrafluoroethylene

TPB: Triple Phase Boundary

WEP: Water Entry Pressure

1 Introduction

1.1 Rising CO_2 Emissions and Policy Context

Carbon dioxide (CO_2) emissions are among the most pressing environmental challenges of our time. These emissions, mainly caused by human activities such as the combustion of fossil fuels, deforestation, industrial processes, and agricultural practices, are the primary driver of global warming and climate change. Since the onset of the Industrial Revolution, atmospheric CO_2 concentrations have risen to unprecedented levels, contributing to significant changes in weather patterns, rising global temperatures, melting ice caps, and rising sea levels. Figure 1 depicts that prior to the Industrial Revolution, CO_2 emissions were low. Growth in emissions was slow until around the 1950s, but by 1990, emissions had quadrupled to 20 billion tonnes. Emissions have continued to rise, now at around 30 billion tonnes. Although the rate of growth has slowed, a true plateau of emissions has yet to be achieved [42].

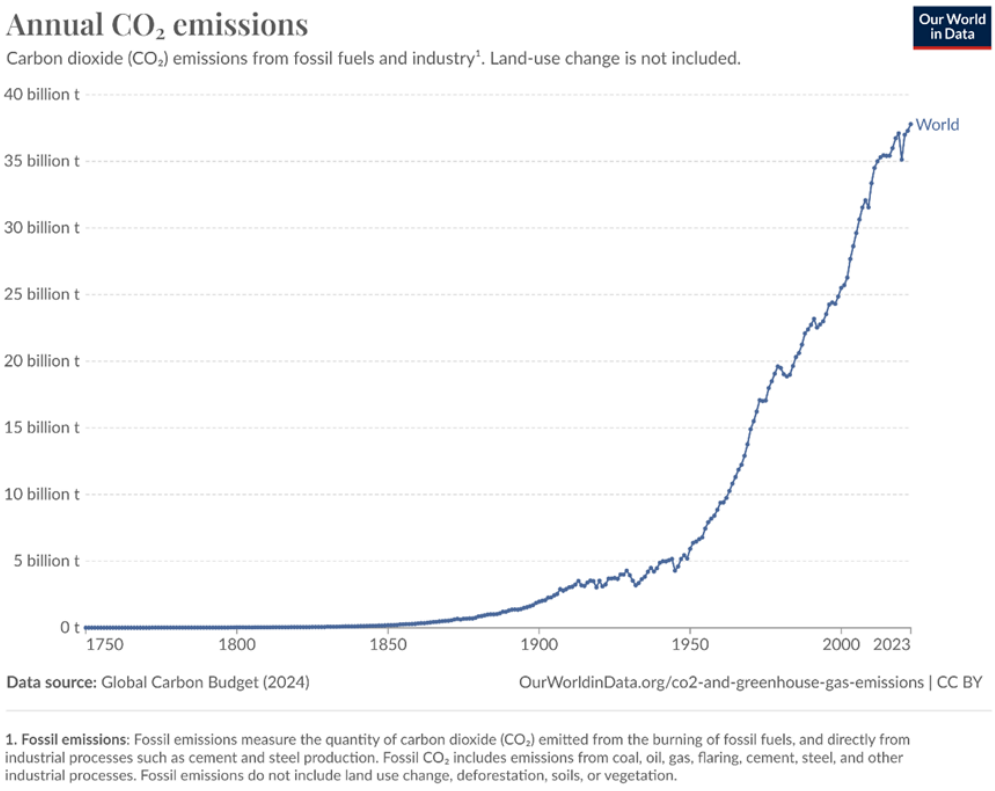

Figure 1: Annual (CO_2) emissions[42]

Furthermore, a constant rise in CO_2 emissions is observed country-wise, as can be seen in Figure 2. It is seen that CO_2 emissions until the 20th century were dominated by Europe and the United States (US). In 1900, the US and Europe dominated CO_2 emissions, and even in the 1950s, 85% of global emissions were from these regions. However, in recent decades, there has been a significant rise in CO_2 from the rest of the world, mainly across Asia, notably in China.

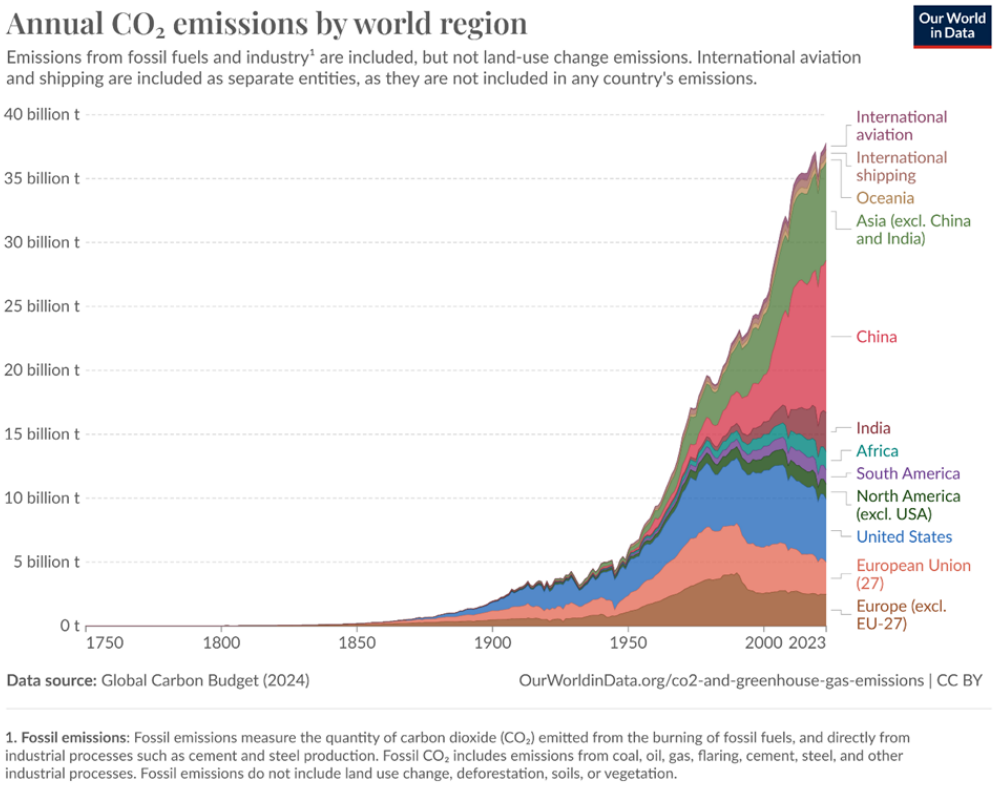

Figure 2: Annual (CO_2) emissions for world emissions[42]

Many countries are beginning, or have already started, implementing measures to tackle the increasing carbon emissions. As part of its efforts, Europe has introduced the European Green Deal, a comprehensive strategy aiming for climate neutrality by 2050. This includes over 3,000 policies [14], with an interim target to reduce emissions by 55% by 2030. Key actions focus on improving energy efficiency, expanding renewable energy, stimulating green job creation, and transitioning to cleaner transportation. Additionally, the plan emphasizes global cooperation to limit the global temperature rise to 1.5°C and effective waste management [13]. Similarly, China has set ambitious goals to peak its CO_2 emissions before 2030. The latest Five-Year Plan includes a target for an 18% reduction in CO_2 intensity and a 13.5% reduction in energy intensity from 2021 to 2025. There is also a proposal, though non-binding, to increase the share of non-fossil fuel energy to 20% of total consumption by 2025, up from around 16% in 2020 [23].

Furthermore, 76 countries, including India and the United States, are part of the COP28 agreement. The conference recognized the need to reduce global greenhouse gas emissions by 43% by 2030 in order to limit global warming to 1.5°C. However, it also acknowledged that many countries are off track in meeting the goals set by the Paris Agreement [50].

1.2 Need For CCUS

Among these urgencies, it is evident that promoting renewable energy plays a major role in countries' efforts to reduce CO_2 emissions. However, another key approach that many countries are adopting is Carbon Capture, Utilization, and Storage (CCUS). Techno-economic studies and policy analyses highlight that CCUS is a critical enabler of the

EU's transition to carbon neutrality, with a paper by Jones and Piebalgs highlighting its importance in reducing emissions and supporting the low-carbon transition[26]. While renewable energy and energy efficiency remain the foundation of the EU's further energy priorities, there are certain sectors such as energy-intensive industries where meeting net-zero emissions is extremely difficult. In these sectors, the alternatives are likely expensive (e.g., using electricity to generate heat) or simply do not exist (e.g., cement factories). Furthermore, certain industries like steelmaking provide limited alternatives to CCUS from both technical and economic considerations.

Technically, CCUS systems can be retrofitted to existing steel and chemical manufacturing infrastructure quickly[16]. Two case studies help illustrate its competitiveness compared to clean energy alternatives. In the steel industry, the hydrogen-based direct reduced iron (DRI) route is considered a low-emission alternative to conventional blast furnace processes. However, this pathway is not yet technologically mature and relies on the availability of large volumes of cheap, clean hydrogen. Economically, current estimates of levelised costs for commercial-scale plants show that producing one tonne of steel via a CCUS-equipped DRI plant raises costs by approximately 8–9% compared to today's mainstream production routes. In contrast, using hydrogen-based DRI raises costs by about 35–70%. A similar trend is observed in the chemical sector. Clean hydrogen can serve as a feedstock for ammonia and methanol production, offering an alternative to retrofitting existing plants with CCUS. However, in most regions, this clean hydrogen pathway is significantly more expensive—raising costs by 50–115%—compared to a more modest 20–40% cost increase when integrating CCUS. Other relevant industries where CCUS remains crucial include natural gas processing.
Based on these examples, it is evident that without a functioning CCUS network, it will be difficult to decarbonize these industries over the next 20 years and beyond.

The Role of Carbon Utilization in Net-Zero Strategies Carbon capture and storage refers to the process of separating CO_2 from relevant emission sources and then transporting it to storage sites, as well as separating CO_2 from the atmosphere for extended periods. This can reduce CO_2 emissions at the source and remove existing CO_2 from the atmosphere on a large scale[16]. Furthermore, a high increase in CO_2 concentration (ppm) has shown a corresponding rise in temperature, as indicated in the figure below, thereby highlighting the urgency to address CO_2 emissions.

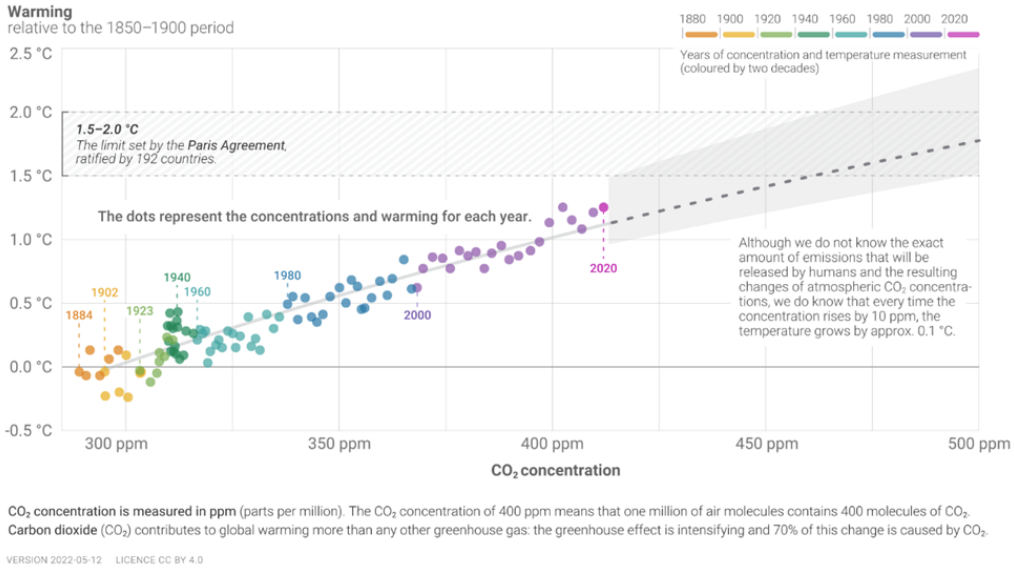

Figure 3: (CO_2) Concentration and Temperature change over the years[16]

In order to achieve a net-zero cycle, captured CO_2 must also be utilized. In this approach, CO_2 captured in production processes is transferred to various production plants for conversion or utilization. This process is not simply storage but reflects the recycling and reuse of CO_2[16].

According to the IEA, current project pipelines suggest that by 2030, around 15 Mt of CO_2 per year could be captured for new applications, with more than half—approximately 8 Mt—allocated to synthetic fuel production [24]. This represents a significant step toward scaling carbon utilization technologies. However, only a small share of this(just over 4 Mt) is expected to come from air or biogenic sources, as required under the Net Zero Emissions by 2050 (NZE) Scenario [24]. The remainder still relies heavily on fossil-derived CO_2, which limits its long-term climate benefits. While geological storage remains part of the carbon management strategy, it is not a permanent or economically productive solution. In contrast, carbon utilization—by converting captured CO_2 into synthetic fuels, chemicals, and building materials—offers a way to close the carbon loop while creating market value, making the process more economically viable [24].

Current approaches to converting and utilizing CO_2 mainly fall into two categories: physical and chemical utilization. The former includes storing CO_2 in underground facilities for enhanced oil recovery. The latter is further divided into biochemical, electrochemical, photochemical, and radiochemical methods. Among these, electrochemical reduction of CO_2 (CO_2RR) refers to converting CO_2 into value-added chemical species using electrical energy. Firstly, CO_2RR can be efficiently coupled with renewable electricity and can serve as an energy storage method. Secondly, products from CO_2RR can be used as alternatives to fossil fuel-based products. Furthermore, CO_2RR operates near room temperature (<100°C) under ambient conditions, and its products can be adjusted by changing parameters such as the catalyst or external voltage, making it an excellent choice for CO_2 utilization [31].

1.3 Electrochemical CO_2 Reduction (CO_2RR)

CO_2 electrochemical reduction (CO_2RR) refers to the conversion of carbon dioxide into value-added chemicals through redox reactions powered by electricity. It is a promising

method for CO_2 utilization because it can operate under ambient conditions and be coupled with renewable energy sources.

Electrolysis is the process of driving non-spontaneous redox reactions using electrical energy. In a CO_2 electrolyzer, the electrochemical cell consists of two electrodes (a cathode and an anode) separated by a membrane. The cathode is where CO_2RR takes place—CO_2 molecules can be reduced by gaining electrons and protons to form carbon products, among other possible reaction pathways. The anode is where the Oxygen Evolution Reaction (OER) occurs, producing oxygen gas and releasing H^+ ions, which migrate through the membrane toward the cathode side to participate in CO_2 reduction.

Various designs of electrolyzers are used for CO_2RR, including H-cells, gas diffusion electrodes (GDEs), and solid-state electrolysis cells. H-cells are typically used in lab-scale setups for fundamental catalyst screening and probing. In contrast, GDEs and solid-state cells increase the active surface area and are more suitable for scaling up toward commercial applications. The cathodes are typically made from metals such as copper, silver, or gold, chosen based on their product selectivity. Copper, for example, favors hydrocarbons like methane and ethylene.

The specific product formed during CO_2RR depends on the number of electrons and protons transferred, the catalyst material, and the applied voltage. The table below lists common half-cell reactions for CO_2RR, along with their standard electrode potentials [7]:

Table 1: Electrochemical half-cell reactions and their standard potentials [7]

Half-cell reaction	**E° (V/SHE)**
$2H^+ + 2e^- \rightarrow H_2$	-0.42
$CO_2 + 2H^+ + 2e^- \rightarrow CO + H_2O$	-0.52
$CO_2 + 2H^+ + 2e^- \rightarrow HCOOH$	-0.61
$CO_2 + 6H^+ + 6e^- \rightarrow CH_3OH + H_2O$	-0.38
$CO_2 + 8H^+ + 8e^- \rightarrow CH_4 + 2H_2O$	-0.24
$CO_2 + 12H^+ + 12e^- \rightarrow C_2H_4 + 4H_2O$	-0.34

Similarly, at the anode, water oxidation takes place via the Oxygen Evolution Reaction (OER). Electrode materials such as iridium oxide or ruthenium oxide are used for this purpose. The OER generates protons (H^+) and oxygen gas, with the protons migrating through the membrane to the cathode side, enabling the CO_2 reduction reaction [7]. The half-cell reaction at the anode is:

$$2H_2O \rightarrow O_2 + 4H^+ + 2e^-$$

A schematic overview of the electrolyzer setup is shown in Figure 4.

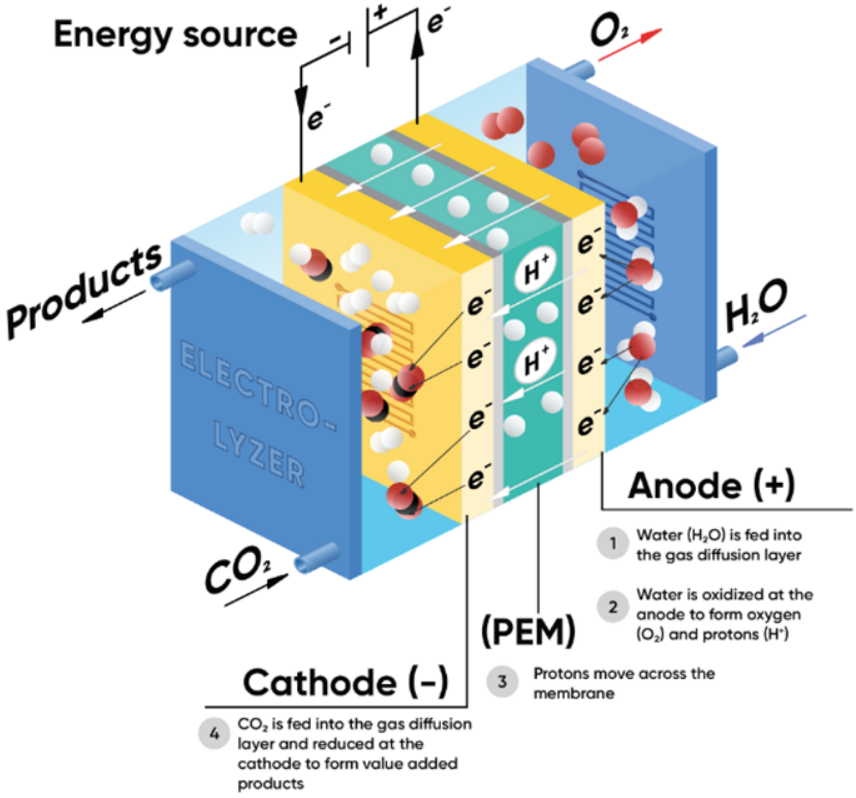

Figure 4: GDE based CO_2 Electrolyser [7]

1.4 Factors Influencing CO_2RR Performance

CO_2RR performance and product output are influenced by various factors such as cathode electrode composition, catalyst, etc. The cathode catalyst layer plays an important role in the CO_2RR process as it greatly affects the mass diffusion rate and accessibility of active sites [62]. Research by Zeng et al. shows that the weight percentage of Nafion binder, carbon black, and catalyst on the cathode side significantly impacts CO selectivity and production rate. Each component has multiple roles: Nafion increases electron and mass transport resistance but lowers charge transfer resistance at high overpotentials. Catalyst loading affects active site availability and mass diffusion, optimizing catalyst utilization. Carbon black enhances electrical conductivity, reduces catalyst agglomeration, and selectively promotes H_2 formation[62]. Similarly, Hika et al. shows that the anode catalyst impacts cathode activity and selectivity, influencing the CO_2 electrochemical reaction[21]. They demonstrate that the Au/Fe_2O_3 system achieves higher CO selectivity than Au/Pt at both applied potentials, with greater CO formation at -0.4 V and comparable production at -0.6 V. In contrast, Au/Pt favors H_2 evolution. The study suggests that Fe_2O_3, being stable, inexpensive, and widely available, can effectively replace the Pt counter electrode.

Similarly, several other factors influence CO_2RR performance and product distribution. Extrinsic factors include the reduction temperature, electrolyte type and concentration, reaction cell design, catalyst/mass loading, electrolyte pH, pressure, and applied potential[8]. The choice of electrolyte, for instance, can significantly affect the reaction kinetics and selectivity by altering the local environment at the electrode surface. Oper-

ating conditions such as temperature and pressure also play crucial roles in determining the efficiency and product distribution of CO_2RR[33]. Furthermore, reactor design and flow cell configurations, such as zero-gap cells or membrane electrode assembly (MEA) setups, impact mass transport and overall system efficiency, further shaping the CO_2 reduction process.[33].

Gas Diffusion Electrodes (GDEs) and Flooding Challenges in CO_2RR Currently, gas diffusion electrodes (GDEs) are emerging as an effective approach to improving current densities and addressing issues related to selectivity, stability, and overpotentials. This improvement is primarily achieved by overcoming the limitations of CO_2 diffusivity on the cathode side. By positioning the catalyst near a gas-liquid interface, mass transport is enhanced, leading to improved performance[29].

Weng et al. compared GDEs with planar electrodes[56]. Figure 5 shows that for cathode potentials below −1.1 V vs. RHE, the CO partial current is nearly an order of magnitude higher for GDEs compared to planar electrodes. The authors attribute this improvement primarily to the higher concentration of catalytically active sites per unit geometric cathode area in GDEs, which is a consequence of their porous structure.

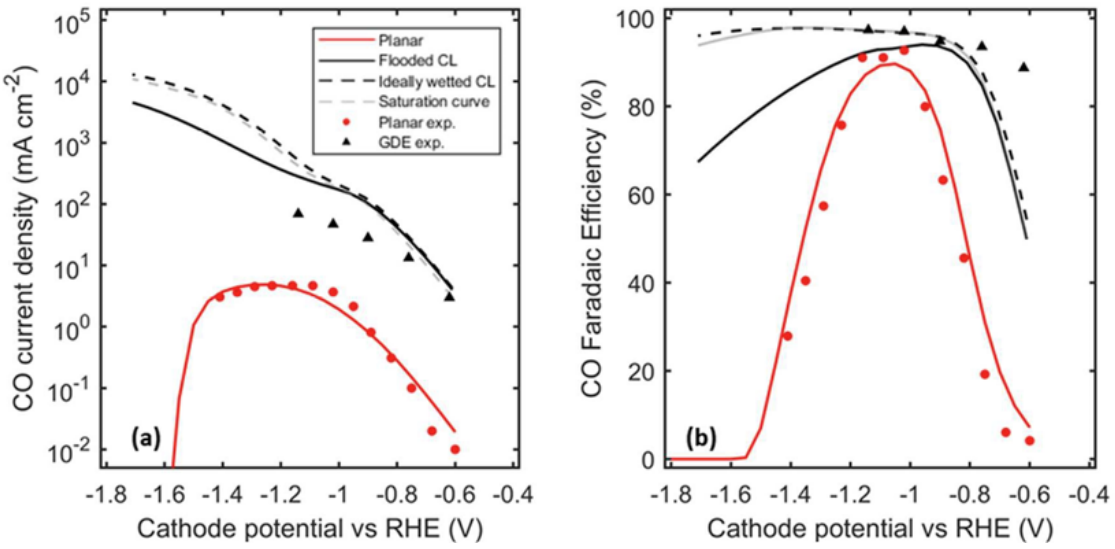

Figure 5: CO partial current density (a) and CO Faradaic efficiency (b) as functions of cathode potential versus RHE, compared across planar, flooded, ideal-wetting, and saturation-curve conditions.[56]

For potentials lower than −1.1 V vs. RHE, the performance difference becomes even more pronounced because the mass transfer resistance in GDEs is significantly lower than in planar systems. In GDEs, the short diffusion distance in the electrolyte enhances CO_2 mass transfer to the catalyst, thereby increasing efficiency in terms of current density and Faradaic efficiency.

The study also highlights that the performance of GDEs greatly depends on the local conditions within the catalyst layer (CL). Factors such as capillary pressure, pore size distribution, and the catalyst material can lead to complete flooding of the pores, which eliminates gas channels and increases mass transfer resistance for gaseous reactants. As seen in Figure 5, although flooded GDEs exhibit high current densities compared to planar electrodes, their selectivity toward CO decreases around −1 V vs. RHE. In

contrast, a partially wetted CL performs significantly better, achieving higher CO partial current densities and improved CO Faradaic efficiency, especially at high potentials, as demonstrated in Figure 5 and Figure 6. Partially wetted pores facilitate the penetration of gas-phase CO_2 through the CL, allowing for a more uniform distribution of dissolved CO_2.

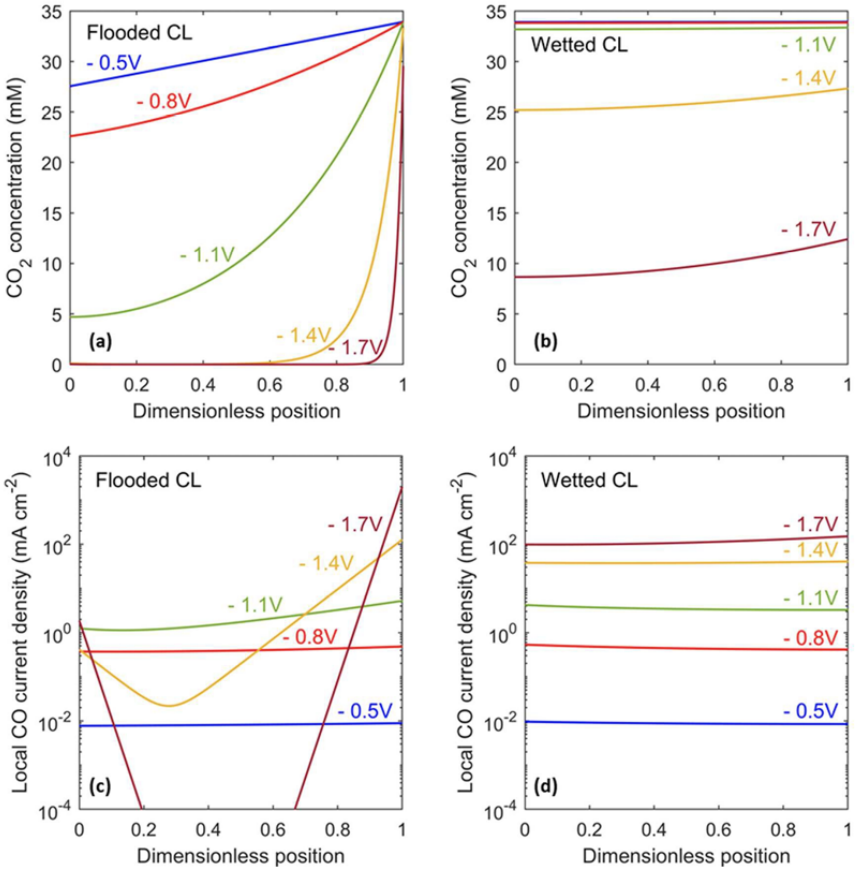

Figure 6: CO_2 concentration distribution (a & c) and corresponding local CO current density (b & d) within the catalyst layer for the flooded configuration (a & b) and the ideal-wetting configuration (c & d). The horizontal axis represents the dimensionless position normalized by the catalyst layer thickness, with 0 denoting the electrolyte/CL interface and 1 denoting the CL/GDL interface[56]

The research indicates that although flooded GDEs demonstrate improved current densities and Faradaic efficiencies compared to planar electrodes, issues such as uneven CO_2 concentration and non-uniform CO_2 current density distribution(Figure 6a,b) can adversely affect long-term stability. Burdyny et al. stated that flooding of the GDL will typically occur within several hours of operation, resulting in diminished selectivity toward products of the CO_2 reduction reaction[59]. Several researchers have further emphasized the need for precise wetting control. Research by Mengran et al. demonstrates that flooding—or more specifically, the invasion of electrolyte into the pores—increases the diffusion distance for CO_2. This extended path allows OH^- ions generated by the CO_2RR and the hydrogen evolution reaction (HER) to react with CO_2, reducing its availability at the catalyst surface and gradually shifting the cathode reaction from CO_2RR to HER[29].

Furthermore, the rapid formation of carbonates and bicarbonates quickly reaches their

solubility limits as water evaporates from the gas phase, leading to salt precipitation[30]. At industrial-level current densities (>200 mA/cm^2), flooding becomes a critical issue that reduces operational time by diminishing both selectivity and reaction rate. Precipitated salts physically block the gas diffusion pathways, consume CO_2 by converting carbonates to bicarbonates, and accelerate electrolyte precipitation. Tailoring the wettability of electrodes to mitigate these challenges while ensuring long operating hours could lead to significant improvements in both stability and current density.

In brief, substantial opportunities remain to engineer these partially wetted, field-induced (gas–liquid–solid boundaries) triple-phase boundaries (TPB) to control wetting and optimize performance.

2 Literature Review

2.1 Preface

This literature review covers recent advances in nanoporous materials and wetting control in CO_2 electrolyzers, discussing material-based and environmental strategies—including coatings, surface modifications, pH, and electrolyte composition—as well as the fundamentals and applications of electrowetting. It also highlights the role of molecular dynamics simulations in modeling these systems, setting the stage for research aimed at enhancing electrolyzer stability and efficiency through detailed analysis of the triple-phase interface.

2.2 Fundamentals of Wetting

Wetting is a fundamental interfacial interaction that governs the behavior of fluids on solid surfaces. It is primarily determined by intermolecular forces, including van der Waals and electrostatic (Coulombic) forces[3]. A strong intermolecular interaction enhances solid–liquid adhesion and generally reduces the macroscopic contact angle. Van der Waals forces, which arise at the solid–liquid interface, can be categorized into London dispersion, Debye, and Keesom forces, based on dipole interactions. Among these, London dispersion forces are typically weaker than Debye (dipole-induced) and Keesom (dipole-dipole) forces becuase it originates from random charge re-distribution in molecules with no permanent dipoles. All these forces are highly dependent on the chemical properties of the solid and liquid such as polarity, dipole moments, structures, and charging states[29].

The classical approach to quantifying wettability involves measuring the contact angle (θ) between a liquid droplet and a solid surface. Young's equation relates the contact angle to the interfacial tensions between the solid–vapor (γ_{SV}), solid–liquid (γ_{SL}), and liquid–vapor (γ_{LV}) interfaces:

$$\gamma_{SV} = \gamma_{SL} + \gamma_{LV} \cos\theta$$

where a contact angle less than 90° indicates a hydrophilic surface, while an angle greater than 90° signifies a hydrophobic surface. However, real surfaces, such as catalyst layers in the CO_2RR, are rarely ideal and exhibit variations due to roughness and chemical heterogeneity. Surface defects and microstructures can pin the contact line, leading to significant deviations in the apparent contact angle[29]. On rough surfaces, wetting behavior is often described by the Wenzel and Cassie–Baxter models (Figure 7). In the Wenzel state, the liquid fully infiltrates the surface roughness, enhancing wettability if the surface is hydrophilic but increasing hydrophobicity if the surface is inherently hydrophobic. The Wenzel equation is given by:

$$\cos\theta^* = R \times \cos\theta, \quad R = \frac{area_{real}}{area_{geo}}$$

Where θ^* is the apparent contact angle and R is the roughness factor. In contrast, the Cassie–Baxter state occurs when air pockets are trapped beneath the droplet, reducing the solid–liquid contact area and maintaining a higher apparent contact angle. This state is described by:

$$\cos\theta^* = f(\cos\theta + 1) - 1, \quad f = \frac{area_{solid}}{area_{solid} + area_{air}}$$

where f represents the fraction of solid surface in contact with the liquid. The Cassie–Baxter state is favored when the surface is chemically hydrophobic and highly textured. Although for moderate hydrophobicity and roughness, one could still observe a metastable Cassie–Baxter state. This could transition to the Wenzel state under external perturbations, such as pressure or an applied electric field(Figure 7c) that can overcome the energy barrier required to wet the inner walls within the surface texture[29].

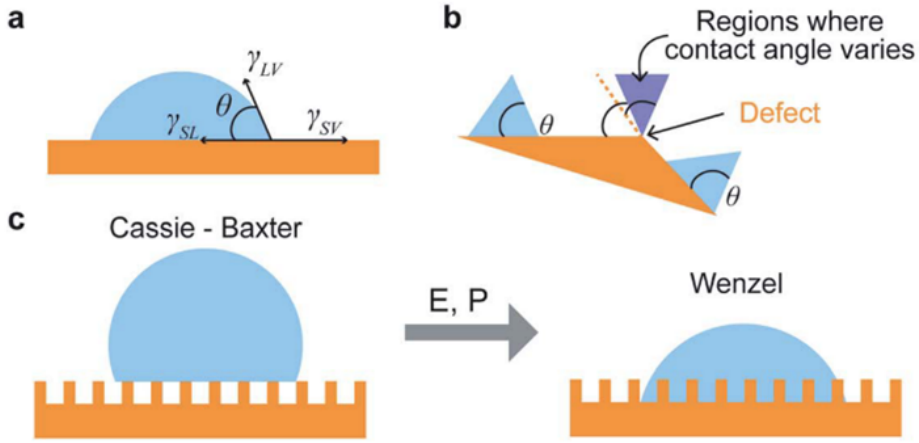

Figure 7: A schematic depiction showing: (a) the static contact angle on an ideal, perfectly flat surface, and (b) the variation in contact angle on a surface containing defects. Such defects may be chemical in nature—such as corners, kinks, dopants, or vacancies—or structural, for instance surface roughness. (c) Illustration of the Cassie–Baxter and Wenzel wetting states, where an applied electric field (E) or pressure (P) can trigger a transition from the Cassie–Baxter to the Wenzel regime[29]

In the context of CO_2RR, the GDE consists of materials with varying wettabilities, such as that of liquid electrolytes, liquid products, and condensed water. Considering GDE as a porous medium with a network of connected porous cylinders, the capillary pressure (P_C) can be described using the Young–Laplace equation:

$$P_C = \frac{\gamma_{LV}\cos\theta}{r} = \frac{\gamma_{SV} - \gamma_{SL}}{r}$$

Where P_C is the capillary pressure and r is the pore radius. High capillary pressure facilitates liquid infiltration into the porous network, although the presence of an electric field during CO_2RR further complicates wetting behavior. Additionally, the inherent porosity and chemical heterogeneity of GDEs introduce further complexities in predicting wetting dynamics[29].

Having established the fundamentals of wetting, the following sections will explore the primary factors driving electrolyte penetration into catalyst layer structures (CL) and gas diffusion layers (GDL). These include the effects of wettability, pore structure, capillary forces, and electrostatic influences, all of which play a crucial role in determining electrolyte distribution and transport in CO_2RR systems.

2.3 Electrolyte Penetration and Flooding in GDEs

The penetration of electrolyte in gas diffusion layers occurs primarily due to three factors: Electrowetting, Pressure difference, and Salt precipitation.

Electrowetting refers to the enhanced spreading of a liquid on a surface under an applied electric field. This phenomenon is described by the Young–Lippmann equation, which establishes the relationship between the applied potential and the contact angle (Equation 1)[57]. Under CO_2 electrolysis conditions, the contact angle decreases as the applied potential increases. This effect occurs for both conductive and dielectric materials, though it is more pronounced in conductive materials due to their higher sensitivity to electric field-induced wetting changes[29].

$$\cos\theta_E = \cos\theta_0 + \frac{1}{2}\frac{\varepsilon\varepsilon_0}{\gamma_{LV}d}(E - E_{PZC})^2 \tag{1}$$

In the above equation, θ_E is the contact angle under the applied electric field E; E_{PZC} is the potential of zero charge; θ_0 is the contact angle in the absence of an electric double layer (EDL); ε_0 is the permittivity of free space; ε is the dielectric constant of the liquid on an electrically conductive substrate; γ_{LV} is the surface tension between the liquid and gas; and d is the thickness of the double layer.

Likewise, the differential pressure between the gas and liquid phases within the gas diffusion layer (GDL) must be carefully regulated near the active interfaces. Even minor overpressure on either the gas or liquid side can lead to bubble formation in the liquid phase or cause flooding in the GDL. Maintaining a stable differential pressure is essential; however, imbalances are commonly observed in current studies. The positioning of the three-phase boundary within the GDE pores and the extent of electrolyte flooding are influenced by differential pressure[57]. Similarly, Bert et al. examined how pressure drop across the GDE impacts flooding, which they assessed by analyzing the electrolyte penetration rate. Their study concluded that no single differential pressure between the catholyte and gas chamber optimizes CO_2 electrolysis performance[11].

Salt precipitation, also referred to as carbonation, is another major factor contributing to GDE deactivation in both microfluidic and membrane electrode assembly (MEA) flow cells. The accumulation of bicarbonate and carbonate salts, along with water consumption during CO_2 electrolysis, can push the salt concentration beyond its solubility limit, leading to the precipitation of solid potassium carbonate. These deposits progressively clog the GDE's pores, restricting CO_2 transport to the catalyst and eventually halting electrolysis. This degradation pathway is illustrated in Fig. 8. Ultimately, electrolyte flooding facilitates salt precipitation within the GDE, and their interconnected effects are only beginning to be fully understood.

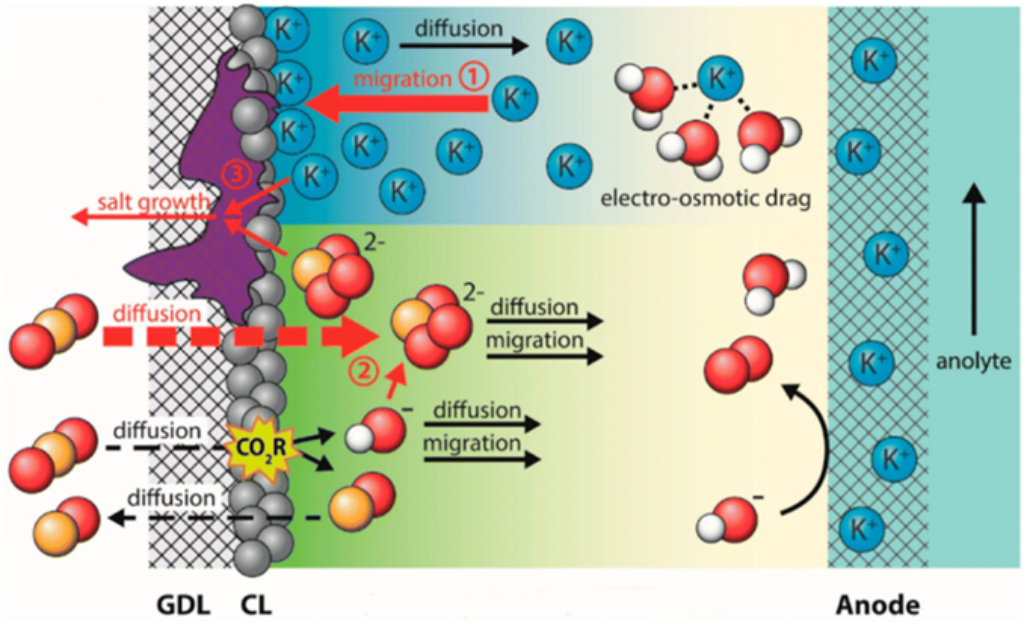

Figure 8: Schematic of the salt precipitation degrading the GDE together with electrolyte flooding[57]

2.4 Optimum Wettability for Improved CO_2RR Performance

Notably, while uncontrolled electrolyte penetration can lead to flooding and salt deposition, controlled penetration boosts performance as seen in Figure 5 and 6. Gas diffusion electrodes are typically designed to be gas-wet to ensure optimal performance. This design facilitates the rapid diffusion of CO_2 to the catalyst layer and the efficient removal of gaseous products into the bulk gas phase. At the same time, the CL should be partially wetted by the electrolyte to enable effective proton transport and the dissolution of reactants at the reaction sites while also acting as a sink for byproducts such as hydroxide ions, formate, and alcohols. However, the ideal wetting state for CO_2RR remains unclear[29].

One widely proposed optimal wetting state involves the presence of multiple solid-liquid-gas triple-phase boundaries (TPBs) at the catalyst layer. This stems from the fact that 1) CO_2RR requires both CO_2 and protons as reactants while relying on the electrolyte to act as a sink for byproducts. 2) The commonly observed improvement in efficiency and selectivity with a moderate increase in hydrophobicity. For example, Shi et al. investigated the relationship between wetting states and CO_2 reduction reaction (CO_2RR) performance, suggesting that a moderate hydrophobicity—where both Wenzel and Cassie–Baxter states coexist—is optimal for CO production. Their conclusions were drawn from ex situ confocal laser scanning microscopy (CLSM) and CO_2RR performance tests on Au/carbon black-based catalyst layers with varying wettability. The wettability was modified using fluorinated silane treatment (Au/C–F) to enhance hydrophobicity or air plasma treatment (Au/C–P-0.5 and Au/C–P-2.5) to progressively increase hydrophilicity. CLSM analysis confirmed the hydrophobicity trend as Au/C–F (Cassie–Baxter state) > Au/C–P-0.5 (mixed state) > Au/C–P-2.5 (Wenzel state). Notably, the Au/C–P-0.5 catalyst exhibited the highest CO_2RR performance, highlighting the advantage of a balanced wetting state[44][29].

Nevertheless, the importance of triple-phase boundaries and their role in the CO_2

reduction reaction (CO_2RR) has yet to be explicitly defined. If the triple-phase boundary is considered the primary reaction zone—as shown in Figure 9—the CO_2RR proceeds as follows: first, CO_2 diffuses through the electrolyte, and then both ions and CO_2 are transported to the reaction site. This pathway is favored because it is energetically more efficient than the alternative mechanisms, which include (1) the weak adsorption of CO_2 on a dry metal surface—requiring pressures as high as 33 atm for CO_2 to adsorb on Cu(111) at 25°C[15][29]—and (2) the significantly slower diffusivity of CO_2 along a dry surface compared to its movement through the liquid phase. Although CO_2 diffusion is much faster in the CO_2 film (grey area in Figure 9), the contact area with the catalyst is too limited to serve as the primary reaction zone.

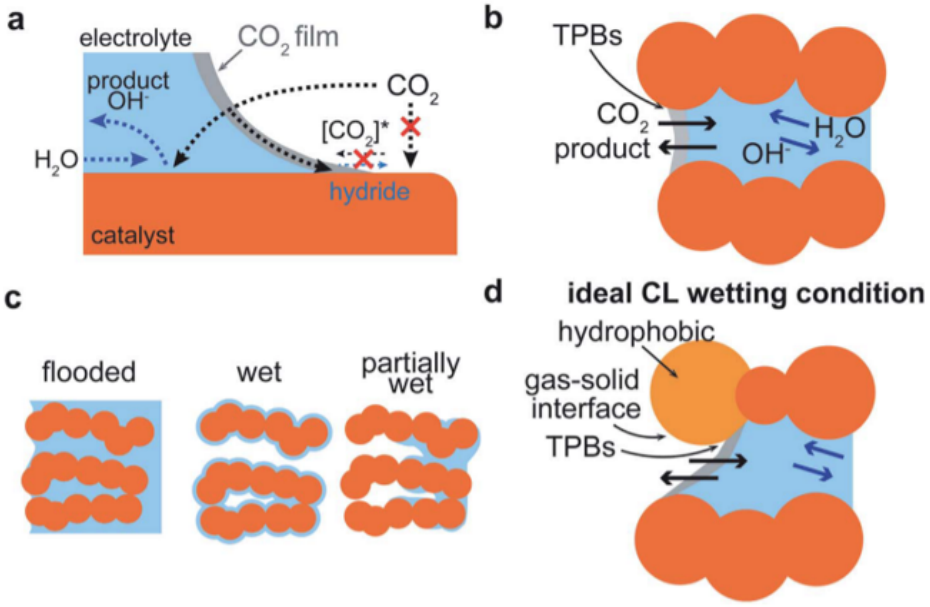

Figure 9: Schematic representation of (a) possible pathways for CO_2 transport toward the catalyst surface at triple-phase boundaries (TPBs), (b) various wetting states within the pores of a homogeneous catalyst layer (CL), (c) potential wetting scenarios within the CL structure, and (d) the targeted wetting state for pores within the CL[29]

Further critical discussion of phase boundaries were conducted by Nesbitt et al., who reviewed the dominant phase boundaries within uniform porous catalyst layers for CO_2 reduction reaction and drew several key conclusions: (1) the CL pores should be filled under CO_2RR conditions(Figure 9b), (2) solid-liquid boundaries serve as dominant reaction zones within the CL, and (3) the reaction zone is expected to be approximately 100 to 1000 nm in size within the catalyst layer [34].

Additionally, Weng et al. highlighted that the CO_2 concentration in a liquid electrolyte (33 mM at 20°C and 1 atm) is not significantly lower than in the gas phase (42 mM) [56]. This suggests that the orders-of-magnitude improvement in GDE performance compared to planar electrodes is primarily due to (1) a significant reduction in CO_2 diffusion distances in the liquid electrolyte from 40–160 μm to 0.01–20 μm[29] and (2) an increased density of active reaction sites. However, the wet condition suggested by Weng et al.[56] (Figure 9C) is unlikely, given the relatively thick hydrodynamic layers of electrolyte inside the nanopores. This is especially true in the absence of hydrophobic additives like PTFE, where pores are more likely to be only partially filled (Figure 9B),

confining the triple-phase boundaries mainly to the GDL-CL interfaces. In this context, if TPBs were the primary reaction sites, the thickness of the CL should have minimal impact on CO_2RR activity. However, findings by Xing et al., which demonstrate a clear effect of CL thickness on CO_2RR performance, suggest that TPBs are not the dominant reaction zones in CO_2RR [58].

Considering the solid-liquid interface as the primary reaction zone, as discussed by Nesbitt et al.[34], Mengran et al. proposed an explanation for the observed enhancement in CO_2RR activity under moderate hydrophobicity, which effectively creates wet and partially wet conditions. The increased activity is primarily attributed to (1) a reduced diffusional distance for CO_2 in the liquid phase, allowing it to reach the solid-liquid reaction sites near the bulk electrolyte more efficiently, and (2) an extended gas-solid interface due to the presence of hydrophobic additives (Figure 9D). These gas-solid interfaces, along with TPBs, provide shorter diffusion pathways for CO_2 gas, while liquid-wetted pathways ensure access to the electrolyte and facilitate the migration of CO_2RR liquid products to the bulk electrolyte[29].

The extended gas-solid interfaces are achieved by introducing hydrophobic additives such as PTFE and alkanethiols[29] between catalyst sites. These non-reactive additives have minimal impact on the density of active sites, provided that the catalyst remains conductive and accessible to the bulk electrolyte. Additionally, this CL configuration may reduce the transport length for dissolved CO_2 by preventing its migration through long pores. This explanation aligns with the hypothesis that the coexistence of Cassie–Baxter and Wenzel wetting states, as suggested by Shi et al.[44], plays a crucial role in optimizing electrode wetting for improved CO_2RR performance.

However, it is important to acknowledge the need for sufficient electrochemically active sites within the CL structure. Electron-conducting phases, such as carbon materials, provide these active sites while also forming the essential solid-liquid interface that facilitates reaction and transport pathways for electrolytes and liquid products. At the same time, hydrophobic additives help create extended gas-solid interfaces that enhance CO_2 transport. However, these additives also increase the overall ohmic losses of the electrode and can lead to a reduction in active sites due to their non-conductive and non-reactive nature[29]. Therefore, a trade-off exists between ensuring sufficient active sites and establishing efficient gas and liquid transport pathways.

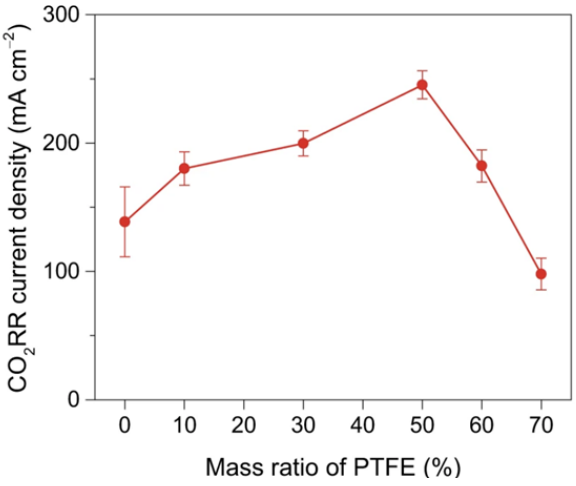

Figure 10: Partial current density for CO_2 at -1.0 V on Cu/C/PTFE electrodes with different mass ratios of PTFE in the catalyst layer[58]

A study conducted by Xing et al. demonstrated the effect of PTFE nanoparticles amount on the CO_2RR current density. Their results showed that a 50% PTFE mass loading reduced the diffusion layer thickness from 20.2 µm to 3.2 µm, increasing the CO_2 reduction current density to approximately 250 mA/cm^2 at −1.0 V vs. RHE (Figure 10). These findings confirm that a moderate level of hydrophobicity is typically optimal for CO_2RR[58].

In conclusion, achieving optimal CO_2RR performance demands a catalyst layer that simultaneously promotes rapid liquid and electron transport, maximizes the density of active and selective sites, and optimizes the local reaction environment. This requires a strategic combination of materials with complementary wettability and functional properties, enabling multiple transport pathways for CO_2, protons, electrons, and reaction byproducts, thereby minimizing diffusion distances. Additionally, the integration of a hydrophobic gas diffusion layer is critical to sustaining fast gas-phase transport.

2.5 CO_2RR performance optimization by wettability manipulation

The previous section outlined the ideal wetting conditions, emphasizing the factors that influence wettability and the requirements for maximizing electrolytic performance, efficiency, and selectivity. The following section examines in greater detail the various parameters that affect wettability and, consequently, performance, as well as strategies for tailoring these conditions to meet specific application needs.

2.5.1 Role of liquid in electrode wettability

The wettability of a liquid on a solid surface is determined by the balance between cohesive and adhesive forces. Cohesive forces refer to the intermolecular attractions that hold liquid molecules together, while adhesive forces describe the interactions between the liquid and the solid surface. When adhesive forces dominate over cohesive forces, the liquid tends to spread more readily. Both cohesive and adhesive forces are influenced by the liquid's intrinsic properties, such as polarity, ionic nature, ionic strength, and overall composition.

Study by Leonard et al. compared the contact angles of CO_2RR liquid products with their aqueous solutions on PTFE and graphite surfaces. Their findings indicate that CO_2RR liquid products exhibit greater spreading compared to water, with longer-chain carbon-based products displaying even higher wettability[28].

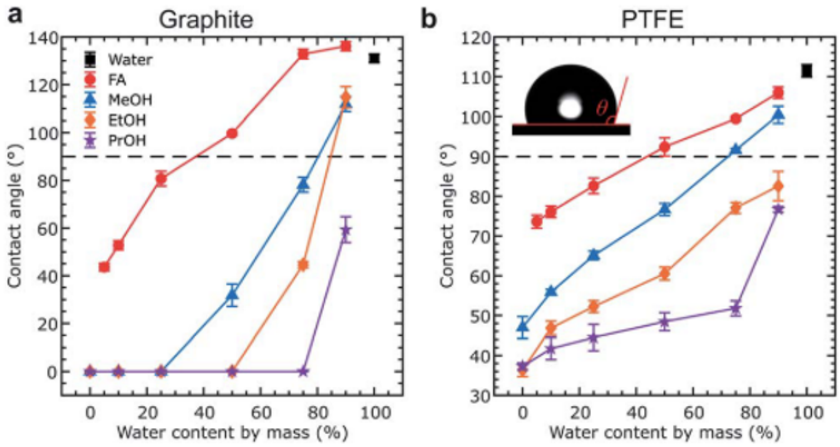

Figure 11: Comparison of static contact angles for water and aqueous solutions containing liquid CO_2RR products on (a) graphite and (b) PTFE substrates[28]

This behavior, illustrated in Figure 11, is primarily attributed to the nonpolar nature of C–H bonds. As the proportion of these bonds increases in aqueous solutions, the overall polarity and cohesive forces of the liquid decrease, thereby enhancing spreading.

The effect of ions on wetting primarily depends on their hydration energy and their interactions with the solid substrate. Figure 12 illustrates the relationship between hydration enthalpy and the gradient of surface tension. Highly charged, small ions attract more water molecules, resulting in strong hydration shells. These robust interactions among water molecules increase the cohesion within the electrolyte, thereby reducing the liquid's ability to spread on the solid surface. In contrast, ions such as K^+ and Cs^+ have much weaker hydration shells. This enables them to approach the solid substrate more closely within the electrical double layer, intensifying the local electric field and promoting both CO_2 reduction reaction activity and enhanced spreading[29].

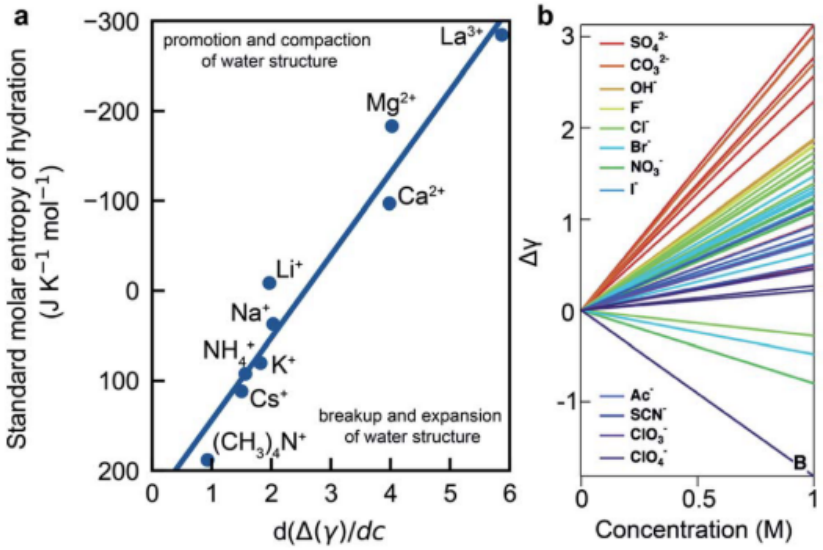

Figure 12: (a) Correlation between the salt concentration–induced tension gradient and the hydration entropies of cations. (b) Influence of anion concentration on variations in electrolyte surface tension[29]

Similarly, solutions with a high concentration of hydrated anions exhibit increased cohesive forces within the electrolyte, leading to higher surface tension. In contrast, anions such as I^-, which have relatively low hydration, tend to form bonds with the electrode at the inner Helmholtz layer (the compact layer of specifically adsorbed ions directly at the electrode surface). This bonding enhances the adhesive forces at the interface and promotes liquid spreading. Additionally, anions can interact with hydrophobic surfaces to facilitate wetting.

In the absence of an external potential, OH^- ions are prone to adsorb onto hydrophobic surfaces due to interactions between their intrinsic dipole moment and the oriented dipoles of adjacent water molecules close to the surface. This phenomenon explains the reduced contact angle on PTFE for liquids with high pH[40][29]. Similarly, Virga et al. investigated the pH-dependent wettability of amphoteric surfaces (Al_2O_3 and TiO_2) using a theoretical 1-pK model and captive bubble experiments. They found that contact angles peaked at the materials' point of zero charge (PZC; 8.7 for alumina, 4.4 for titania), where surfaces were neutrally charged and most hydrophobic. pH affects wetting by modulating the surface charge and thereby deviating from this point, increases surface ionization, enhancing hydrophilicity and reducing contact angles[52].

2.5.2 Role of Solid in electrode wettability

The way electrodes are manufactured and their morphology also affect wettability and, in turn, the performance of the CO_2 electrolyzer. The study by Preston et al. shows that the coating application process markedly affects the hydrophobicity of graphene. They demonstrated that ultrathin graphene coatings (1–2 atomic layers) reduce the surface energy of copper, making it hydrophobic. This is quantified by advancing contact angles of 87°–93°, where water droplets bead up rather than spread out[38].

Furthermore, graphene coatings grown via CVD exhibit microscopic grain boundaries and defects, as seen in Figure 13. These imperfections create localized variations in surface energy, leading to contact angle hysteresis. High hysteresis (30°) means droplets adhere more strongly to the surface, thereby promoting wetting[38].

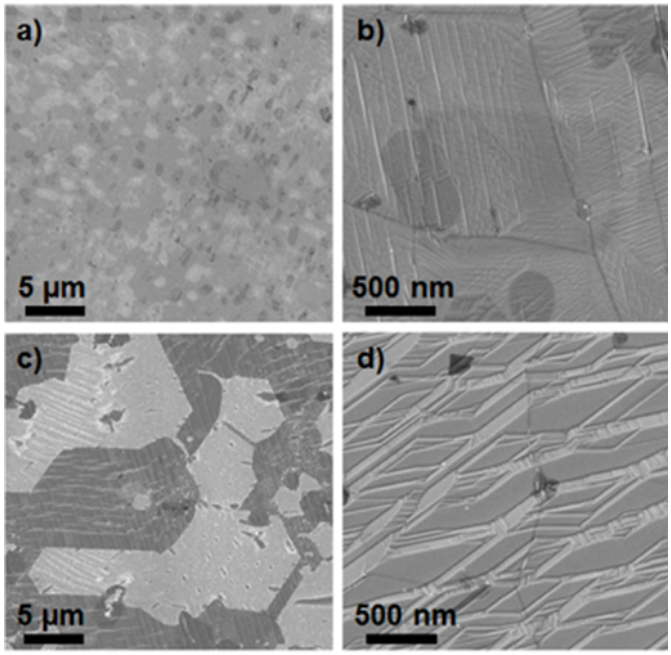

Figure 13: FESEM micrographs showing (a,b) graphene layers produced via low-pressure CVD and (c,d) those grown under atmospheric-pressure CVD, both deposited on copper substrates of purity exceeding 99.99%[38]

Recent work by Zhen et al. demonstrates that engineering catalyst morphology via nanoporous gold (npAu) coatings can markedly enhance both wetting behavior and CO_2 reduction performance. In their study, conventional magnetron-sputtered (MS) Au coatings showed a low contact angle (20°), leading to significant electrolyte flooding. In contrast, npAu coatings—achieved through dealloying—exhibited much higher contact angles (140° for a 400 nm film and 90° for an 800 nm film), which stabilize the triple-phase boundaries, as seen in Figure 14[39].

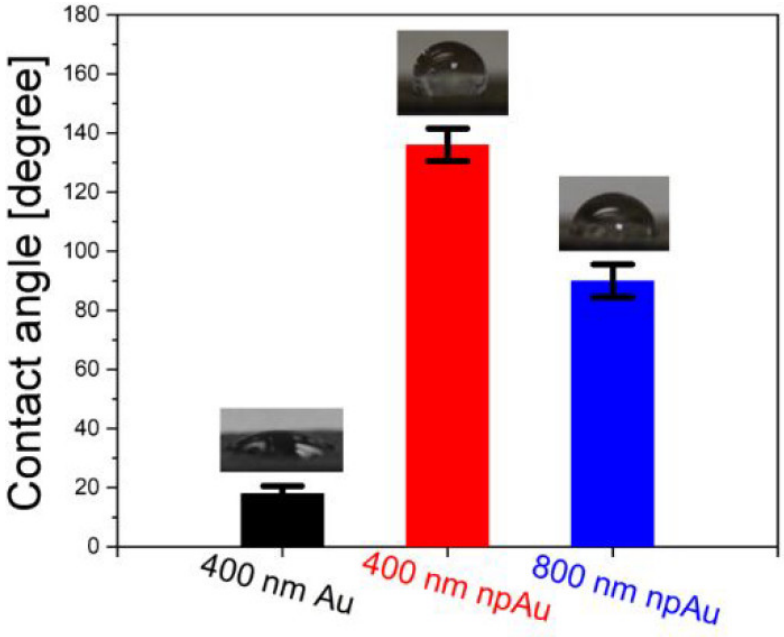

Figure 14: Measured contact angles for 400 nm Au, 400 nm nanoporous Au (npAu), and 800 nm npAu samples[39]

This shift in wettability correlates with improved performance: the CO Faradaic efficiency increased from 70% for MS Au to 88% for the 800 nm npAu coating at 100 mA/cm^2, with enhanced partial current densities and operational stability also observed (Figure 15). Moreover, npAu reduces contact resistance and optimizes triple-phase boundaries, achieving 45% energy efficiency for CO production (vs. lower values for MS Au) (Figure 15).

The thicker npAu coatings (800 nm) retain mesoscale agglomerates from sputtering, which slightly reduce hydrophobicity compared to thinner npAu (400 nm). However, this structure enhance CO_2 diffusion pathways, balancing wettability and gas transport[39].

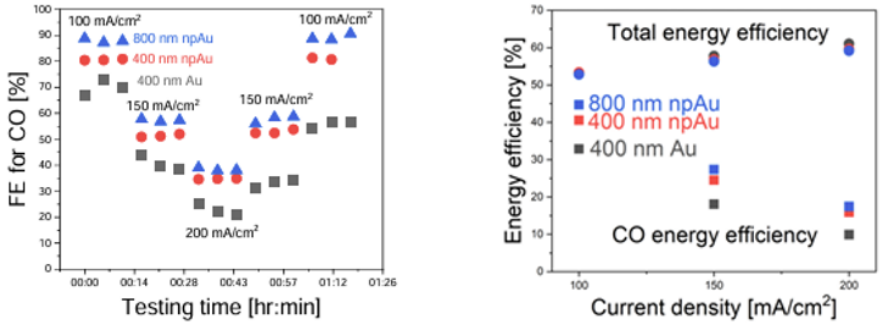

Figure 15: (Left) Durability assessment of 400 nm Au, 400 nm npAu, and 800 nm npAu catalyst films, conducted by increasing the current density from 100 to 200 mA/cm^2 and subsequently reducing it back to 100 mA/cm^2. (Right) Overall energy efficiency and CO-specific energy efficiency for 400 nm Au, 400 nm npAu, and 800 nm npAu at current densities of 100, 150, and 200 mA/cm^2[39]

Apart from morphology, pore size also affects hydrophobicity, as evidenced by recent work by Senocrate et al. In their study, the authors showed that tuning the pore size of

the GDE polymer substrate—using PTFE and PVDF materials with pore sizes ranging from 0.2 to 3 μm—strongly influences both the wetting behavior and the CO_2 reduction performance. By correlating the water entry pressure (WEP) with the electrodes' selectivity and stability, they found that substrates with low WEP (i.e., more easily wetted surfaces) exhibit poor CO selectivity ($\leq 30\% at 100\ mA/cm^2$) and reduced stability (only 65% retention of initial selectivity after 3 h).

In stark contrast, GDEs with higher WEP maintain a highly hydrophobic character, yielding up to 95% CO selectivity at 100 mA/cm^2 and nearly 97% selectivity retention over more than 40 h of operation, while also showing enhanced resilience to surface Cu contaminants (Figure 16)[43]. These findings underscore that optimizing pore size to achieve a high WEP is a powerful, scalable strategy to enhance both wettability control and overall CO_2 reduction performance.

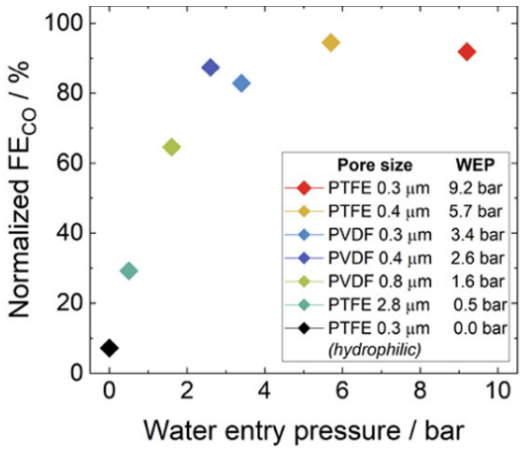

Figure 16: Correlation between Water Entry Pressure (WEP) and CO Faradaic Efficiency (FE_{CO}) for PTFE and PVDF-based gas diffusion electrodes (GDEs) with varying pore sizes[43]

2.6 Electrowetting

In previous sections, electrolyte composition, pore size, and catalytic materials were explored as key parameters for controlling wetting phenomena. Building on that foundation, this section delves into electrowetting—a dynamic and reversible method for modulating the wettability of nanoporous systems via applied electric fields.

Hydrophobic nanopores, by design, favor a dewetted state; their walls are often functionalized with hydrophobic groups, which, in the absence of external stimuli (such as pressure or voltage), result in the pore being filled with water vapor rather than liquid. This inherent property makes hydrophobic nanopores excellent candidates for "gating" applications, where the transport of water and dissolved species can be effectively switched on or off. When an electric field is applied, it induces alignment of water dipoles within the nanopore. This reorientation increases the local water density, eventually overcoming the hydrophobic barrier and initiating the transition from a dewetted (closed) state to a wetted (open) state[37].

The advantage of electrowetting lies in its non-invasive nature: it enables precise control over nanoscale transport without necessitating any structural modifications to the pore membrane. This principle has been demonstrated in both robust synthetic systems

and delicate biological channels, making it a versatile tool in the design of next-generation nanofluidic devices, sensors, and energy conversion technologies.

2.6.1 Wetting Under Electric Field

Under an applied electric field, an electric double layer (EDL) forms at the solid–liquid interface. The EDL comprises a compact Stern layer—divided into the inner Helmholtz plane (IHP) for strongly adsorbed ions and the outer Helmholtz plane (OHP) for more loosely bound ions—and a diffuse layer. Solvated cations accumulate near the negatively charged electrode over a few nanometers (approximately the Debye length)[29], although factors like ion–ion interactions and steric effects add complexity[17].

Electrowetting is quantified by Lippmann–Young's equation (Equation 1), which relates the contact angle under an applied field (θ_E) to the intrinsic contact angle (θ_0) in the absence of an electric field.

In essence, as the applied field increases (or deviates from E_{PZC}), water dipoles align and pack more densely at the interface. At the same time, there is a decrease in solid–liquid interfacial free energy due to the adsorption of counterions and desorption of co-ions at the interface, reducing the contact angle and promoting wetting[47].

This enhanced wetting is more pronounced on conductive surfaces, such as catalysts and carbon blacks in gas diffusion layers—where thin EDLs (<50 nm) allow rapid transitions—compared to dielectric materials like PTFE, which retain their hydrophobicity due to lower dielectric constants and thicker coatings[29]. Incorporating dielectric hydrophobic materials can help preserve gas pathways and reaction zones. However, electrically conductive materials in MPLs may promote wetting under an electric field, potentially leading to flooding. Therefore, an optimal combination and proportion of these two materials is required for the application of electrowetting.

It is important to note that an electric field can also alter the surface chemistry and morphology of the solid phase, thereby affecting wetting behavior. A study by Yang et al. has shown that under cathodic conditions, changes such as the loss of C–F bonds and an increase in oxygen species at the GDL surface can occur—effects attributed to the degradation of PTFE[59]. These modifications have been linked to alterations in wettability in catalyst layers. While the broader electrowetting literature spans numerous experimental and theoretical studies, in the context of this thesis the focus is limited to molecular-level insights relevant to confined electrochemical interfaces.

In this regard, the work of Taherian et.al [48] provides a useful reference, as it employs atomistic simulations to investigate nanoscale wetting and interfacial structuring under applied potentials. While Taherian et al. do not explicitly account for hydrophobic–hydrophilic boundary effects, their study provides a detailed molecular dynamics investigation into nanoscale electrowetting on graphene by focusing on the role of interfacial tension and local liquid structure near the three-phase contact line. In their work, liquid bridges of pure water and 4 M NaCl aqueous solution are confined between oppositely charged graphene sheets, with the setup depicted in Figure 17.

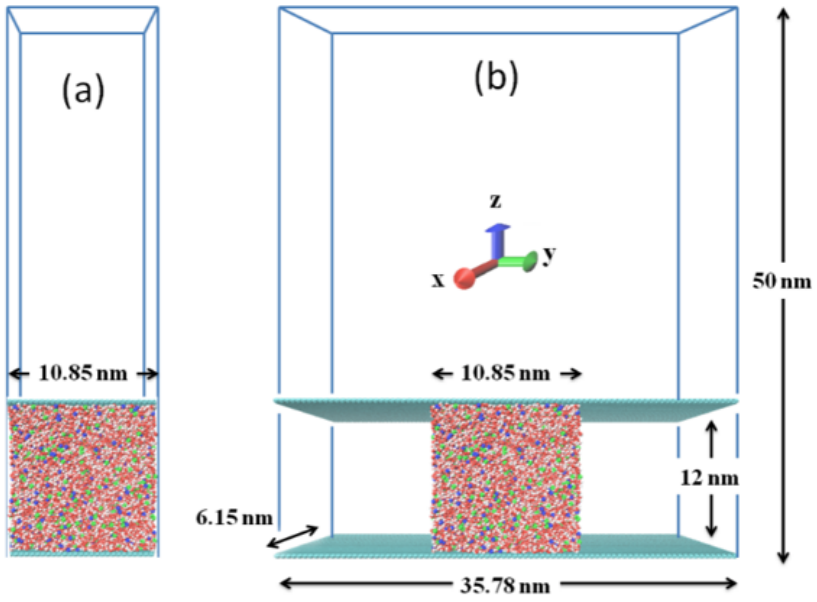

Figure 17: Simulation configuration showing (a) the initial system geometry and (b) the arrangement used for contact angle determination[48]

They measured the static contact angles under various surface charge densities and observed a pronounced asymmetric dependence on the polarity of the applied electric field. When the change in solid–liquid interfacial tension ($\Delta\gamma_{SL}$) was computed via thermodynamic integration, it remained nearly symmetric for both pure water and aqueous NaCl solution(as detailed in Figure 18)[48].

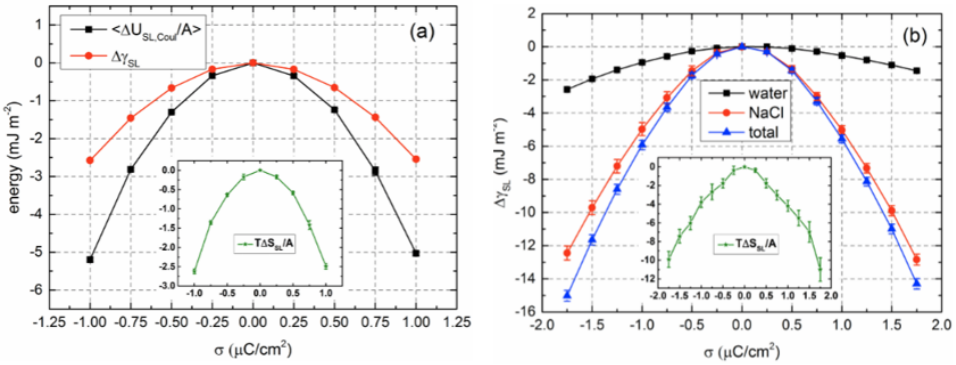

Figure 18: (Left) Solid–liquid Coulomb energy and variation in solid–liquid interfacial tension for pure water, and (Right) variation in solid–liquid interfacial tension for the 4 M NaCl solution[48]

If one were to calculate the contact angle from these $\Delta\gamma_{SL}$ values using the Young–Lippmann equation, the prediction would be that both fluids should exhibit a symmetric response. Yet, as shown in Figure 19, the observed behavior is the opposite: both fluids display an asymmetric contact angle.

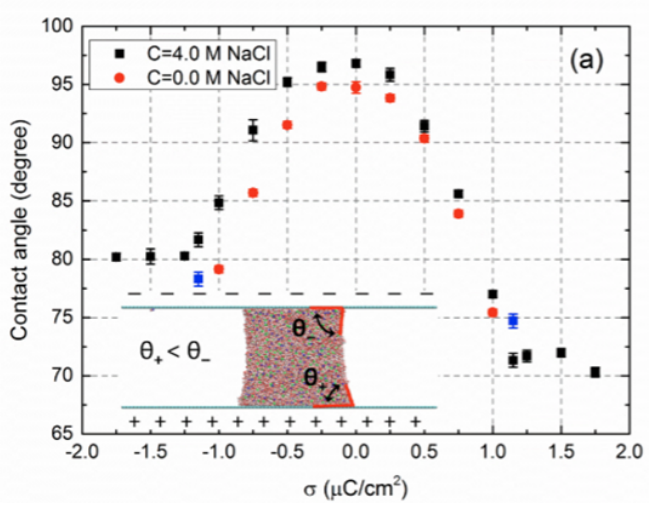

Figure 19: Contact angles measured at various surface charge densities (σ) for 12 nm thick bridges of pure water (red markers), 4 M NaCl (black markers), and for a 68 nm thick bridge of 4 M NaCl (blue markers)[48]

This discrepancy leads them to conclude that macroscopic interfacial tension changes cannot solely account for the observed electrowetting behavior. Instead, their analysis reveals that molecular-scale phenomena at the triple-phase boundary play a crucial role. Figures 20 illustrate that, in the region adjacent to the contact line, water molecules exhibit significant reorientation and disorder compared to the bulk—water dipoles, which are normally aligned parallel to the surface away from the contact line, show a marked transition in orientation near the boundary.

Additionally, the asymmetry also arises from ion-specific hydration and redistribution near charged interfaces. Sodium ions (Na^+), being smaller and more strongly hydrated than chloride ions (Cl^-), face higher dehydration energy loss when drawn toward negatively charged surfaces, limiting their migration to the contact line—a low-water-density region. Conversely, Cl^- ions, with weaker hydration, more readily relocate to positively charged surfaces, gaining electrostatic energy without significant dehydration. Simulations reveal Cl^- accumulation near the contact line on positive surfaces (Figure 21b), while Na^+ remains excluded on negative surfaces, explaining the enhanced spreading magnitude for positive charging.

Note also in Figure 21 the reduction in the number density of ions beyond $z = 1\ nm$ between $\sigma = 0\ \mu C/cm^2$ and $\sigma = +1\ \mu C/cm^2$ in the contact line area, which is not seen between $\sigma = 0\ \mu C/cm^2$ and $\sigma = -1\ \mu C/cm^2$[48]. These observations may explain why spreading is observed with a larger magnitude on the positive surface. This hydration-dependent ion mobility, coupled with interfacial water structure, underpins the observed asymmetry.

Understanding the nanoscale distribution of ions and CO_2 is essential for uncovering the underlying mechanisms that govern contact angle changes and interfacial behavior in electrochemical systems. As shown in Taherian et al.[48], ion distribution near the triple-phase boundary significantly affects the local electric field, water structure, and interfacial tension. These molecular-level changes directly impact wettability and can lead to variations in contact angle, especially under applied electric fields. Similarly, the study by Du et al. highlights how the distribution of CO_2 within confined nanopores influences adsorption capacity and interfacial free energy. CO_2 molecules do not distribute

uniformly; instead, their arrangement depends on factors such as surface charge and water content, which in turn affect how readily CO_2 can be captured or react at catalytic interfaces[12].

Together, these findings underscore the importance of using molecular dynamics simulations to resolve spatial distributions of ions and CO_2 near the contact line. Such insights are crucial not only for understanding wetting behavior but also for improving the design of electrochemical systems. This thesis will build upon that foundation by simulating how electric field variations affect both ion and CO_2 distribution and their combined influence on the contact angle at the nanoscale—an area that remains underexplored and holds significant potential for further research and technological advancement.

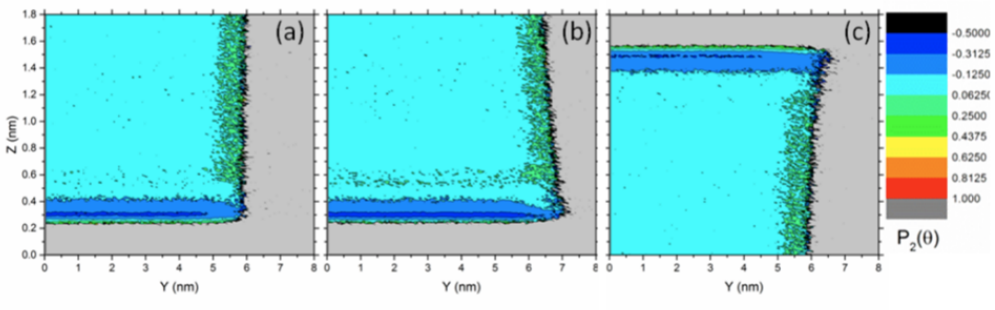

Figure 20: Water dipole moment orientation relative to the surface normal at $\sigma = 0\ \mu C/cm^2$ (a), $\sigma = +1.0\ \mu C/cm^2$ (b), and $\sigma = -1.0\ \mu C/cm^2$ (c)[48]

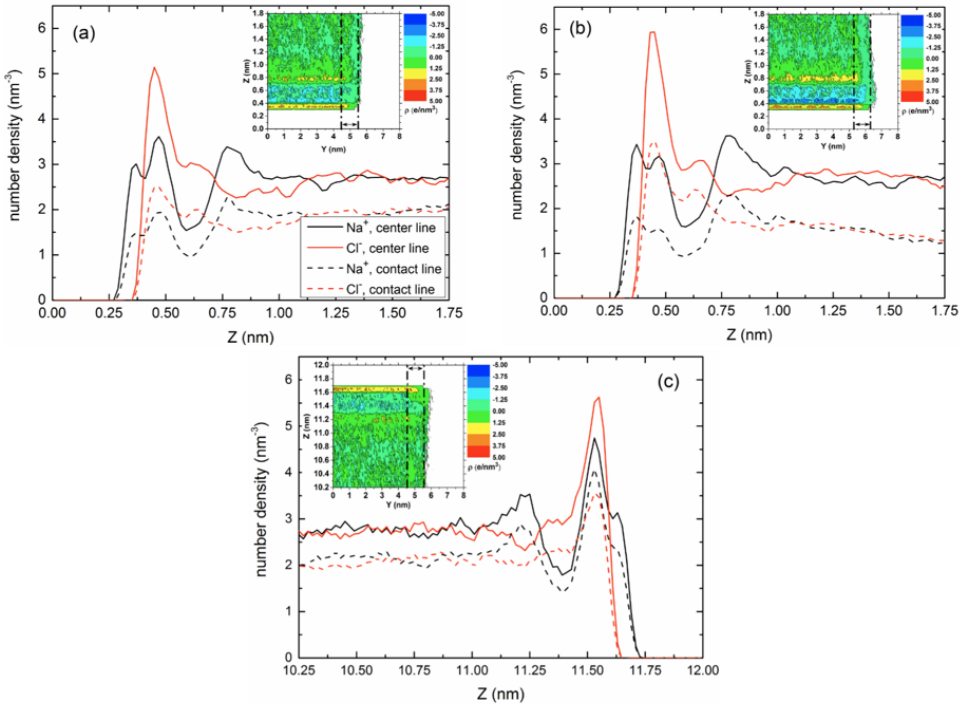

Figure 21: Number density profiles of sodium (black) and chloride (red) ions at the center region (solid curves) and the contact-line region (dashed curves) for $\sigma = 0\ \mu C/cm^2$ (a), $\sigma = +1.0\ \mu C/cm^2$ (b), and $\sigma = -1.0\ \mu C/cm^2$ (c). The insets depict the liquid's volume charge density arising from the ions. The dashed vertical lines mark the spatial interval defined as the contact-line region[48]

2.7 Why MD?

Molecular dynamics (MD) simulations are indispensable for resolving nanoscale interfacial phenomena in systems such as hydrophobic/hydrophilic junctions and triple-phase boundaries, where continuum models fail to capture molecular-scale interactions (for brief introduction to what MD is, readers are guided to Appendix C). Johnson and Haussener[25] present a detailed comparison between traditional continuum models—specifically, Poisson–Nernst–Planck (PNP) and its size-modified variant, GMPNP—and constant-potential molecular dynamics (MD) simulations. Their results highlight a fundamental gap: continuum approaches are effective for bulk-scale modeling but fail to capture complex, molecular-scale interfacial structures. The report explores the disparities between the two approaches while pointing to their relevance in our respective scenario.

Oscillatory Potential vs. Smooth Profiles Continuum models assume that water polarization and electrode–solute interactions can be averaged out and approximated by a uniform relative permittivity. Consequently, the potential profile in continuum theory tends to rise (or fall) smoothly from the bulk value to the electrode. In contrast, Figure 24a from Johnson and Haussener's work clearly shows multiple oscillations in the local potential extending up to approximately 8–9 nm into the solution. These oscillations originate from layers of polarized water molecules alternating with ions that partially lose or preserve their hydration shells. Traditional continuum equations cannot naturally incorporate the discrete layering of water molecules—each carrying partial charges—or

the induced (image) charges in the metal surface. As a result, continuum models predict a single, monotonic potential drop, whereas MD uncovers repeated sign changes that reveal genuine physical layering of charge and solvent structure.

Inner vs. Outer Adsorbed Ion Layers A key highlight is the formation of dual cation layers at the negatively charged electrode. In Figure 24b, the MD results show a double-peak in cation concentration: an inner layer where some K^+ ions are closely adsorbed (peak at 2.6 Å) and some rest further away (peak at 4.6 Å), with the concentration eventually decaying to the bulk value away from the electrode. This phenomenon arises because the metal electrode, modeled with the constant potential method (CPM), can dynamically redistribute charge in response to ionic proximity. The positive ions induce image charges in the metal, attracting the ions even more strongly to the surface. In the inner adsorbed layer, the electrostatic attraction is so strong that water molecules are partially stripped away, allowing closer contact with the electrode. Continuum PNP or GMPNP models, on the other hand, treat ions as continuous charge distributions and typically assume only one layer (the outer Helmholtz plane) without partial hydration changes. Consequently, it appears that the continuum models present a simplified picture of the EDL by neglecting many of these molecular length-scale phenomena within several angstroms of the surface.

Cation Identity and Hydration Johnson and Haussener highlight how the size and hydration properties of Li^+, Na^+, K^+, and Cs^+ dramatically affect their adsorption. Larger ions (e.g., Cs^+) exhibit stronger, closer adsorption in the inner layer because their hydration shells are more easily distorted than those of smaller ions (like Li^+). MD pinpoints this effect by looking at radial distribution functions and coordination numbers: the number of water oxygens bound to each ion decreases substantially in the inner layer, whereas continuum approaches simply lump all ions into a fixed "steric diameter" without capturing changes in hydration energy or shell distortion.

CO_2 Behavior and "Steric Crowding" Misconceptions From a reaction-environment standpoint, Figures 24 and especially 23 demonstrate that MD simulations find increased CO_2 density near the electrode—due to van der Waals attraction and electrostatic interactions—even when cations are present at high concentrations. Continuum GMPNP, by contrast, often predicts that cations "crowd out" CO_2 entirely if the ion packing limit is approached. In practice, Johnson and Haussener show that no such dramatic exclusion occurs; CO_2 actually accumulates near the metal surface in MD. This discrepancy is especially relevant for our systems aiming to promote CO_2 availability at triple-phase boundaries; using continuum theory alone may incorrectly suggest that CO_2 molecules cannot penetrate cation-rich regions.

Constant Potential Method vs. Fixed Charge Method Within MD, the authors also highlight the importance of the method used. Figure 22 underscores the importance of CPM within MD. By letting each electrode atom's charge adjust in real time to the local environment, CPM captures induced polarization at the metal surface—a driving factor for strong ion adsorption, local restructuring of water, and enhanced CO_2 accumulation. Older "fixed charge" MD approaches systematically underestimate these effects because they cannot replicate image-charge phenomena. In the past, implementing CPM in MD may have been too onerous for many researchers, but as of May 2022,

the LAMMPS-ELECTRODE package makes using CPM very straightforward. Furthermore, continuum models, likewise, treat the electrode as a boundary condition and cannot represent dynamic charge rearrangements at each metal atom, which become critical at the nanoscale.

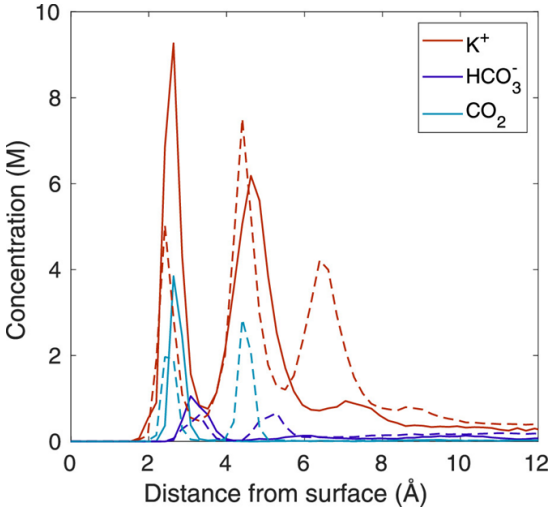

Figure 22: Species concentration profiles comparing CPM (solid curves) and FCM (dashed curves) for $q = 30$ and $KHCO_3$[25]

Implications for Contact Angles and Triple-Phase Boundaries The ability of MD to resolve local water orientations, partial dehydration, and van der Waals forces is precisely why it is so powerful for studying contact angle variations in nanopores with hydrophobic/hydrophilic junctions. At triple-phase boundaries, a small change in water structure—say, a reorienting hydrogen-bond network—can shift local wettability, as observed in [48]. Continuum methods, which average out solvent polarization, cannot portray these subtle reorganizations, thereby missing the precise conditions that lead to changes in contact angles, especially when CO_2 partitioning also depends on local solvation structures.

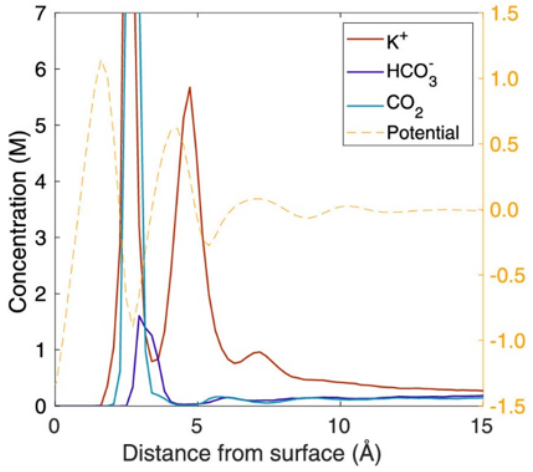

Figure 23: CO_2 concentration profiles for $KHCO_3$ with 60 CO_2 molecules simulated, corresponding to five times the base-case amount$_3$[25]

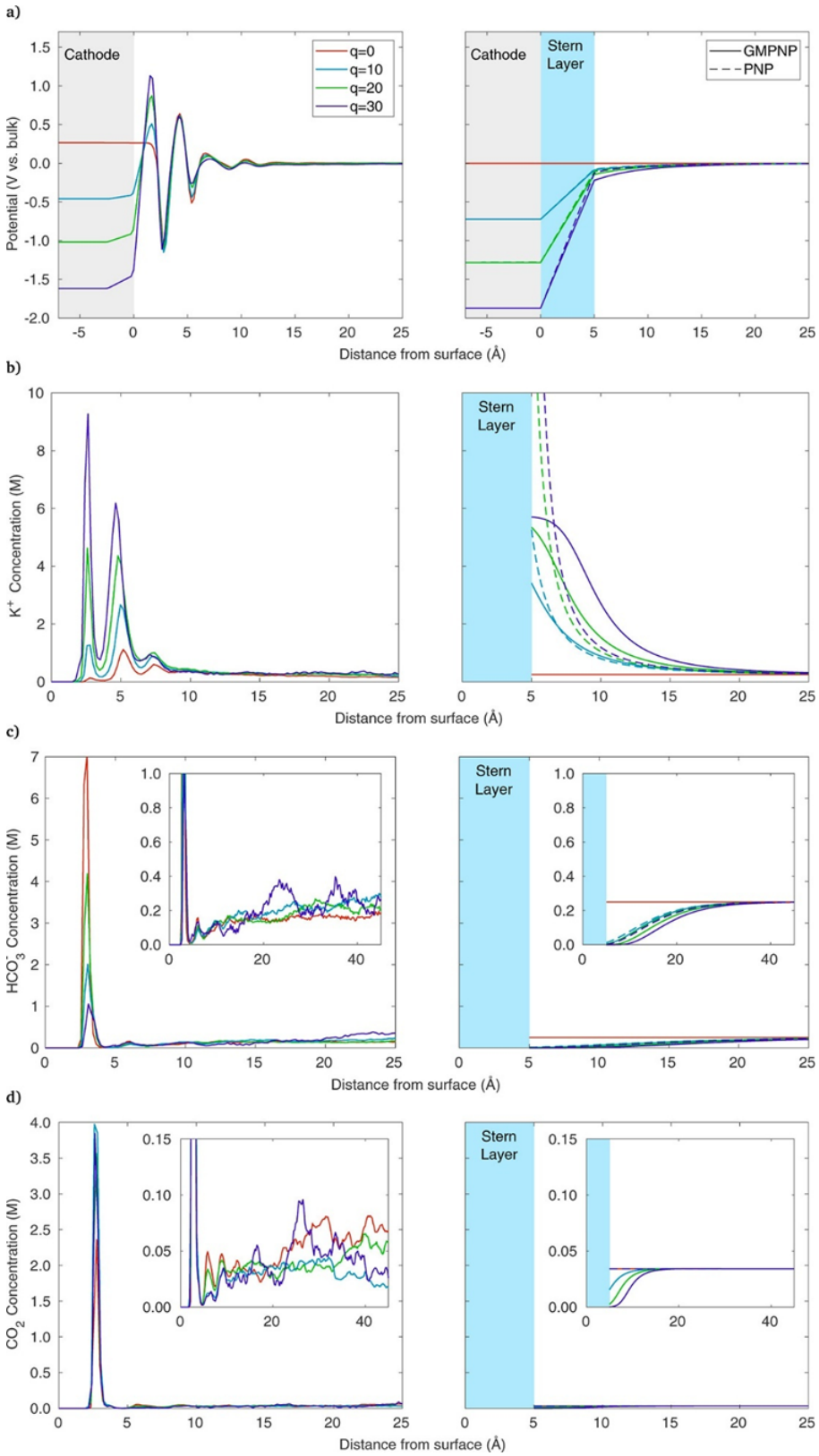

Figure 24: Comparison of molecular dynamics (left panels) and continuum model results (right panels), illustrating (a) potential relative to the bulk, and concentrations of (b) K^+, (c) HCO_3, and (d) CO_2. The distance axis is referenced from the center of the Au atoms at the electrode–electrolyte interface. The shaded blue area indicates a 5 Å Stern layer, while the cathode is depicted in gray[25]

3 Research Plan

3.1 Research Objective and Scope

The objective of this thesis is to investigate how surface potential influences wettability and CO_2 distribution in a nanopore system using molecular dynamics (MD) simulations. The system consists of a slit-type nanopore with a hydrophilic/hydrophobic junction, filled with a fluid mixture of water, CO_2, potassium (K^+), and bicarbonate (HCO_3^-) ions.

By systematically varying the surface charge density, the study aims to understand how the resulting electrostatic fields affects interfacial water structure, ion distributions, and CO_2 localization near solid-liquid interfaces. Special attention is given to the behavior at the triple-phase boundary and the role of molecular interactions that are not captured by continuum models.

The scope of this study is limited to MD simulations under static conditions, without chemical reactions, as the typical simulation timescale ($\sim$10 ns) is several orders of magnitude shorter than those associated with electrochemical reaction events. As stated by pierce *et al.* [35], conventional molecular dynamics generally accesses only tens to hundreds of nanoseconds, whereas many reaction processes occur on microsecond–millisecond timescales or longer. Recent advances in machine-learning-accelerated MD, as demonstrated by Tian *et al.* [49] in a current working paper, have begun to bridge this gap. The simulations focus on a single-pore system, evaluating how surface potential modulates wetting behavior, ion layering, and CO_2 accessibility. These insights are relevant for enhancing reactant accessibility, improving interfacial stability, and optimizing overall performance in electrochemical CO_2 conversion systems.

3.2 Research Questions

1. **How does CO_2 availability at the reaction site vary with applied surface potential in confined environments?**
   Rationale: This will be explored by studying how CO_2 distribution shifts within a nanopore under varying electrode voltages using molecular dynamics simulations.

2. **How does ion structuring near charged surfaces evolve with applied potential, and what impact does this have on interface stability in nanoporous systems?**
   Rationale: The simulations will examine voltage-dependent ion layering and charge separation near solid–liquid interfaces, providing insight into how interfacial electrostatics shape local environments.

3. **How do molecular-scale predictions of reactant transport and partitioning compare with continuum theoretical models in nanoporous electrochemical systems?**
   Rationale: This comparison will test the limits of traditional continuum theories in capturing ion and molecule behavior under extreme confinement and strong interfacial fields.

The answers to these research questions will provide insight into how surface potential and ion behavior affect wetting dynamics and species availability at the triple-phase

boundary in confined environments. These findings aim to improve the understanding of interfacial control in nanoporous systems, with relevance to CO_2 electrolysis applications.

4 Methodology

4.1 Simulation Overview

This study utilizes classical Molecular Dynamics (MD) simulations to examine how applied surface potentials modulate wettability and influence CO_2 and ion distribution at nanoscale hydrophilic–hydrophobic junctions. MD offers a powerful framework to capture dynamic interfacial behavior at molecular resolution, such as water structuring and ion layering, that are not captured by continuum theories.

The simulation framework is implemented in LAMMPS[36] with the inclusion of a constant-potential electrode algorithm[4] to mimic electrochemical boundary conditions. Long-range electrostatics are computed using slab-corrected Particle–Particle Particle–Mesh (PPPM)[22] summation to appropriately treat the nonperiodic nature of the confined geometry.

The methodology that follows is divided into two main parts. First, in Section 4.1, the molecular model is described in detail, including system composition and box dimensions, surface functionalization strategy, force field parameters, and the implementation of constant-potential boundary conditions. Then, Section 4.2 outlines the simulation protocol: beginning with system construction using Packmol, followed by energy minimization, equilibration, and finally the voltage-controlled production runs used for data collection and analysis.

4.1.1 System Composition and Box Size

To investigate the impact of surface potential on interfacial wetting and molecular distributions in confined liquid systems, we constructed a slit-pore geometry consisting of an aqueous electrolyte confined between two planar solid walls. It represents an ideally wetted single pore in the catalyst layer and enables direct observation of triple-phase boundary phenomena, ion layering, and wetting transitions.

The simulation domain was designed as a rectangular box approximately 114 Å × 40 Å × 106 Å in size. It was centered at the origin and featured periodic boundary conditions along the x and y directions, while the z direction contained two stationary solid slabs that confined the fluid. To study spatially varying surface interactions, the inner wall surfaces were chemically patterned: a central hydrophilic region (20.394 Å to +20.394 Å along y) was flanked by hydrophobic zones, allowing investigation of electrowetting at heterogeneous interfaces. The configuration of the simulation domain, including the chemically patterned walls, is illustrated in Figure 25.

The confined electrolyte consisted of:

- 4990 water molecules modeled using the SPC/E[6] model, yielding a bulk density near 0.99 g/cm^3 at 298 K.
- 45 potassium (K^+) and 45 bicarbonate (HCO_3^-) ions, approximating a bulk concentration of 0.5 M $KHCO_3$ with 1:1 stoichiometry for charge neutrality.
- 12 CO_2 molecules were considered. The Henry's law solubility of CO_2 in 0.5 M aqueous $KHCO_3$ at 1 bar and 298 K corresponds to approximately nine CO_2 molecules within the simulated volume. A larger number of CO_2 molecules were included in the system to ensure meaningful sampling of solvation behavior and to enable statistical analysis of solubility trends.

The total fluid composition and box volume were selected to maintain atmospheric pressure and an electroneutral environment, consistent with mild CO_2RR operating conditions. The resulting number density matches expected values for liquid water systems, ensuring physically realistic structuring.

The solid walls consisted of crystalline gold (Au) slabs constructed with face-centered cubic (FCC) (100) orientation, 3 atomic layers thick. Initially, wall atoms were fixed in space to mimic rigid electrodes, and the wall spacing was set by design; together with the target concentration, this was used to determine the number of molecules in the simulation.

To ensure electrostatic consistency in this slab geometry, long-range Coulombic interactions were computed using two-dimensional periodic boundary conditions, with corrections applied to remove artificial dipole contributions in the confinement direction.[1]

Note: A detailed table listing system quantities, such as atom counts, simulation box dimensions, concentrations, and justifications, is provided in Appendix A.

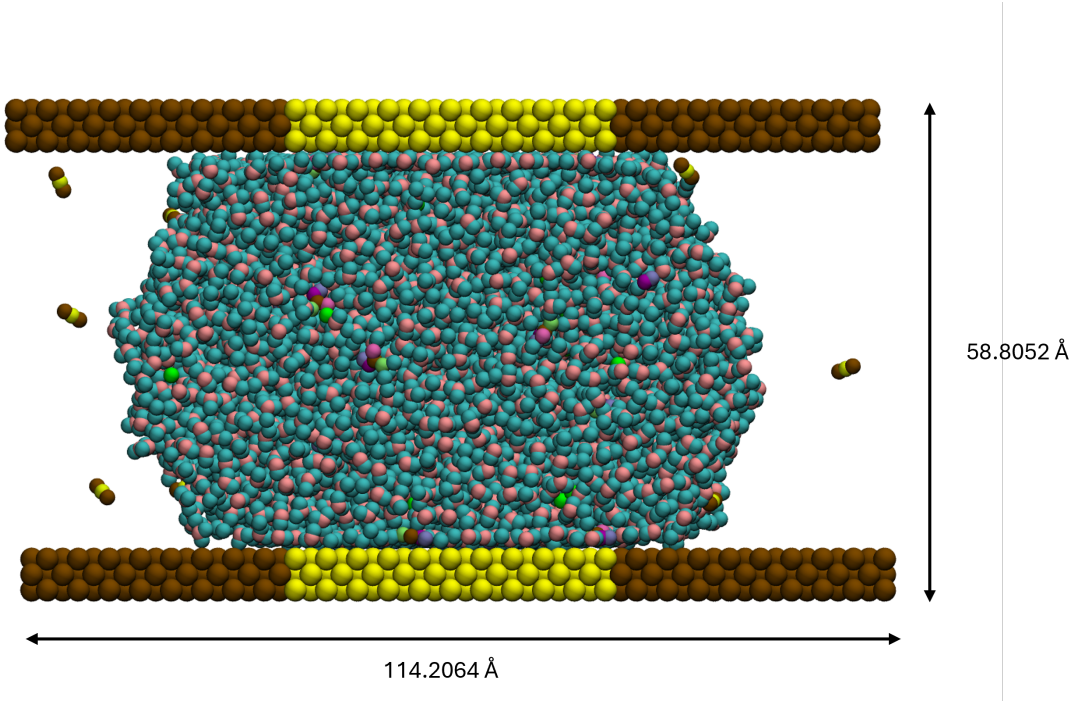

Figure 25: Simulation box with fluid confined between patterned gold walls. Hydrophilic (yellow) and hydrophobic (brown) regions are shown; box dimensions are labeled.

4.1.2 Electrode Surface Composition

The confining solid walls were constructed using gold atoms arranged in a face-centered cubic (FCC) lattice, with a lattice constant of 4.0788 Å. These walls were symmetrically positioned about the $y = 0$ midplane and acted as rigid boundaries for the confined fluid.

The wall surfaces were modified to create distinct hydrophilic and hydrophobic regions. This was achieved by tuning the strength of wall–fluid interactions, specifically

[1]For example, in LAMMPS, this is handled via slab-corrected Ewald summation (e.g., `kspace_style pppm/electrode` with `slab` modifier). Equivalent approaches exist in other MD packages.

via modification of the Lennard–Jones (LJ) interaction parameters that govern van der Waals forces between wall atoms and surrounding fluid species.

Hydrophilic region (consisting of Au Atoms) interaction parameters were adopted from Heinz et al. (2008)[19], who fitted Lennard-Jones potential parameters for FCC metals to accurately reproduce experimental densities and surface/interfacial energies under ambient conditions (a brief explanation of Lennard-Jones potential is provided in Appendix B). For the hydrophobic zones, literature values were consulted primarily to gauge the typical range of Lennard–Jones parameters for hydrophobic surfaces, with limited further optimization since this was not the main focus of the thesis. In particular, reference was made to a study where such parameters were taken from established force fields and validated through molecular dynamics simulations of water wetting on fluorinated solid surfaces [10].

The functionalisation was spatially patterned along the lateral axis (x), with a central hydrophilic zone flanked by hydrophobic entrances and exits. This configuration emulates nanopatterned electrode surfaces commonly found in electrocatalyst platforms, and facilitates the study of wetting transitions, triple-phase boundary formation, and field-induced redistribution.

A full breakdown of the wall atom types, interaction parameters, and source justification is provided in Appendix A.2.

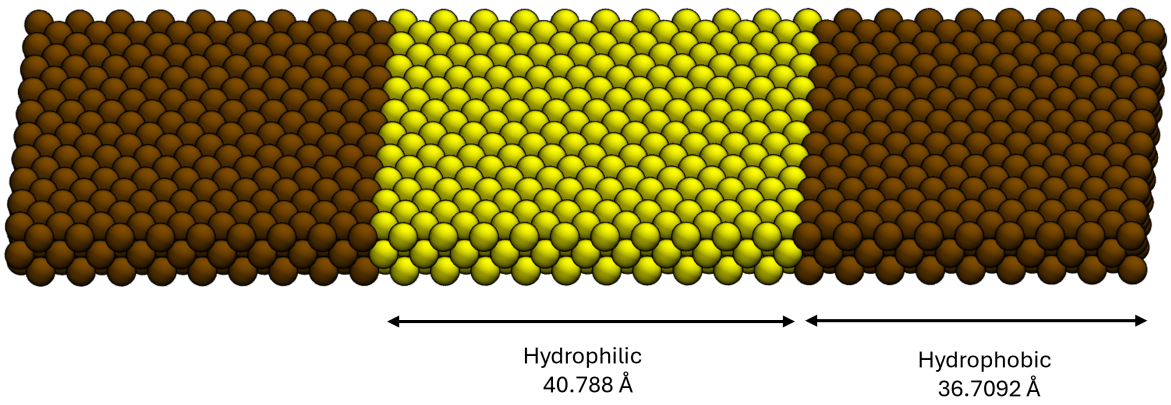

Figure 26: Patterned wall surface showing spatially separated hydrophilic and hydrophobic regions. The central hydrophilic zone spans 40.8Å, flanked by hydrophobic segments.

4.1.3 Force-Field Parameters

Atomic interactions in the system were modeled using a combination of bonded and non-bonded classical potential functions commonly supported by most molecular dynamics platforms.

Non-bonded interactions. All atoms interacted via a combination of Lennard-Jones (12–6) potentials and Coulombic electrostatics. Lorentz–Berthelot mixing rules were applied for unlike pair interactions. A cutoff distance of 10 Å was imposed for the short-range van der Waals and real-space electrostatic components. Long-range electrostatics were treated using slab-corrected Ewald summation, which mitigates artifacts arising from periodicity in the confinement direction[2]. Other electrostatic solvers, such as standard 3D Ewald summation or reaction field methods, were deemed unsuitable: the former assumes full three-dimensional periodicity, while the latter imposes spherical symmetry in dielectric screening, making both inaccurate for anisotropic, confined interfacial systems.[60].

Bonded interactions.

- **Water molecules** were modeled using a rigid geometry, with constraints applied to preserve O–H bond lengths and the H–O–H angle.[3]. This allowed the use of a 1 fs integration timestep without compromising structural stability.
- **Carbon dioxide (CO_2)** was treated as a rigid linear triatomic species, with fixed bond lengths and angles as defined in the García-Sánchez *et al.* force field[54].
- **Bicarbonate ions (HCO_3^-)** bond, angle, and dihedral parameters adapted from the Zeebe et al force field.[61]

The complete list of force-field parameters, including ε, σ, and partial charges for all atom types, is provided in Appendix A.3. Although this setup was implemented in LAMMPS, the described parameter sets and interaction models are transferable to other MD engines (e.g., GROMACS, AMBER, OpenMM), with only format-specific differences in constraint definitions or long-range electrostatics.

[2]In LAMMPS, this is implemented via `kspace_style pppm/electrode 1.0e-5` and `kspace_modify slab 3.0`.

[3]Rigid constraints in LAMMPS were applied using `fix shake` for water and `fix rigid` for CO_2.

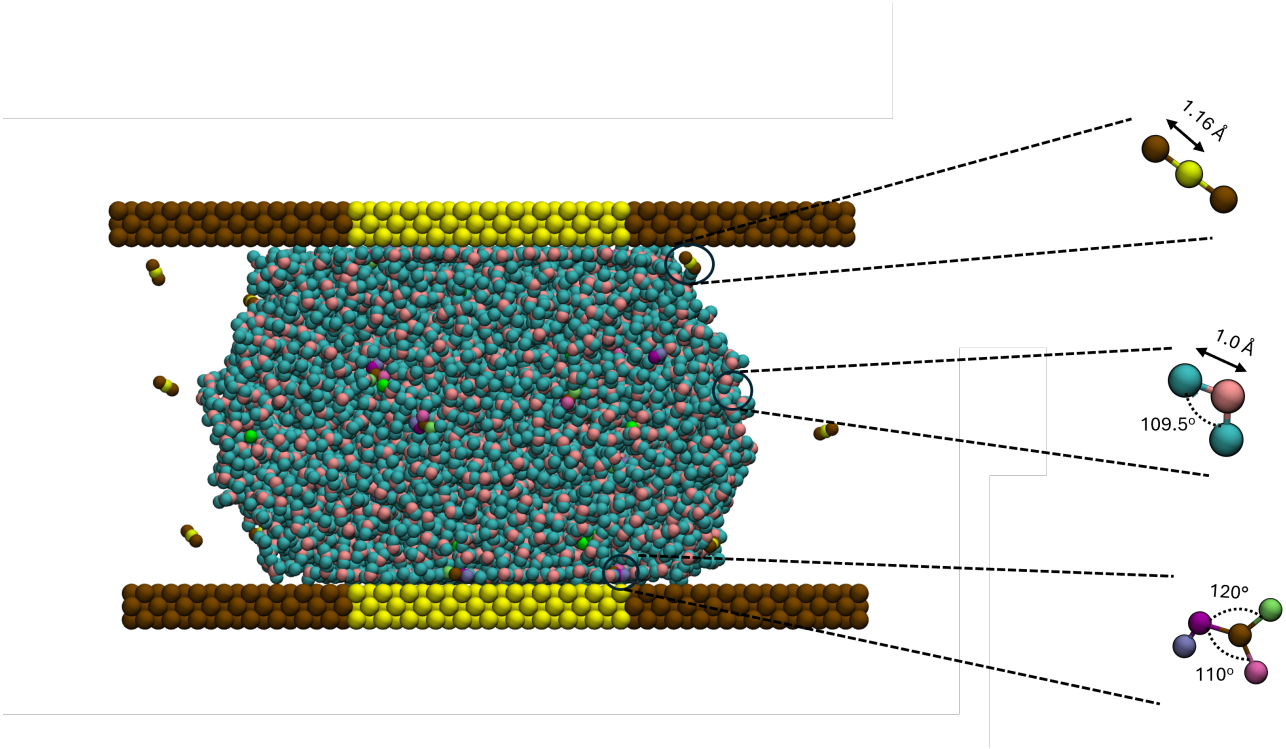

Figure 27: Rigid molecular geometries used in the force field. The figure shows bond angles and lengths for (a) H_2O, (b) CO_2, and (c) HCO_3^-

4.1.4 Constant-Potential Algorithm

In this study, electrode surfaces were modeled using the Constant Potential Method (CPM)[4], which allows metallic surfaces to maintain a fixed electrostatic potential while dynamically adjusting atomic charges. This behavior mimics that of an ideal conductor and is essential for accurately capturing field-driven interfacial phenomena.

Unlike traditional fixed-charge models where surface charges remain constant, CPM allows each electrode atom to redistribute its charge in response to its local electrostatic environment. This is essential to simulate:

- Image-charge effects (how metal surfaces attract counter-ions),
- Accurate structure of electrochemical double layers,

To enforce the constant potential condition, the simulation algorithm solves Poisson's equation at each timestep using a particle–particle particle–mesh (PPPM) solver with slab correction. A target potential Φ_{target} is imposed on the electrode, and the charges q_i on each electrode atom are optimized by solving the following constrained minimization problem:

$$\min_{\{q_i\}} \left[\frac{1}{2} \sum_{i,j} q_i G_{ij} q_j - \sum_i \Phi_{target} q_i \right]$$

where G_{ij} is the electrostatic Green's function. The necessary condition each electrode atom must satisfy is:

$$\sum G_{ij} q_j = \Phi_{target}$$

In this minimization form, the indices i and j run only over electrode atoms with variable charges. The contribution from fixed charges in the electrolyte is not written explicitly here; in practice, it is included separately as a known potential term when constructing the right-hand side of the CPM linear system. This ensures a uniform potential across the conductive surface regardless of electrolyte configuration. At each timestep, the CPM linear system was solved with a relative convergence tolerance of 1×10^{-6}.

The electrode surface was divided into two functional regions:

- **Hydrophilic electrode atoms**: confined to the central zone of the wall, treated as conductive and coupled to the constant potential algorithm.[4]
- **Hydrophobic wall atoms**: positioned at either end of the slit pore, remained electrostatically neutral and non-conductive throughout the simulation.

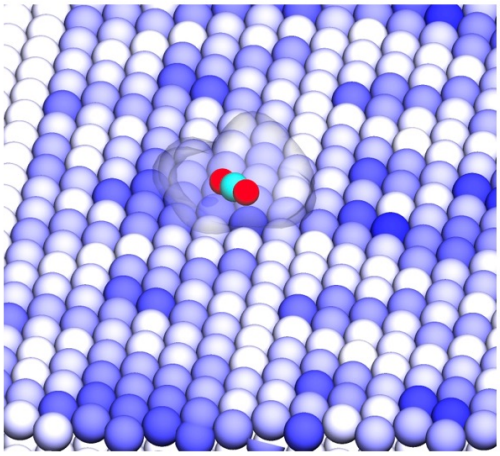

Figure 28: Visual representation of charge distribution on the bottom plate using CPM for the -2V case(cathode). Blue–white shading indicates spatially resolved surface charge. The surrounding electrolyte, which induces this distribution, is present in the simulation but omitted here for visual clarity

Alternative methods

Several commonly used electrostatic models were evaluated but found unsuitable for this study:

- **Fixed-charge models**: In this approach, each electrode atom is assigned a static charge (e.g., +0.1e), and the potential at any point in the electrolyte becomes an outcome of the simulation rather than an input. As ions and polar molecules rearrange near the surface, the local electrostatic potential fluctuates:

[4]Defined as a specific atom group coupled using `fix electrode` in LAMMPS.

$$\Phi(\mathbf{r}) = \sum_j \frac{q_j}{|\mathbf{r} - \mathbf{r}_j|}$$

Because the charges q_j remain fixed, the wall cannot maintain a constant potential and fails to behave as a true conductor. This undermines voltage control and produces physically inaccurate double-layer structures.

- **Uniform external electric field models**: Applying a background field across the entire simulation domain (e.g., via parallel-plate capacitor analogy) lacks any explicit conducting boundary. As a result, this model cannot simulate surface polarization, image-charge attraction, or potential-driven wetting effects.

Why CPM is essential for this work

To realistically simulate a metallic electrode under applied voltage, it is essential to enforce a constant electrostatic potential across the surface—reflecting the behavior of a true conductive plate. CPM provides the only physically consistent method in molecular dynamics to achieve this. It dynamically adjusts atomic charges in response to the surrounding electrolyte configuration, ensuring the electrode behaves as an equipotential surface throughout the simulation.

This is particularly important for:

- Maintaining voltage control rather than fixed surface charge, which is a prerequisite for simulating electrowetting,
- Resolving the electric double layer structure that forms near conducting surfaces,
- Capturing field-driven transport, ion migration, and wetting transitions triggered by applied potentials.

Although more computationally intensive than fixed-charge methods, CPM is essential to reproduce the correct electrostatic boundary conditions at electrode–electrolyte interfaces. Its accuracy is foundational for modeling voltage-controlled wetting and flooding behavior, central to the objectives of this thesis.

4.2 System Protocol

The simulation protocol describes the sequential steps used to prepare, initialize, and execute the molecular dynamics simulations based on the system model defined in Section 4.1. Beginning with molecular packing and geometry setup, the protocol includes system minimisation, thermal equilibration, and the application of surface-charge boundary conditions using the constant-potential method. Each simulation was conducted over a range of imposed surface-charge densities, allowing the influence of voltage-induced electrowetting to be systematically investigated.

4.2.1 System Build

The molecular system was designed to represent a slit nanopore with a central conductive (hydrophilic) region flanked by two non-conductive (hydrophobic) walls. The fluid domain consisted of water, CO_2, potassium (K^+), and bicarbonate (HCO_3^-) ions, while the walls were constructed from crystalline atoms arranged in face-centered cubic (FCC) lattices.

Fluid Region Packing with Packmol. The fluid-phase molecules were placed using Packmol, which enables dense molecular configurations inside confined geometries. With more than 5,000 molecules placed within a narrow slab, direct random insertion methods[5] were infeasible due to poor acceptance rates for atom/molecule insertion at high densities. Packmol's optimization routines minimized interatomic overlaps and allowed for complex polyatomic molecules to be positioned in realistic geometries.

Key features:

- Prevents atomic overlap via distance constraints,
- Handles multi-atom species (e.g., HCO_3^-, CO_2),
- Outputs PDB-format coordinates suitable for next step in simulation.

Molecules were packed into a cuboidal region with bounds: $x \in [-54.0, 54.0]$Å, $y \in [-20.0, 20.0]$Å, $z \in [-41.0, 41.0]$Å. The following molecules were placed uniformly in this volume:

Molecule Type	Count	Placement Volume	Notes
H_2O	4990	Full fluid region	SPC/E water model
CO_2	12	Full fluid region	Rigid triatomic
K^+	45	Full fluid region	Monovalent cation
HCO_3^-	45	Full fluid region	Anionic species

Each species was defined in a separate `.pdb` file with rigid geometries. A placement tolerance of 2.0Å and 1000 optimization loops ensured minimal overlap and uniform distribution. The final output from Packmol formed the geometric foundation for system assembly.

[5]For example, via `create_atoms random` in LAMMPS, which becomes inefficient at high density.

Bond Topology Generation in VMD. Packmol does not preserve or assign bond connectivity. To define intra-molecular bonds, a custom TCL script was used within VMD (Visual Molecular Dynamics), which imported template bonds from each species-specific PDB file and mapped them onto the packed systemwhich was used to build the complete bonded topology. This modular process ensured, Correct bonding and angle parameters from VMD and Compatibility with downstream force field parameterization.

Wall Construction in Lattice Coordinates. The solid wall atoms were built directly in lattice positions following a face-centered cubic (FCC) configuration, with a lattice constant of 4.0788Å. The simulation box dimensions were:

$$x \in [-57.1032, 57.1032] \quad y \in [-20.394, 20.394] \quad z \in [-53.0244, 53.0244]$$

Top and bottom wall slabs spanned the entire x–y plane and were divided functionally(Fig 26):

- The central region $z \in [-20.394, 20.394]$ was designated as the hydrophilic electrode and later assigned a target surface potential.
- The outer regions served as hydrophobic walls and remained electrically neutral. The dimensions were chosen in accordance with omiting periodic interactions and thereby getting stuck in meta-stable state.

Final Composition Summary.

Species	Count	Region	Function
H_2O	4990	Central pore	Solvent
CO_2	12	Throughout	Dissolved gas
K^+	45	Central pore	Electrolyte cation
HCO_3^-	45	Central pore	Electrolyte anion
Au (wall)	–	Top and bottom slabs	Solid substrate (hydrophilic/hydrophobic)

The top slab acted as a counter electrode to ensure charge neutrality in the simulation cell. This composite system, including packed molecules, bonded topology, and rigid wall structure (see Figure 29), was exported as a single `.data` file and passed to the energy minimization and equilibration stages detailed in the next section.

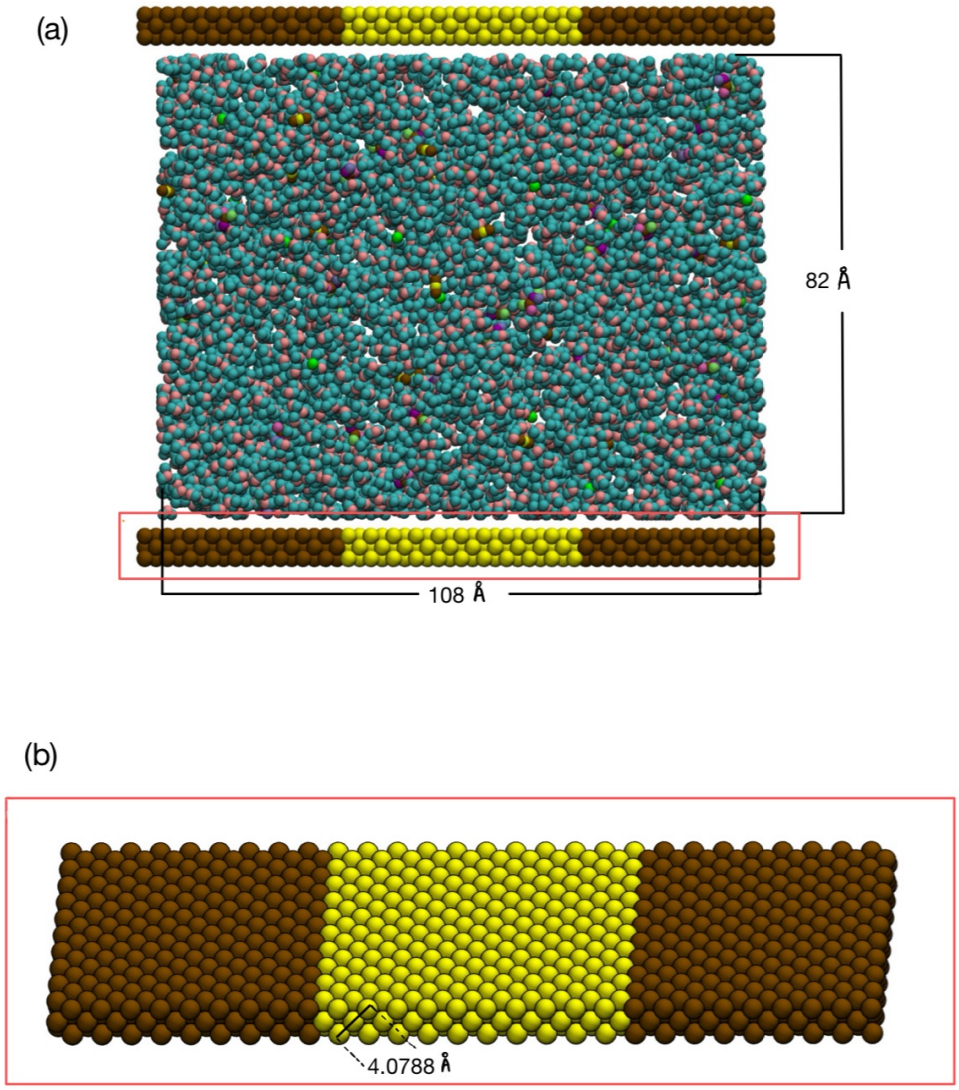

Figure 29: Initial system configuration and wall lattice structure. (a) Packed fluid configuration generated using Packmol, showing initial water height (82Å) and box width (108Å) prior to equilibration. Plates were generated separately using LAMMPS in FCC lattice positions. (b) Bottom wall slab highlighting the FCC structure with a lattice constant of 4.0788Å.

4.2.2 Energy Minimisation & Equilibration

After constructing the full system, molecular dynamics simulations were used to thermally equilibrate the fluid. In particular, this step allowed water, ions, and CO_2 to reorganize near the hydrophilic and hydrophobic surfaces, enabling spontaneous wetting.

Energy minimisation was performed using NVT ensamble. The initial structure gen-

erated by Packmol satisfied the insertion rules, such as the 2 Å minimum interatomic distance constraint.

Thermodynamic Parameters

Parameter	Value	Justification
Temperature	298.15 K	Ambient conditions
Timestep	1 fs	Stable with SHAKE and rigid-body dynamics
Equilibration time	8 ns	Confirmed via Potential-Energy convergence (see Fig. 30)

The Temperature was regulated using Nosé–Hoover Thermostat. Readers are guided to Appendix D for brief explanation.

Molecular Group Treatments Each group of atoms was assigned constraints or thermostatting appropriate to its physical behavior:

- **H_2O molecules** were treated using SHAKE[6] to preserve geometry and enable a stable 1 fs timestep. - **HCO_3^-, CO_2** were integrated as rigid bodies[7]. - **Wall atoms** were kept fixed throughout[8] to maintain surface structure.

Equilibration Duration The system was equilibrated over 8 ns. Figure 30 shows the potential energy trajectory, which rapidly decreases in the first 0.3 ns as system relax from their initial configuration, followed by a stable plateau after approximately 1 ns.

The absence of drift and bounded thermal fluctuations in potential energy confirms thermodynamic equilibrium. The final structure after 8 ns was used as the initial configuration for further equilibration.

Wall Relaxation and Fluid Height Adjustment Prior to voltage application, the top wall was allowed to move freely in the z-direction to reach mechanical equilibrium with the confined fluid. This ensured that all forces within the system were balanced, establishing a physically realistic meniscus height with near ambient pressure conditions. The top wall was constrained to move only along the z-axis with all other motions restricted. Any residual drift was removed, and the bottom wall remained fully fixed.[9]

This pre-relaxation ensured that all subsequent electrostatic effects during voltage application occurred from a mechanically relaxed initial configuration.

[6]Enforced using `fix shake` to constrain O–H bonds and H–O–H angles in SPC/E water.

[7]Implemented with `fix rigid/nvt/small`

[8]Applied via `fix setforce 0 0 0` to zero net force on wall atoms and preserve confinement geometry.

[9]The top wall was treated as a rigid group with translation allowed only along z using `fix rigid`, and momentum was zeroed via `fix momentum`. The bottom wall atoms were frozen using `fix setforce 0 0 0`.

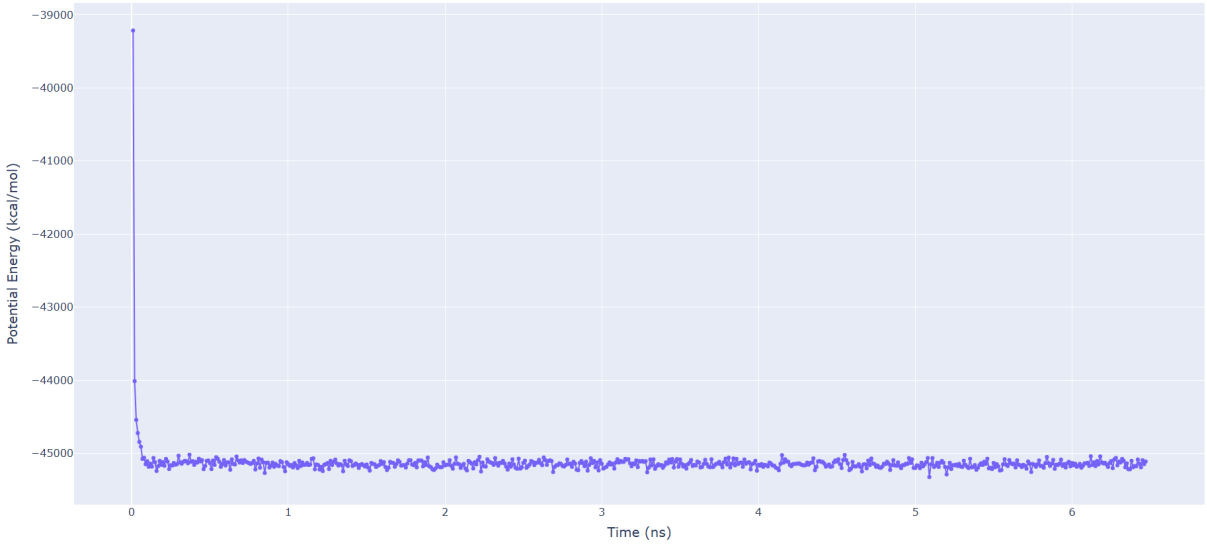

Figure 30: Potential energy profile during the 8ns equilibration run. The system exhibits rapid energy relaxation within the first nanosecond, followed by stable fluctuations, confirming thermodynamic equilibration.

4.2.3 Production Run

Following equilibration, the system was subjected to a series of production simulations to investigate electrowetting behavior under applied surface potentials. These runs were performed using the Constant-Potential Method (CPM) on the hydrophilic portions of the top and bottom walls, while fluid atoms evolved dynamically.

CPM on Mobile Electrodes: Solver and Rationale Electrostatic potentials were applied to the catalyst (hydrophilic wall atoms) using a constant-potential solver that dynamically adjusts atomic charges to maintain a fixed electrostatic potential. Equal and opposite potentials were assigned to the top and bottom. Readers are referred to Section 4.1.4 for a more comprehensive explanation.

This approach enables accurate charge redistribution in response to local electrolyte structure, particularly when the electrodes are mobile.[10]

Applied Potential Difference and Run Configuration Simulations were conducted under four voltage conditions to capture electrochemical and electrowetting effects:

Case	CPM Applied	Potential (V)	Duration
1	No	–	20 ns
2	Yes	0	20 ns
3	Yes	1	20 ns
4	Yes	2	20 ns

The selected voltages (0V, 1V, 2V) were chosen to represent a range of electrochemical and electrowetting regimes. In the context of CO_2 electroreduction, surface potentials between –2V and 2V (vs. SHE) are commonly reported at metal–electrolyte

[10]Implemented using LAMMPS `fix electrode/conp` with with aglo to account for moving topwall

interfaces, particularly for gold and carbon electrodes operating in $KHCO_3$ or KCl-based electrolytes. Within this voltage range, multiple elementary steps such as CO_2 activation, *CO formation, and proton–electron transfer are known to occur with appreciable reaction rates.[41][51]

Similarly, electrowetting studies show that potentials in the ±2V range can induce strong changes in contact angle and interfacial charge structure[32]. Each case was initialized from the same 8ns equilibrated and mechanically relaxed structure. The Constant Potential Method (CPM) was applied only to the catalyst atoms of the walls, while the hydrophobic additive regions remained electrically neutral.

Run Conditions All simulations used:

- 1fs timestep,
- NVT ensemble,
- Rigid constraint applied to water molecules,
- Bicarbonate ions constrained to preserve geometry,
- Output recorded every 1ps for analysis.[11]

A total simulation length of 20ns was chosen for each voltage case.

Simulation Conditions and System States To dissect the interplay between surface chemistry, electrode polarization, and applied voltage, we simulated four distinct electrochemical conditions, each designed to isolate specific physical phenomena relevant to solute distribution.

- **Case 1 – No CPM (Neutral Walls):**
  In this case, no surface charges or boundary constraints are applied. This configuration serves as a reference for purely chemically driven wetting behavior, free from electrostatic effects.
- **Case 2 – CPM @ 0 V:**
  In this case, the Constant-Potential Method is activated, allowing wall atoms in the hydrophilic regions to adjust their charges dynamically in response to the local electrolyte environment. However, the target potential is set to 0 V, so there is no net field across the system. This setup captures metallic screening and image-charge effects typical of conducting electrodes. This setup also serves as a controlled reference for comparison with the fixed-charge case, thereby highlighting the role of charge regulation in interfacial electrostatics.
- **Case 3 – CPM @ 1 V:**
  A symmetric voltage bias is applied across the walls, setting the top and bottom hydrophilic regions to +1 V and –1 V, respectively. This introduces a moderate electric field across the slit-pore, promoting electrowetting, ion redistribution, and fluid reorganization.

[11] Data collection performed using `fix ave/time`, `compute`, and `dump` commands in LAMMPS.

- **Case 4 – CPM @ 2 V:**
  The applied potential is increased to ±2 V to assess how stronger electrostatic fields intensify interfacial restructuring, double-layer formation, and possible disruption or enhancement of CO_2 adsorption.

In all CPM-enabled cases (2–4), only the hydrophilic zones of the wall were assigned dynamic surface potential via CPM; the hydrophobic regions remained uncharged and electrostatically inert.This mimics a pore in the catalyst layer (CL) of a gas diffusion electrode (GDE), where one side is sprayed with catalyst nanoparticles and the other is coated with a hydrophobic additive such as PTFE on a carbon-based support.

In the Results section, these four cases are compared systematically within each type of analysis.

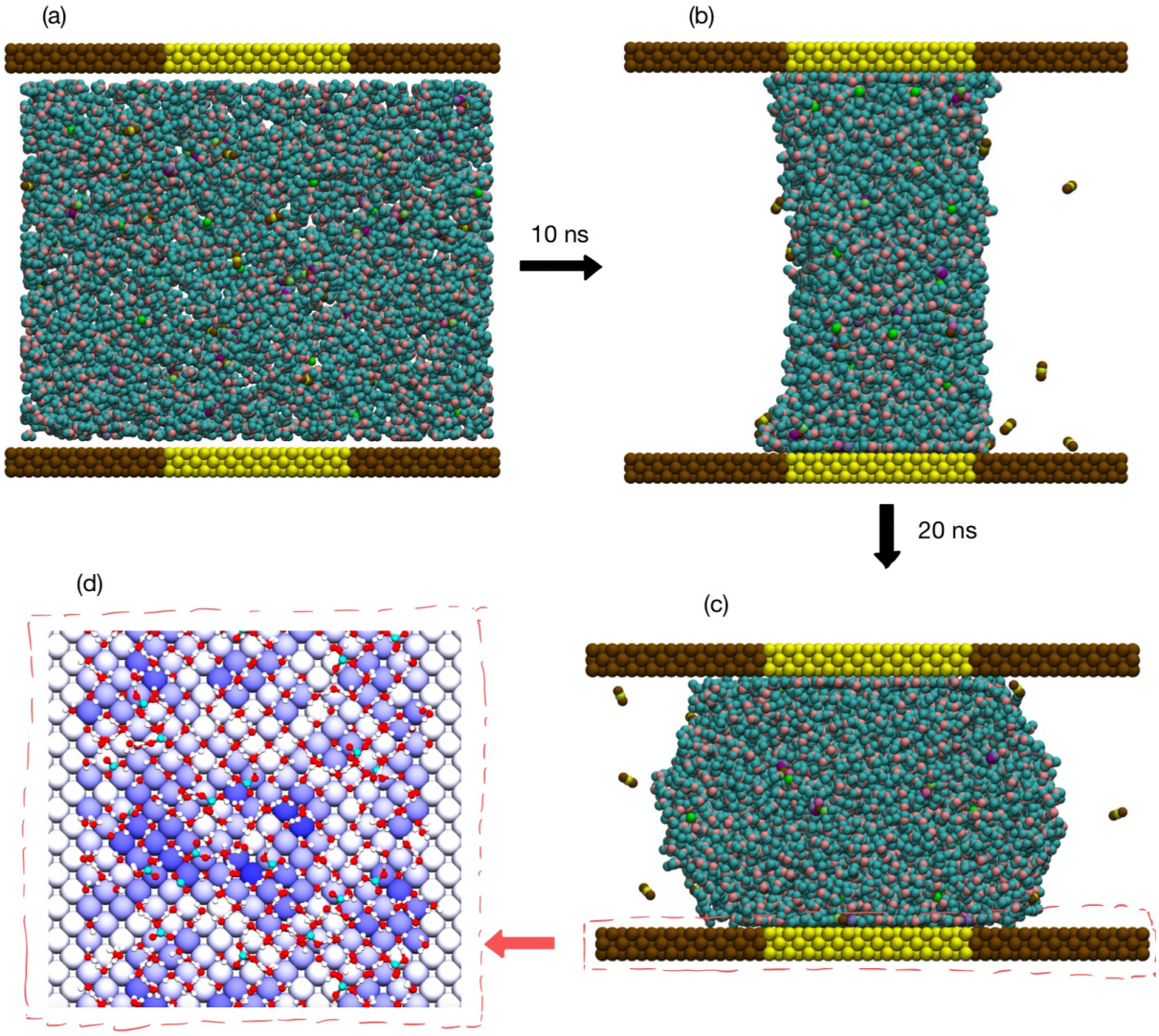

Figure 31: Simulation workflow from initial setup to production run under applied voltage. (a) Initial packed configuration from Packmol. (b) Post-equilibration snapshot showing water drawn to the hydrophilic region. (c) Mechanically relaxed system after top wall is allowed to move, establishing equilibrium height. (d) Bottom plate at 2V showing charge distribution computed via CPM.

5 Results and Discussion

This chapter presents the results of molecular dynamics (MD) simulations performed to investigate the influence of surface chemistry and electrostatic potential on interface structure in a confined nanopore. A particular focus is placed on understanding how voltage-controlled electrowetting modulates spatial distribution, molecular orientation, and CO_2 uptake under varying electrochemical boundary conditions.

The results are presented in the following order:

- Section 5.1 presents one-dimensional number density profiles for each species, showing how confinement and wall electrostatics influence fluid layering.
- Section 5.2 introduces two-dimensional lateral density maps, revealing in-plane heterogeneity linked to surface patterning and voltage-induced wetting transitions.

Rather than isolating voltage effects in a separate final section, the influence of surface potential is discussed progressively within each subsection. This structure allows each type of analysis, density, orientation, adsorption, to be understood both in isolation and in the context of electrostatic modulation. Also, The anode (top wall) was allowed to move along the z-direction to maintain mechanical equilibrium, whereas the cathode (bottom wall) was fixed. Since our focus is on the cathode-side interfacial behavior, anode-side concentrations were not analyzed in detail.

5.1 One-Dimensional Density Profiles

To quantify the spatial distribution of species along the confinement direction, one-dimensional (1D) number density profiles were calculated along the z-axis, perpendicular to the gold walls. These profiles provide molecular-scale insights into fluid structuring near interfaces, including layering phenomena, ion adsorption, and field-induced rearrangements under applied surface potentials.

Beyond their intrinsic utility in describing confined interfacial systems, 1D profiles also serve as a critical point of comparison with continuum electrostatic models, such as the Poisson–Boltzmann (PB) and generalized modified Poisson–Nernst–Planck (GMPNP) frameworks. Aligning MD-derived profiles with this convention enables a direct evaluation of non-continuum effects, such as ion layering, finite-size exclusion, and molecular correlations.

For post-processing analysis to obtain these profiles, the simulation box was divided into evenly spaced slabs (a process known as *binning*) of thickness $\Delta z = 0.25$ Å, parallel to the xy-plane. For each slab, the total mass of a given species was averaged over the trajectory and normalized by the slab volume to obtain a mass density profile $\rho_m(z)$ in units of $\mathrm{g\,cm^{-3}}$. This was then converted to molar concentration $C(z)$ (in $\mathrm{mol\,L^{-1}}$) using the molecular weight M of the species. :

$$C(z) = \frac{1000 \cdot \rho_m(z)}{M} \tag{2}$$

where:

- $C(z)$ is the molar concentration at height z ($\mathrm{mol\,L^{-1}}$),
- $\rho_m(z)$ is the mass density in $\mathrm{g\,cm^{-3}}$,

- M is the molar mass in $\mathrm{g\,mol^{-1}}$,
- The factor of 1000 converts $\mathrm{cm^3}$ to liters.

This procedure was repeated independently for CO_2, K^+, and HCO_3^-, using the center of mass of each molecule or ion as the positional reference to avoid overcounting multi-atom species. For example, CO_2 distributions reflect the position of the molecular centroid rather than individual atoms. The computed $C(z)$ profiles represent time-averaged concentrations over the final 10 ns of each 20 ns production simulation, ensuring equilibrium sampling and statistical reliability.

Let the slab index be denoted by i and its volume by:

$$V_i = L_x \cdot L_y \cdot \Delta z \tag{3}$$

where L_x and L_y are the box dimensions in the lateral directions. If m_i is the total mass of the selected atoms/molecules in slab i, then the mass density and molar concentration are given by:

$$\rho_m(z_i) = \frac{m_i}{V_i} \quad \Rightarrow \quad C(z_i) = \frac{1000 \cdot m_i}{M \cdot L_x L_y \Delta z} \tag{4}$$

This treatment accounts for the full cross-sectional area of the simulation box, ensuring proper normalization across all cases.

The coordinate system was centered about the pore midplane ($z = 0$ Å), and profiles were symmetrized when appropriate to reveal average layering features. These profiles serve as the primary diagnostic for comparing the structural response of confined fluid species across the four electrostatic boundary conditions. In subsequent subsections, these profiles are analyzed species by species, and results are compared across the simulation cases to reveal how electrode polarization and field strength alter interfacial structure.

5.1.1 Molecular Dynamics Profiles

Figure 35, 36 and 37 presents one-dimensional concentration profiles for CO_2, K^+, and HCO_3^- respectively, across the pore height (z-axis) for four simulation conditions: fixed neutral walls (No CPM), and constant-potential simulations at 0 V, 1 V, and 2 V. Each curve represents the average concentration across x and y, from cathode to anode.

Water and Charge Distribution Figure 32 shows the atomic concentrations of H and O from water molecules near the negative electrode under a 2 V potential, focusing only on the type 11 (hydrophilic) region of the surface. In the SPC/E water model, the hydrogen and oxygen atoms carry partial charges of $+0.4238\,e$ and $-0.8476\,e$, respectively, and thus interact electrostatically with the electrode in addition to van der Waals forces. The negatively charged surface attracts H and repels O atoms, forcing water molecules to rotate such that the hydrogens predominantly point toward the wall. This is seen in the primary H peak located about 0.5 Å from the cathode surface, which is nearly devoid of O atoms. The first O peak appears roughly 1.8 Å from the surface, followed by a second H peak, consistent with a tilted water orientation. The height difference and spatial offset between these peaks show that H atoms dominate the innermost interfacial layer, while O remains slightly farther away. Additional H and O peaks extend up to 9–11 Åfrom the surface, forming a damped oscillatory pattern, though not a simple harmonic one. These layers reflect a combination of hydration shell structure, molecular packing, and the voltage-induced orientation of interfacial water.

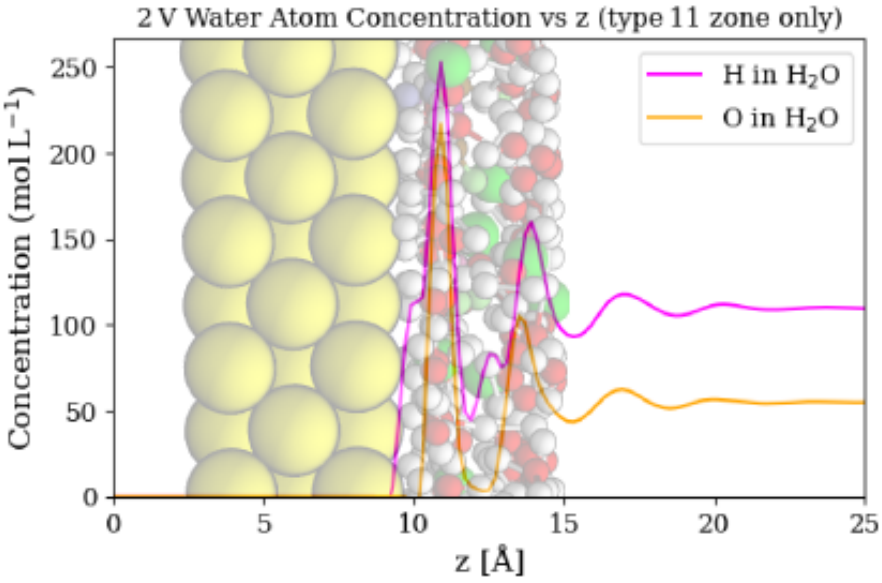

Figure 32: Water atom concentration profiles near the negatively charged wall at 2 V. The z-distribution of H and O atoms in H_2O shows that hydrogen atoms preferentially orient toward the wall, indicating interfacial dipole alignment. Background rendering highlights the surface structure (yellow) and water orientation (white: H, red: O) and is provided for visual context only (not to scale)

These orientational trends are further quantified in Figure 33, which shows the distribution of the cosine of the water dipole angle ($\cos\phi$) within 5 Å from the surface. At 2 V, the probability distribution broadens and shifts toward more negative values of $\cos\phi$ (≈ -1 to -0.5), indicating a larger fraction of water molecules with their dipoles oriented into the wall—i.e., hydrogens facing the negatively charged surface. All cases show a pronounced peak near $\cos\phi \approx 0$, corresponding to dipoles lying roughly parallel to the wall, but the 2 V case exhibits a noticeable increase in probability density at strongly negative $\cos\phi$ values. This voltage-dependent reorientation lowers the effective dielectric constant of interfacial water in the surface-normal direction, amplifying local fields and altering ionic screening near the electrode.

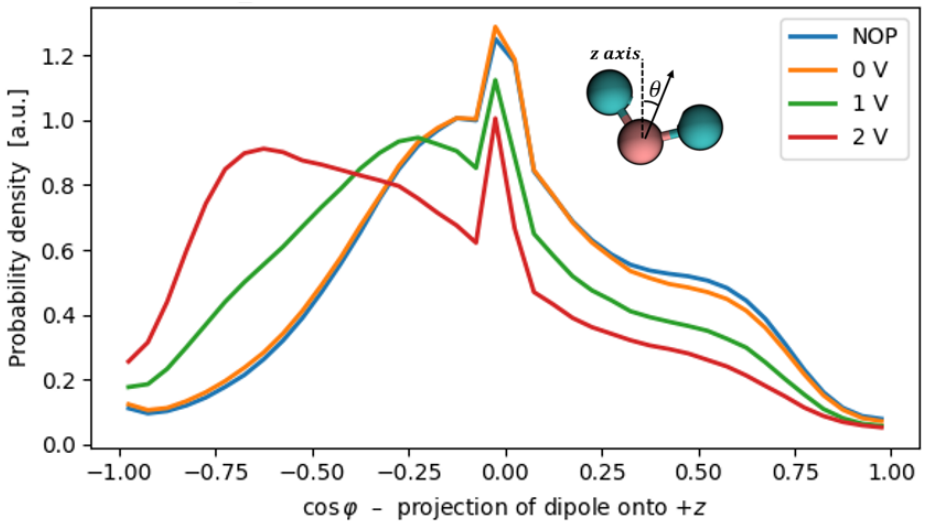

Figure 33: Distribution of $\cos\theta$ for water dipole moments in the interfacial region adjacent to the cathode

Figure 34 shows the total charge density, i.e., the sum of contributions from all charged species (K^+, HCO_3^-, CO_2, and water partial charges), as a function of z near the bottom wall at 2 V. Within the wall itself, most of the induced surface charge appears localized near the outermost layer of atoms, consistent with expectations from the Constant-Potential Method (CPM) and classical electrostatics: charge accumulates at the interface to minimize energy, analogous to how free charges in a conductor rearrange to screen the interior from an external electric field.

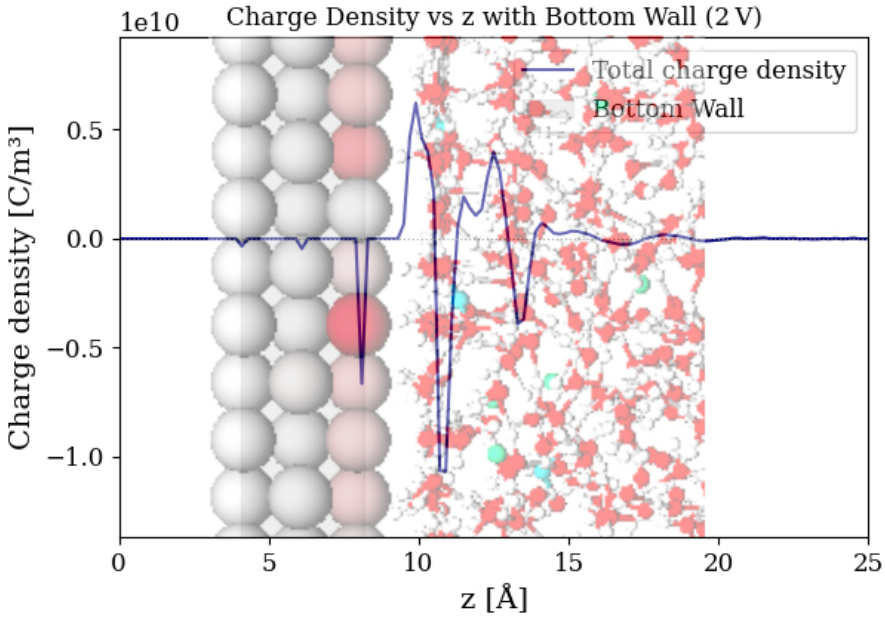

Figure 34: Charge density profile near the bottom wall at -2V, with an overlay of the gold surface and nearby fluid molecules. Most of the induced charge is concentrated at the outer surface layer of the CPM-applied gold plate.

Immediately outside the wall (z 1–2 Å from surface), a sharp positive spike is visible in the fluid phase due to cations (primarily K^+ and H-atoms from water) accumulating

near the surface. This is followed by a stronger negative peak, corresponding to the first oxygen-rich hydration layer, reinforced by HCO_3^- counterions. The charge then oscillates with alternating sign, forming a layered structure that damps out beyond 7 Å from the surface, where the fluid becomes electrostatically neutral on average. These oscillations reflect the interplay of ion adsorption, water dipole orientation, and excluded volume effects, none of which are captured in mean-field continuum models. The spatial structure and decay of this profile illustrate the resolution of the electric double layer in MD, including both molecular and ionic contributions near the polarized surface.
Next, the molecular distribution trends are examined, as shown in Figures 35, 36, and 37.

K^+ Ions: In the absence of surface potential, K^+ ions exhibit weak, symmetric layering near both walls, as shown in Figure 36, rising from the bulk value of 0.25 M to approximately 0.9 M in the EDL. Upon voltage application, K^+ accumulates sharply near the negatively charged wall. At -2 V cathodic potential, interfacial concentrations exceed 4.5 M, forming a narrow first peak (inner Helmholtz layer) and a broader outer peak 3 Å farther from the surface. The anode wall shows K^+ depletion to 0.1 M, as expected from electrostatic exclusion. These layered structures confirm formation of a compact double layer, modulated by voltage and ion hydration.

HCO_3^- Ions: For HCO_3^-, the concentration decreases from 0.25 M in bulk to nearly zero at the cathode surface (Fig 37). However, HCO_3^- consistently accumulates within 3–4 Å of the cathode wall across all conditions, and this is also observed under applied bias of 1 V and 2 V The near-surface concentration increases significantly, reaching approximately 2.3 M at 2 V. This accumulation occurs alongside K^+ condensation, suggesting that bicarbonate ions are stabilized by ion–ion correlations or local hydration shell effects. The positively charged wall exhibits only minor HCO_3^- accumulation, contrary to classical expectations. These observations imply that co-ion exclusion is not complete, and that specific interactions dominate over mean-field electrostatics under nanoconfinement.

CO_2: CO_2 shows weak but measurable interfacial enrichment in all cases (Fig 35). In the No-CPM condition, concentrations are overall similar at anode and cathode; while the cathode exhibits a sharp peak ($\sim 0.43\,\mathrm{mol\,L^{-1}}$) and the anode a broader, lower peak ($\sim 0.26\,\mathrm{mol\,L^{-1}}$), the integrated area under the anode curve indicates a comparable total CO_2 concentration. Upon enabling CPM at 0 V, the left-side peak increases (to $0.53\,\mathrm{mol\,L^{-1}}$) while the right slightly decreases, indicating that electrode polarizability alone alters interfacial structure. This occurs without any applied bias, likely due to image-charge effects or modified water layering.

At 1 V and 2 V, CO_2 enrichment becomes asymmetric: cathode shows increased accumulation, while the anode remains unchanged or slightly depleted. The bulk concentration remains constant at approximately $0.06\,\mathrm{mol\,L^{-1}}$.

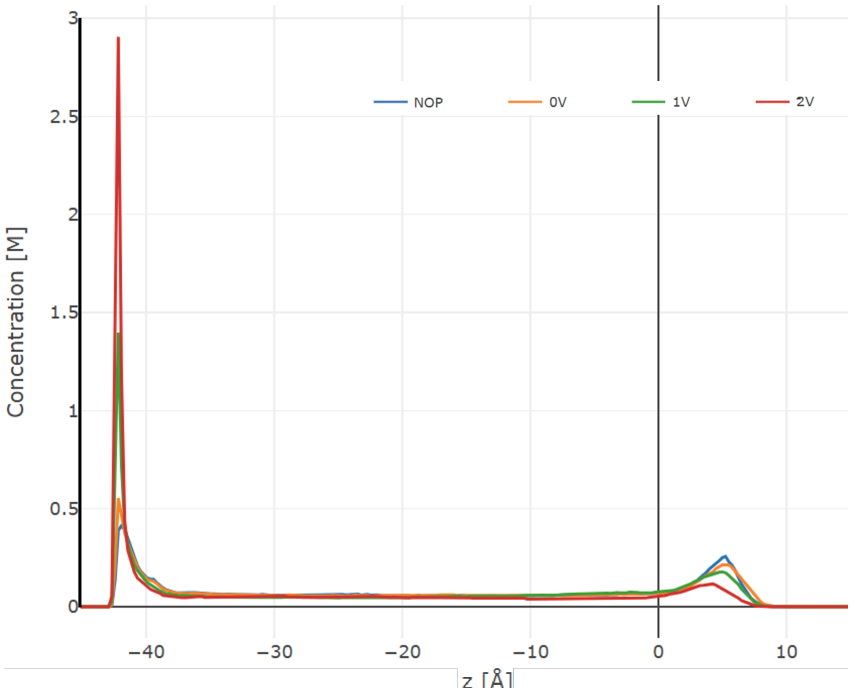

Figure 35: One-dimensional concentration profiles of CO_2 along the z-axis for all four simulation cases. Bold black line represents the cathode surface

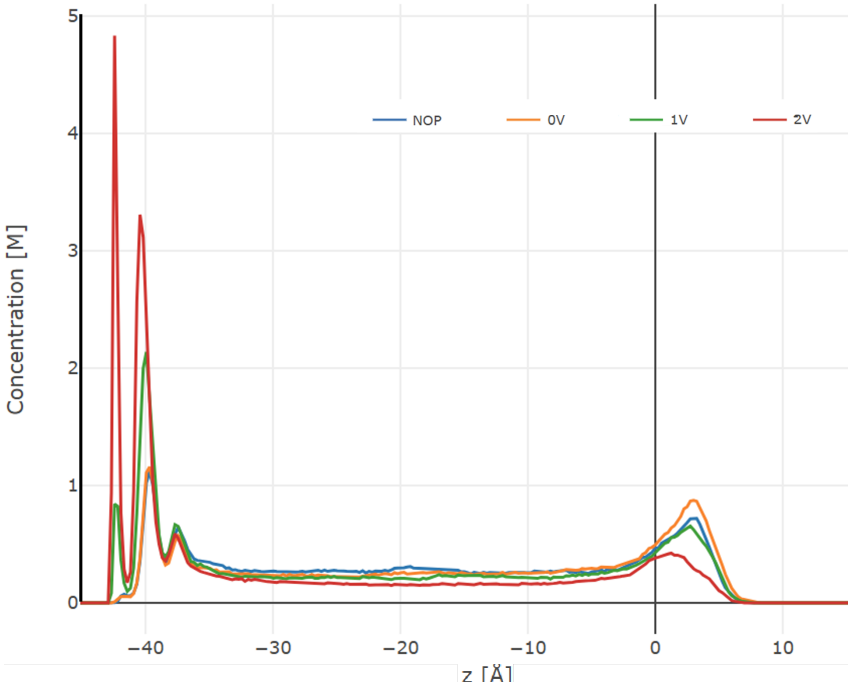

Figure 36: One-dimensional concentration profiles of K^+ along the z-axis for all simulation cases.

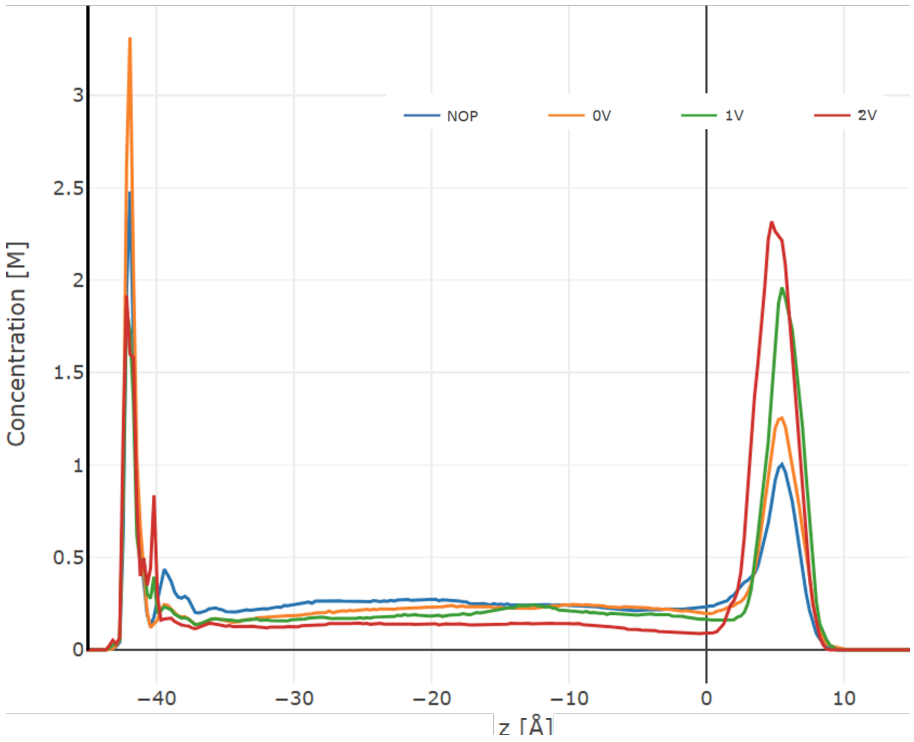

Figure 37: One-dimensional concentration profiles of HCO_3^- along the z-axis for all simulation cases.

5.1.2 Comparison with Continuum Models

To assess the limitations of mean-field electrostatic models in capturing interfacial structure under confinement, MD results from Section 5.1.1 are here compared with continuum model predictions reported by Johnson and Haussener[25]. In their study, ionic and molecular concentration profiles were computed using both Poisson–Nernst–Planck (PNP) and generalized modified PNP (GMPNP) formulations for a 0.25 M $KHCO_3$ solution containing CO_2 at 0.034 M. The GMPNP model includes finite-size effects via steric saturation, while PNP does not. Though their geometry consists of two uniform parallel plates and does not replicate the patterned walls and vacuum interface present in our system, the comparison remains meaningful: it benchmarks the ability of continuum theory to describe ion and solute behavior within the first few nanometers of a charged interface, where deviations from idealized mean-field behavior are most pronounced.

K^+: The continuum models (Figure 38) predict monotonic cation accumulation at the cathode with increasing surface potential, with concentrations rising up to the steric limit in GMPNP ($\sim$5.7 mol L^{-1}) and even beyond physical bounds in PNP (>30 mol L^{-1} for $q = -30\,e^-$)[25]. In contrast, the MD results (Figure 36) show structured layering of K^+, forming a distinct double peak adjacent to the cathode. These correspond to ions in the inner Helmholtz plane (closest to the surface, $\sim$2–3 Å) and a second solvation layer farther out ($\sim$4–5 Å). The peak concentration reaches $\sim$4.8 mol L^{-1} at 2 V, aligning roughly with GMPNP predictions in magnitude, but not in spatial profile.

At 0 V, GMPNP predicts a uniform K^+ concentration equal to the bulk value of 0.25 mol L^{-1}. However, in MD, the K^+ profile already deviates near the walls, with mild layering observed even in the No CPM case. This result underscores the influence of non-

electrostatic interactions, including van der Waals forces, hydration structure, and surface polarization, which are not captured by continuum models. Additionally, CPM-enabled surfaces at 0 V show stronger K^+ accumulation than fixed neutral walls, again indicating that polarizable electrode response affects near-surface ion distributions independently of applied bias.

Overall, while GMPNP approximates the magnitude of interfacial K^+ concentration well, it fails to reproduce the molecular-scale layering, image charge effects, and CPM-specific charge induction observed in MD[25].

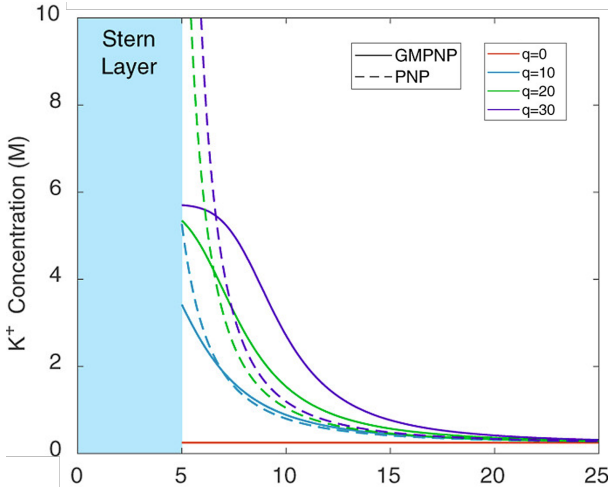

Figure 38: Continuum model predictions for K^+ concentration near a charged surface [25].

HCO_3^-: For bicarbonate, the continuum models (Figure 40) predict gradual exclusion from the vicinity of the negatively charged electrode due to electrostatic repulsion. At $q = -30\,e^-$, both PNP and GMPNP show nearly full depletion of HCO_3^- within ∼5 Å of the wall[25]. In our MD simulations (Figure 37), the expected trend of anion exclusion is partially recovered but not complete: at 2 V, a nonzero HCO_3^- concentration (∼0.6–0.7 mol L^{-1}) persists at the surface, forming a broad peak rather than full depletion.

In all cases, a weak but distinct interfacial accumulation is observed at cathode. These features are absent in continuum predictions. This discrepancy may arise from the molecular geometry of HCO_3^-, whose partial positive charges on H and C atoms can lead to weak surface affinity despite the overall anionic character. This is supported by the atom-resolved concentration profiles (Figure 39), which show that the H atoms peak closer to the surface (∼10 Å) than the O atoms (∼11.3 Å), indicating a tilted orientation where the positive end of the molecule faces the wall. This interfacial alignment may be stabilized by image-charge effects and local water structure, enabling HCO_3^- to remain partially adsorbed even under strong repulsive fields.

Such atomic-level interactions are absent from continuum models, which treat ions as point charges or uniform spheres and assume symmetric exclusion behavior for anions near cathodic surfaces. Therefore, while continuum theory correctly predicts a general trend of co-ion repulsion, it fails to capture the local surface affinity, asymmetry, and incomplete exclusion exhibited in the MD profiles.

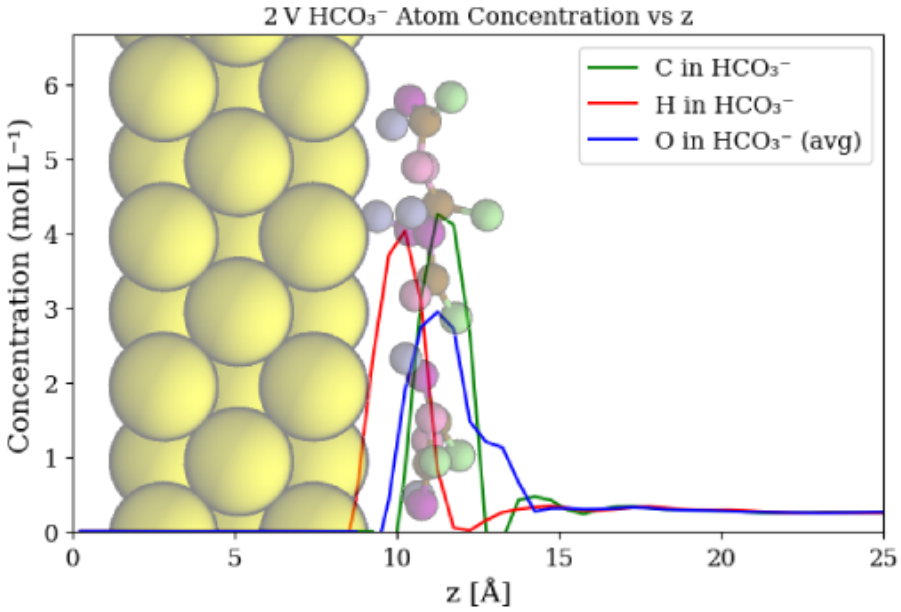

Figure 39: Atom-resolved concentration profiles of HCO_3^- at 2 V, with background showing wall atoms and a representative HCO_3^- molecules (purple: H, brown: C, green: O).

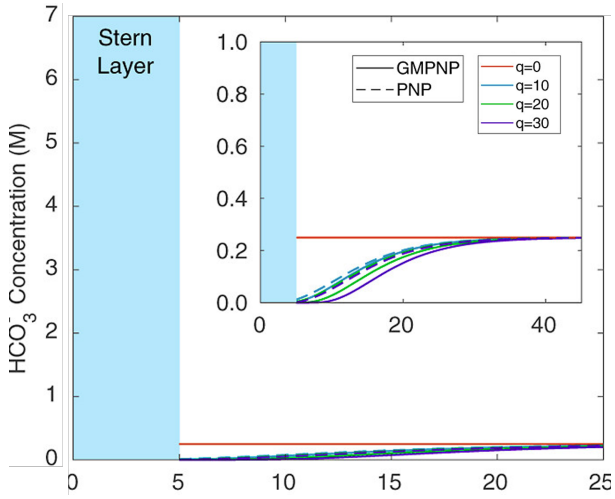

Figure 40: Continuum model predictions for HCO_3^- concentration near a charged surface [25].

CO_2: Continuum models (Figure 41) provide a minimal prediction for CO_2: PNP yields a flat profile equal to the bulk concentration (in the absence of consumption), and GMPNP shows only a minor interfacial dip due to steric exclusion. These models include steric effects and account for crowding near the interface, which leads to a predicted decrease in local CO_2 concentration. However, as seen in the MD results (Figure 40), CO_2 shows clear and repeatable enrichment near the electrode surfaces, particularly under nonzero voltage. At 2 V, CO_2 accumulates to ∼2.8 mol L^{-1} at the negatively charged surface, compared to its bulk value of ∼0.06 mol L^{-1}.

Notably, even in the No CPM and 0 V cases, CO_2 shows mild enrichment (∼0.4–0.5 mol L^{-1}) near both walls. Upon activating CPM at 0 V, the left-wall CO_2 peak becomes sharper and larger. This arises because weakly adsorbed anions coexist with

strongly adsorbed cations, leading the polarizable wall to acquire a slight net negative charge for electrostatic compensation. This localized negative surface potential increases CO_2 affinity, producing preferential adsorption at that wall. This behavior is entirely absent in continuum models, which cannot (accurately) account for van der Waals interactions, electrode-induced polarization. While continuum models predict reduced CO_2 concentration at the surface due to steric crowding, the MD results clearly demonstrate that molecular-scale interactions between CO_2 and the surface persist and dominate, leading to net enrichment instead.

Apart from the continuum comparison, we also benchmark against the fully flooded slit-pore MD results of Johnson & Haussener [25], where CO_2 shows a persistent near-wall enrichment that is largely insensitive to cathodic bias across the reported range (Figure 42). In contrast, in our TPB-resolved setup the interfacial CO_2 population does track the applied bias, with enrichment increasing as the cathode is driven more negative (Figure 35). This contrast highlights that while flooding does not severely hinder CO_2 adsorption at the wall, introducing surface heterogeneity and partial wetting, as in our hydrophobic-additive nanopore, can couple electrostatic effects to local CO_2 partitioning, producing a pronounced voltage-dependent response absent in uniformly wet systems. Practically, a fully wetted slit retains CO_2 at the wall but shows weak potential sensitivity, whereas a TPB-rich environment enables bias-tunable CO_2 adsorption.

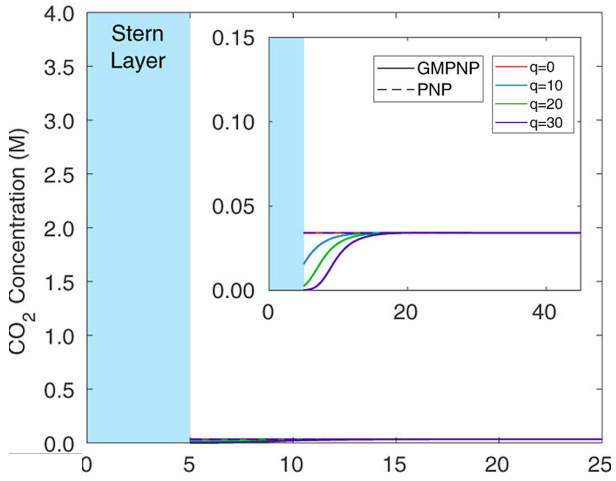

Figure 41: Continuum model predictions for CO_2 concentration near a charged surface [25].

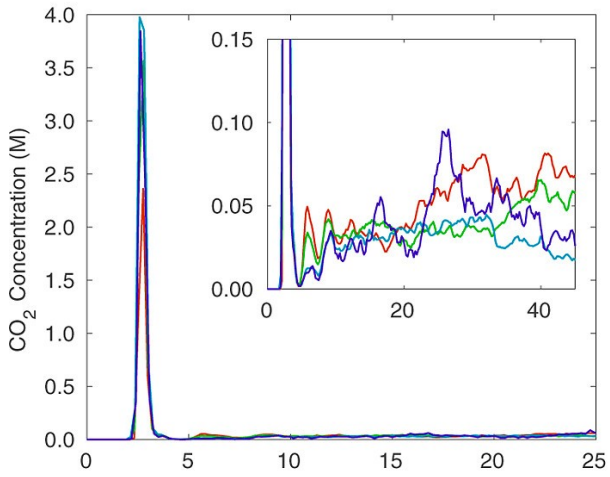

Figure 42: Molecular dynamics results from Johnson & Haussener [25] for a fully flooded slit-pore, showing CO_2 concentration profiles at varying applied potentials

5.2 Two-Dimensional Density Profiles

While one-dimensional concentration profiles provide averaged insight along the confinement axis (z), they inherently obscure lateral variations that arise due to surface patterning, molecular adsorption, and field-driven inhomogeneities. To resolve these effects, we analyze two-dimensional spatial density maps in the x–z plane for selected species. These distributions capture structural features such as localized adsorption at hydrophilic zones, in-plane asymmetries in ion packing, and spatial correlation between surface topography and interfacial accumulation. Furthermore, high-density features in these maps often correspond to trapping in hollow sites on surface, sub-surface adlayer pockets, or localized field minima: phenomena that cannot be resolved in 1-D binning.

The following sections present 2D number density maps for K^+, HCO_3^-, and CO_2, across different voltage conditions. When relevant, atomic overlays and zoomed-in system snapshots are used to clarify molecular-scale adsorption behavior and connect charge density features to underlying surface structure.

5.2.1 Construction of Two-Dimensional Concentration Maps

To analyze spatial heterogeneity in solute distributions near the electrode surfaces, two-dimensional concentration maps were computed in the x–z plane for selected atomic species. This approach enables resolution of both normal (z-direction) structuring due to interfacial electrostatics and lateral (x-direction) inhomogeneities induced by surface heterogeneity, such as triple-phase boundaries (TPBs).

The simulation box was first partitioned into a regular grid of rectangular voxels of dimensions $\Delta x = \Delta z = 0.25$Å. For each trajectory frame, the positions of the molecules were recorded and spatially binned based on their x and z coordinates, with the origin shifted to the box center. The total count of particles $N_{i,j}$ in each bin (i, j) was accumulated over all trajectory frames and converted to a number density using:

$$\rho_{i,j}^{num} = \frac{N_{i,j}}{V_{voxel} \cdot N_{frames}} \tag{5}$$

where $V_{voxel} = \Delta x \cdot \Delta z \cdot L_y$ is the volume of each x–z slab (assuming the full box

height L_y is integrated out), and N_{frames} is the number of analyzed frames. This number density was then converted to molar concentration (mol/L) using Avogadro's number N_A as:

$$C_{i,j} = \rho_{i,j}^{num} \cdot \frac{10^{30}}{N_A.1000} \tag{6}$$

where the factor 10^{30} converts Å^{-3} to m^{-3}.

This voxel-based mapping procedure yields 2D concentration fields $C(x, z)$, which were rendered as color heatmaps to visualize lateral patchiness, layering near the wall, and field-induced spatial confinement. Importantly, these maps enable detection of phenomena that are otherwise averaged out in conventional 1D z-profiles, such as the emergence of ion adsorption corridors aligned with specific surface types or lattice features, the influence of TPBs, and spatial correlations between co- and counter-ions. This framework is applied in the subsequent sections to analyze the spatial distributions of K^+, CO_2, and HCO_3^-.

5.2.2 Two-Dimensional K^+ Analysis

Figure 43 presents the two-dimensional K^+ concentration (molarity) in the x–z plane for four simulation cases: No applied potential (NOP), 0 V, 1 V, and 2 V. Each color map spans the full gap between the parallel electrodes (approximately $z = -45$ Å at the bottom gold wall up to $z = +10$ Å at the top wall) and covers $x = -57.1$ to $+57.1$ Å laterally. The anode in these simulations is free to move along z to maintain mechanical equilibrium, but since our focus is on the cathode-side (bottom wall) behavior, the anode concentrations are not analyzed in detail. The K^+ density is depicted on a uniform color scale capped at 3 $\text{mol}\,\text{L}^{-1}$, such that yellow color indicate higher local ion concentrations. The cathode is located just outside the plotted z-range, immediately beneath the prominent K^+ accumulation layers at the solid–liquid interfaces. Notably, the Au(100) lattice constant is 4.0788 Å, which will serve as a reference length for interpreting any periodic lateral features in the ion density. The central region of each electrode (approximately $x = -20$ to $+20$ Å) corresponds to a hydrophilic surface zone (surface type 11), while the outer portions ($|x| > 20$ Å) are hydrophobic. This patterned wettability leads to spatial variations in interfacial water structure and, consequently, in the local ion distribution, as discussed below.

No-bias baseline (NOP and 0 V). Under no applied field, the K^+ distribution is essentially uniform and symmetric. In the absence of an external potential (NOP, Fig. 43a), there is no driving force to push cations toward either wall. The 2D map shows K^+ fairly evenly dispersed throughout the interior, with only very mild enhancements in concentration near the bottom surface. These interfacial features are broad, diffuse layers on the order of a few angstroms thick, arising from the spontaneous ordering of solvent and ions next to a neutral confining surface. The peak K^+ concentrations at the bottom in NOP are low (on the order of ∼0.5–1.0 M), indicating only a minor accumulation due to exclusion from the wall and coordination with surface-bound water. Laterally, under zero bias, there is discernible variation: while in z direction there is no significant difference between the NOP and 0 V cases, the lateral K^+ distribution clearly distinguishes the two configurations. In the NOP case, the hydrophilic central zone shows more K^+ accumulation near the edges between hydrophobic and hydrophilic regions on the bottom electrode. In contrast, this effect is not observed in the 0 V case(Fig. 43b),

where K^+ density is relatively higher at the center of the hydrophilic zone. This behavior is discussed in more detail in section 5.2.5.

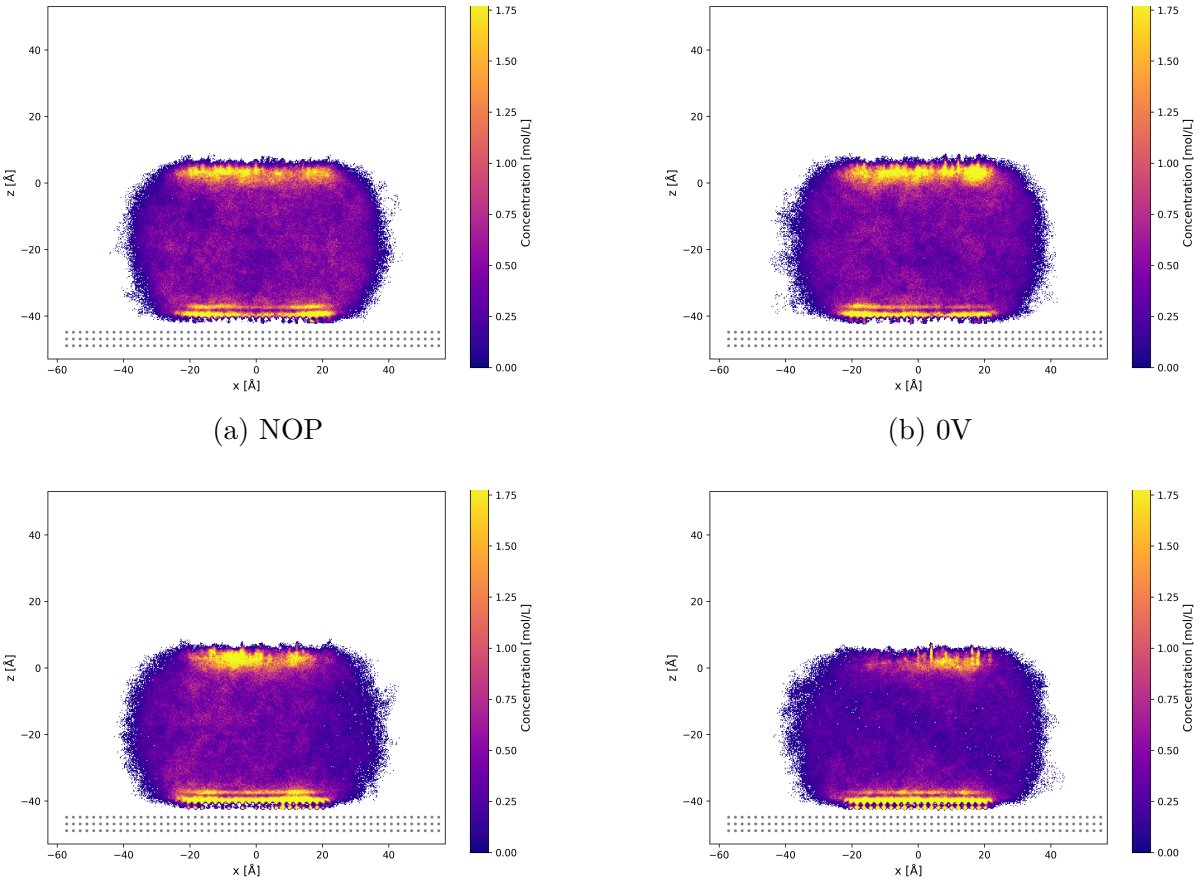

(a) NOP (b) 0V

(c) 1V (d) 2V

Figure 43: Two-dimensional K^+ concentration maps ($\mathrm{mol\,L^{-1}}$) for four potential conditions (NOP, 0 V, 1 V, 2 V), plotted across the x–z plane.

Effect of a 1 V potential. Imposing a 1 V potential difference breaks the symmetry of the K^+ distribution and drives significant ion adsorption at the negative electrode. In the 1 V case (Fig. 43c), K^+ enrichment becomes clearly visible near the bottom wall and a depletion is noted near the top wall. A pronounced K^+ density peak emerges at the bottom interface, centered around $z \approx -40$ Å, just a few angstroms above the gold surface. The local K^+ concentration in this region reaches a few molar, and closer to the plate exhibits clear local inhomogeneities rather than a uniform distribution.

It is at 1 V that lateral heterogeneities tied to surface chemistry and lattice structure begin to manifest. In the bottom region of Fig. 43c, the K^+ enrichment is not perfectly uniform along x; instead, the central hydrophilic band (approximately $x = -20$ to $+20$ Å) shows slightly higher K^+ density right at the interface compared to the hydrophilic outer regions. This lateral contrast reflects favorable coordination of hydrated K^+ ions with the structured water network in the central hydrophilic patch. The K^+ layer at this stage remains mostly continuous but exhibits small modulations—hinting at the emergence of site-specific adsorption patterns.

High bias (2 V) and emergence of discrete adsorption sites. At 2 V, the K^+ distribution near the bottom electrode becomes sharply structured, revealing localized adsorption into well-defined spots consistent with DFT studies conducted[20]. In Fig. 43d, bright peaks appear periodically across x within $z \approx -41$ Å, with spacings matching the Au(100) lattice constant of 4.0788 Å. These are site-specific adsorption events, indicating that K^+ ions preferentially occupy energetically favorable positions such as hollow sites or minima in the electrostatic potential energy landscape created by the electrode.

A VMD snapshot of the 2 V system (Figure 44) confirms the presence of K^+ ions trapped in sub-adlayer pockets, sitting just beneath the first interfacial water layer and in registry with the metal lattice. This sub-adlayer localization requires partial dehydration, suggesting strong cation–metal interaction driven by high field strengths.

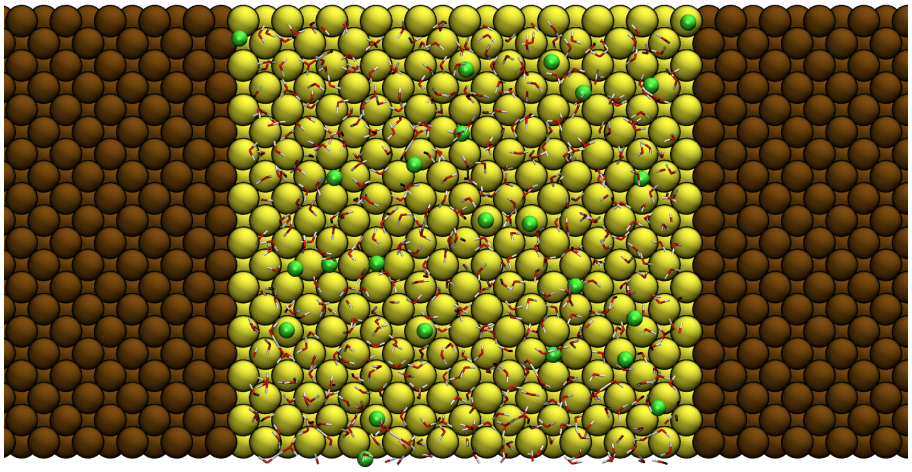

(a) A K^+ ion adsorbed onto the Au(100) surface, positioned in a surface lattice site. The ion appears partially dehydrated, reflecting strong ion–metal interaction under high field conditions.

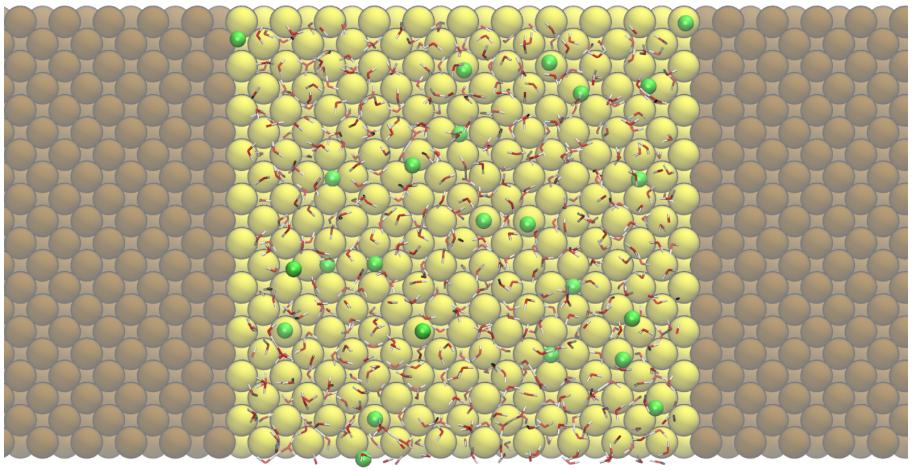

(b) Solvation layering around adsorbed K^+: a compact first hydration shell is followed by a more diffuse second layer.

Figure 44: Representative VMD snapshots from the 2 V simulation showing (a) site-specific adsorption of K^+ onto the Au(100) electrode and (b) the resulting layered hydration structure.

Layering, hydration state, and EDL stratification. K^+ concentration perpendicular to the cathode shows two distinct layers. The first peak around $z \approx -41$ Å (Fig 36) corresponds to ions directly adsorbed onto the Au(100) lattice and appears partially dehydrated. The second accumulation zone is located near $z \approx -36$ Å, positioned between the first and second hydration layers of interfacial water (see black box in fig45a). This second population is clearly visible in the 2D concentration maps and water profiles, especially at 2 V (see Fig. 45). It is not directly adsorbed to the surface but also not fully hydrated, suggesting that the ions are stabilized between hydration shells. As the voltage increases, this layering becomes more pronounced and slightly compressed, consistent with stronger electric-field-driven structuring.

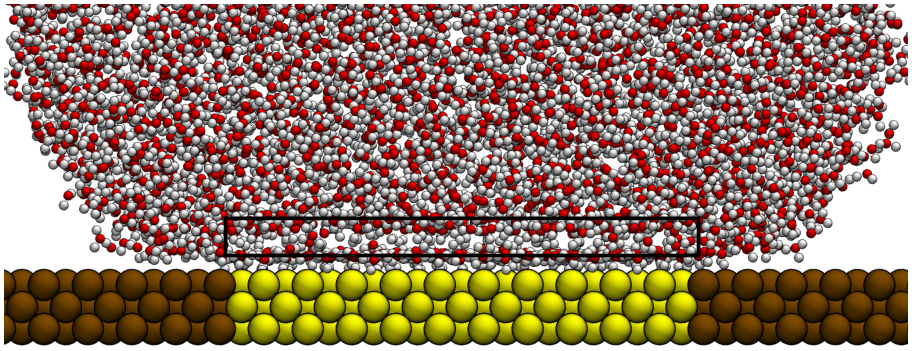

(a) Annotated hydration layering around the bottom Au(100) plate, showing a black box indicating the region between the first and second hydration layers.

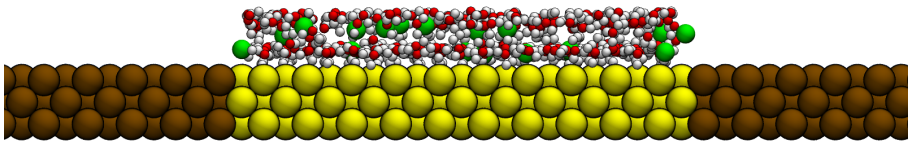

(b) Zoom-in of potassium ion distribution at 2V showing accumulation in the boxed region from (a). The second K layer appears confined between hydration layers.

Figure 45: Figures showing intermediate K^+ layering

5.2.3 Two Dimensional HCO_3^- Analysis

Voltage-Dependent Interfacial Exclusion and Peak Intensity Drop. HCO_3^- concentration profiles along the z-direction (Figure 37) show that the position of the primary interfacial peak remains fixed near ∼2-3 Å from the bottom cathode across all voltage conditions (NOP, 0 V, 1 V, 2 V). However, its magnitude decreases steadily with increasing potential, indicating progressive electrostatic exclusion of the anion from the Stern layer. At 2 V, a notable change occurs: a secondary, broader concentration peak appears farther into the solution (∼6 Å). This feature likely arises from a combination of saturation in the first adsorption layer, where increasing surface charge pushes HCO_3^-

ions away from the wall, and electrostatic crowding by accumulated K^+ counter-ions, which reduces available space near the surface. In such regimes, co-ions begin to accumulate in the outer regions of the diffuse layer, consistent with known charge overscreening behaviors in confined systems[18].

Previous MD and DFT studies of interfacial ion distributions have shown that once the inner layer saturates or becomes highly repulsive, additional adsorption shifts outward, resulting in layered ion organization even for co-ions that are typically excluded at low field strength.

Lateral Clustering and Localized Adsorption Corridors. The 2D x–z histograms, shown in Figure 47, demonstrate that HCO_3^- ions form laterally confined patches near the cathode rather than distributing uniformly along the wall. These patches grow sharper and more distinct with increasing voltage. At 2 V, high-density stripes emerge, separated by depletion zones, implying that lateral redistribution is enhanced under strong electrostatic forcing. These high-density bands frequently co-locate with adsorbed K^+ structures, suggesting that bicarbonate adsorption is templated or stabilized by the existing counter-ion landscape and interfacial water structuring.

A conceptually similar phenomenon is reported in the study by Lee *et al.*[46], where ion-specific adsorption patterns and correlated layering were observed at charged mica–electrolyte interfaces. In their work, the use of high-concentration RbI enabled visualization of ion correlations and overscreening, where ions became laterally pinned into well-defined rows along the substrate lattice. These correlated structures persisted even under electrostatic exclusion due to hydration shell compatibility and field localization.

While their system involved crystalline nucleation at very high salt concentrations, and our setup employs dilute $KHCO_3$ with no reactions or ion crystallization, the underlying insight remains relevant: strong interfacial fields and surface patterning can drive ions into specific adsorption zones, overriding uniform distribution expectations. In our system, the lattice periodicity of the Au(100) plate, combined with K^+ adlayer geometry and hydration constraints, likely carves out adsorption corridors where HCO_3^- ions preferentially localize, even under net repulsive conditions.

1D–2D Interplay The 1D z-profiles(Fig 37), averaged over hydrophobic-hydrophilic section, underrepresent the patchiness evident in 2D maps. For example, the mild, broad hump at 2 V in the z-profile corresponds to localized lateral peaks at ∼5–6 Å in 2D slices. This averaging smears spatially sharp features, underscoring the necessity of using 2D views to resolve interfacial heterogeneity.

The x-profiles (Figure 46), extracted near the wall ($z \approx 10$ Å), display periodic peaks that grow sharper with increasing bias. These align with lateral HCO_3^- hotspots and further suggest coupling with the templated structure of K^+.

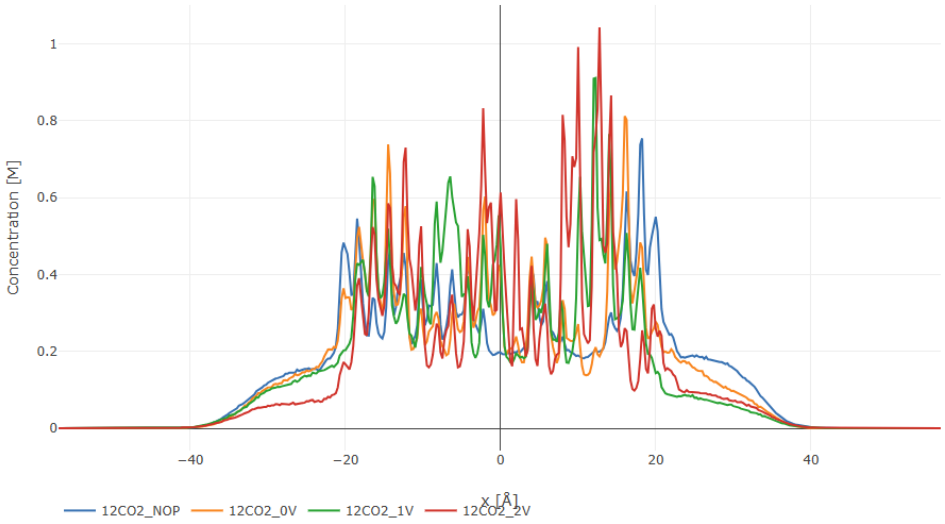

Figure 46: One-dimensional concentration profiles of HCO_3^- along the x-axis for all simulation cases.

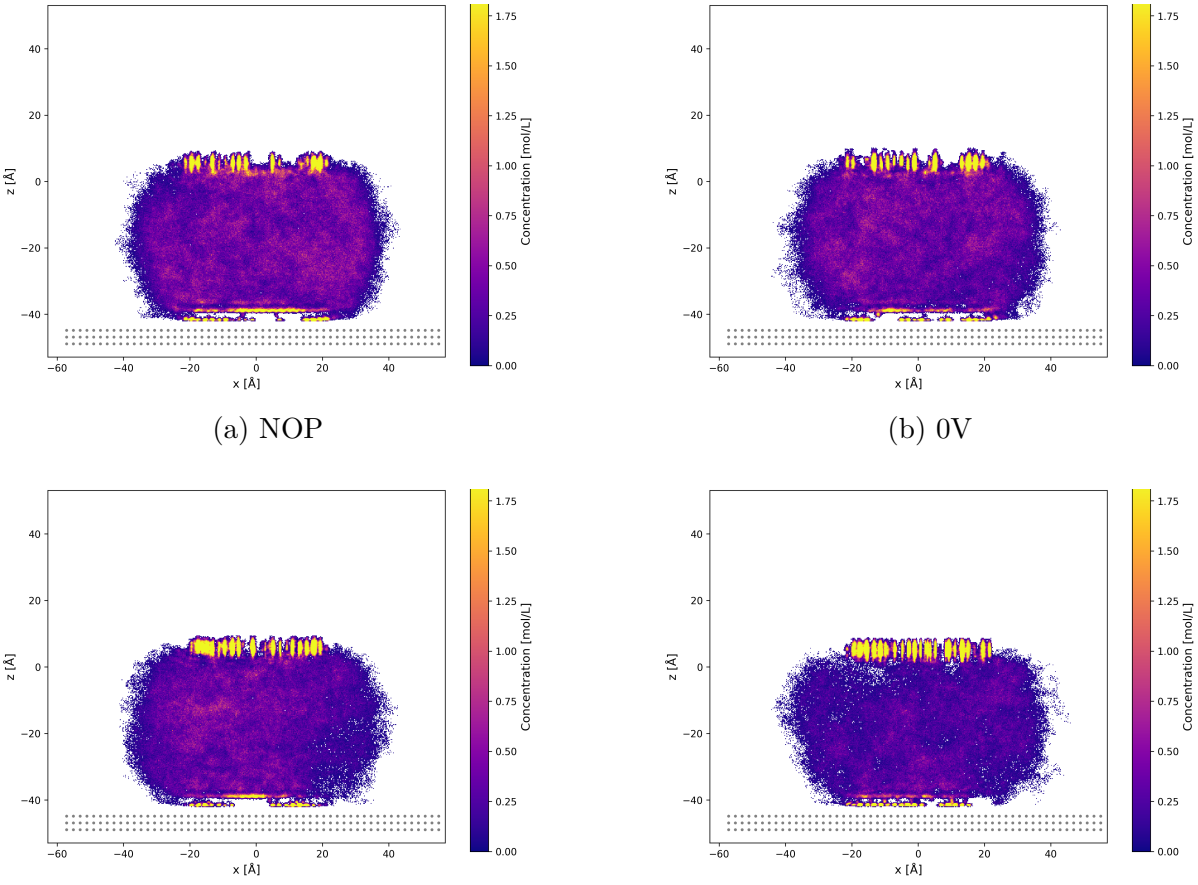

(a) NOP (b) 0V

(c) 1V (d) 2V

Figure 47: Two-dimensional HCO_3^- concentration maps ($\mathrm{mol\,L^{-1}}$) for four potential conditions (NOP, 0 V, 1 V, 2 V), plotted across the x–z plane.

5.2.4 Two Dimensional CO_2 Analysis

Voltage-Dependent Enhancement of CO_2 Interfacial Concentration. From the 1D z-concentration profiles, shown in Figure 35, a clear increase in CO_2 accumulation is observed at the bottom surface ($z \approx -44$ Å) as the applied cathodic bias increases from 0 V to 2 V. The interfacial peak rises from ≈0.5 M under unbiased conditions to nearly 3 M at 2 V. This trend is consistently captured in the 2D xz heatmaps (Figure 49), where the most intense hotspots emerge exclusively at the interface under high bias. The sharpness and intensity of these interfacial lobes demonstrate that field-induced image-charge interactions between the CO_2 and the negatively polarized gold surface significantly lower the local adsorption energy barrier, facilitating physical trapping in the Helmholtz layer.

The spatial patterning of CO_2 becomes more evident when projected onto the xy-plane over the hydrophilic region of the bottom plate. The mass density plots reveal that with increasing bias, CO_2 is not uniformly distributed but instead forms spatially confined patches that align with localized electrostatic features of the substrate. At 0 V, the distribution is relatively sparse and disordered; however, as the bias increases to 1 V and 2 V, the CO_2 regions become denser and increasingly organized into lateral bands and spot-like domains.

Figure 48a–d shows the lateral charge distribution on the bottom plate and the corresponding CO_2 adsorption patterns for four representative cases: NOP, 0 V, 1 V, and 2 V. Notably, the CO_2 density maxima consistently align with localized domains of accumulated negative charge, particularly under high applied bias. This occurs because the interface between the hydrophilic and hydrophobic wall regions promotes charge localization, allowing the system to minimize electrostatic energy; the negatively charged domains at these boundaries then act as preferential adsorption sites for CO_2.

This patchiness correlates strongly with the lateral (xy) average charge maps obtained from constant potential method (CPM) calculations, which show that negative charge accumulates preferentially in discrete domains on the hydrophilic Au surface. These charge-rich regions act as electrostatic traps, promoting local CO_2 accumulation by modulating the potential landscape near the interface. A similar observation was made by Du et al. [12], who reported that in montmorillonite nanopores, CO_2 preferentially clusters around localized charge sites, forming adsorption hotspots. Their study demonstrated that such heterogeneity in surface charge distribution significantly enhances spatial structuring of CO_2 within the pore.

While their system differs in material, medium, and charge origin, the core mechanism remains consistent: interfacial charge inhomogeneity governs lateral CO_2 localization. Nevertheless, the agreement between these two contrasting systems underscores a robust physical principle that nanoscale electrostatic heterogeneity can effectively template CO_2 adsorption behavior.

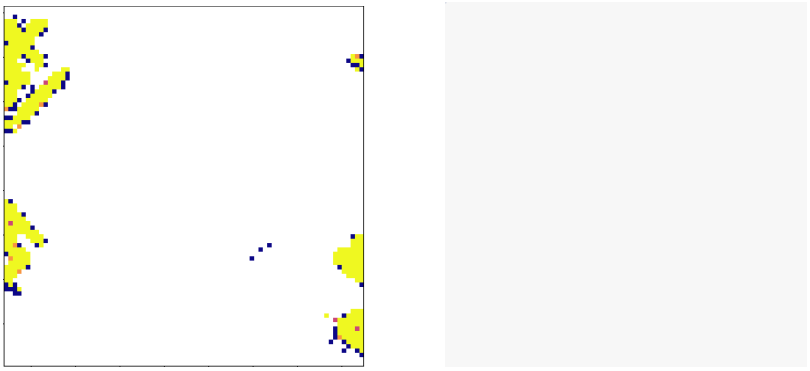

(a) NOP

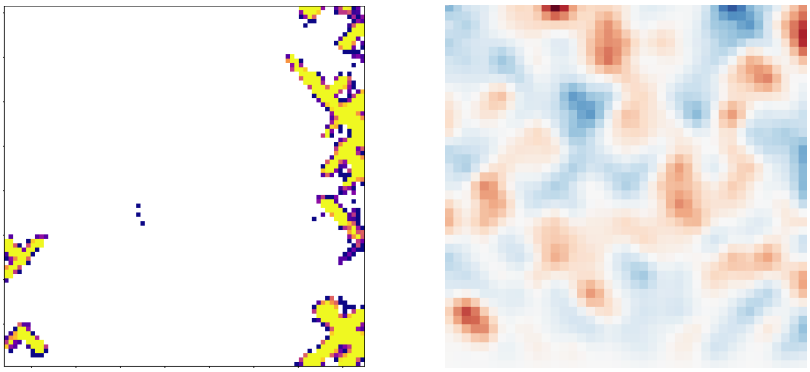

(b) 0 V

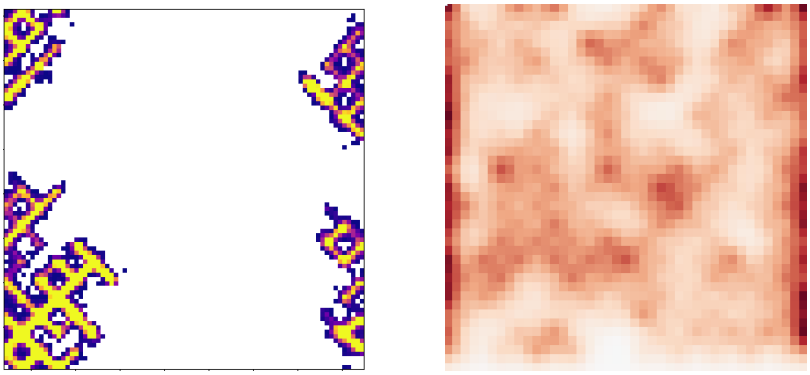

(c) 1 V

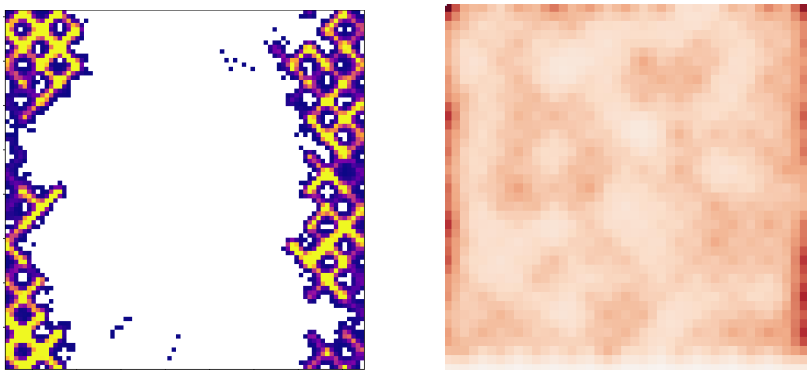

(d) 2 V

Figure 48: CO_2 mass density (left) and lateral charge distribution (right) projected onto the xy-plane of the bottom hydrophilic plate for four electrostatic conditions. Each subfigure (a–d) corresponds to one applied voltage, showing CO_2 accumulation patterns aligning with surface charge heterogeneity.

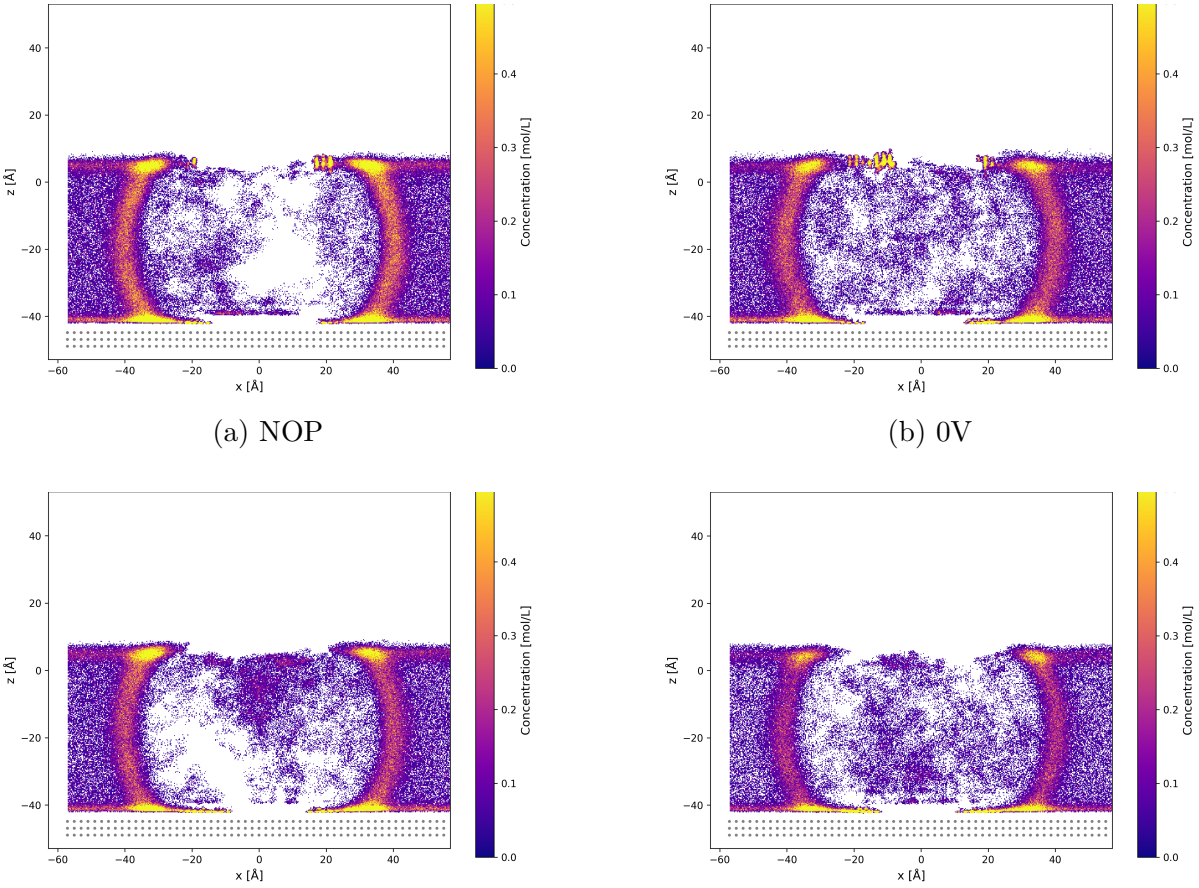

(a) NOP (b) 0V

(c) 1V (d) 2V

Figure 49: Two-dimensional CO_2 concentration maps ($\mathrm{mol\,L^{-1}}$) for four potential conditions (NOP, 0 V, 1 V, 2 V), plotted across the x–z plane.

5.2.5 Two-Dimensional Insights into Double Layer and CO_2 Localization

The one-dimensional z-profiles of potassium number density (Fig 36) initially suggest that the spatial distribution of K^+ ions remains largely unchanged between the no-potential (NOP) and 0 V constant-potential (CPM) cases. In both, the profiles show a primary peak near $z \approx 4$–5 Å above the cathode, followed by a broad decay into the bulk. Based on this averaged view alone, one might conclude that imposing a surface potential via the CPM method has limited impact on the electric double layer (EDL) structure.

However, this interpretation fails under closer scrutiny. The region-resolved density plots, comparing the hydrophilic centre strip (7 Å wide) and the edge regions (average of left and right edges at the hydrophobic/hydrophilic boundary, calculated per bin width $\Delta z = 0.25$ Å), reveal a marked lateral heterogeneity (Figs. 50–53). At NOP, the K^+ profile is dominated by edge accumulation, with the peak at the plate edge rising higher than in the centre. This suggests that, in the absence of surface field relaxation, potassium ions preferentially localize along the lateral confinement zones: regions associated with weaker hydration and lower local water density.

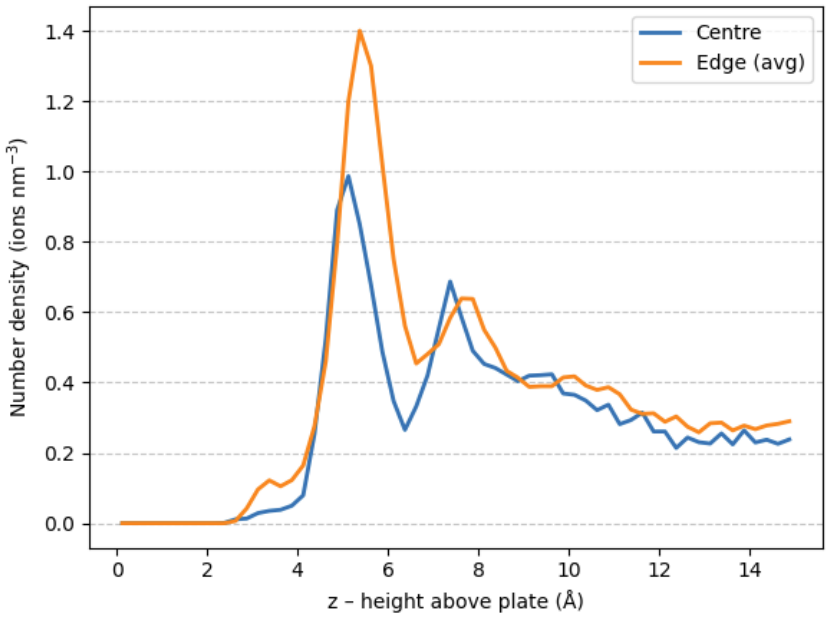

Figure 50: Region-resolved number density of K^+ ions (NOP).

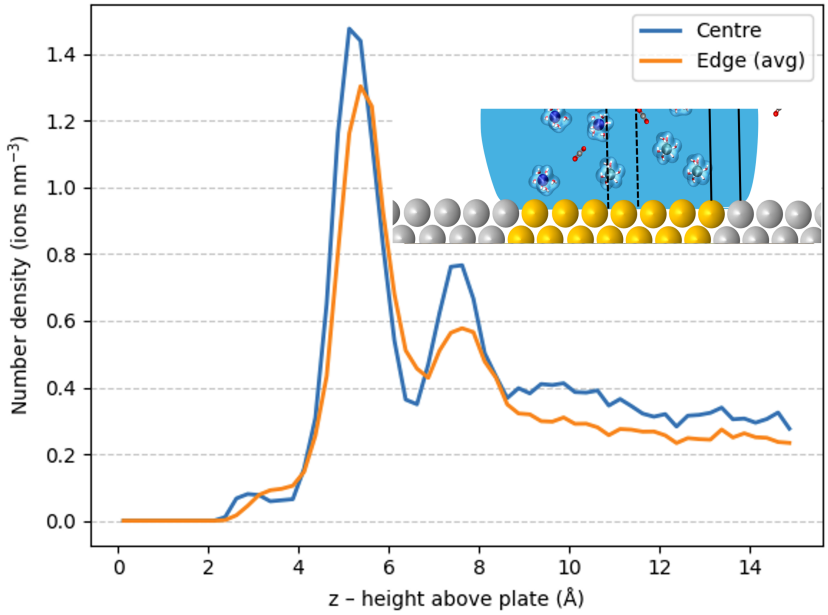

Figure 51: Region-resolved number density of K^+ ions at 0 V. The inset shows the edge and center regions indicated by solid and dotted vertical lines, respectively.

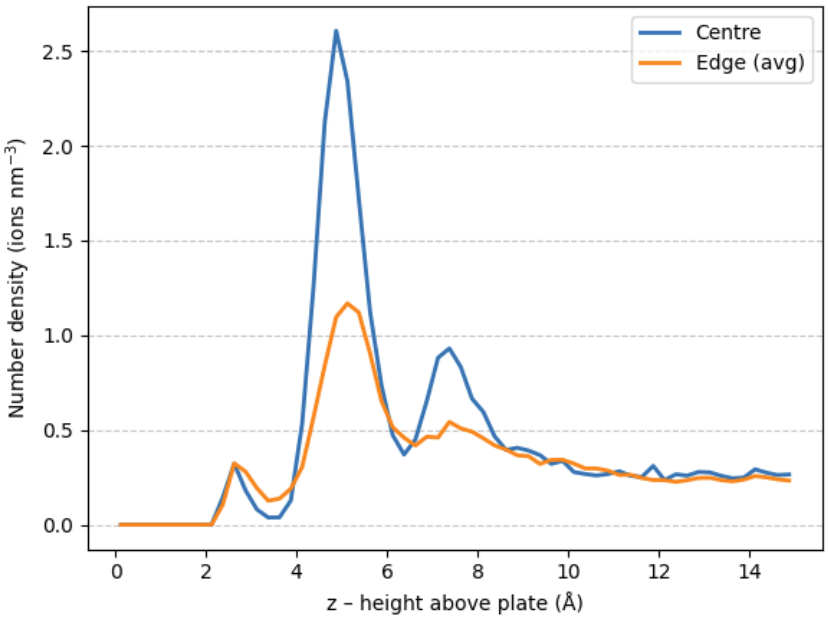

Figure 52: Region-resolved number density of K^+ ions (1 V).

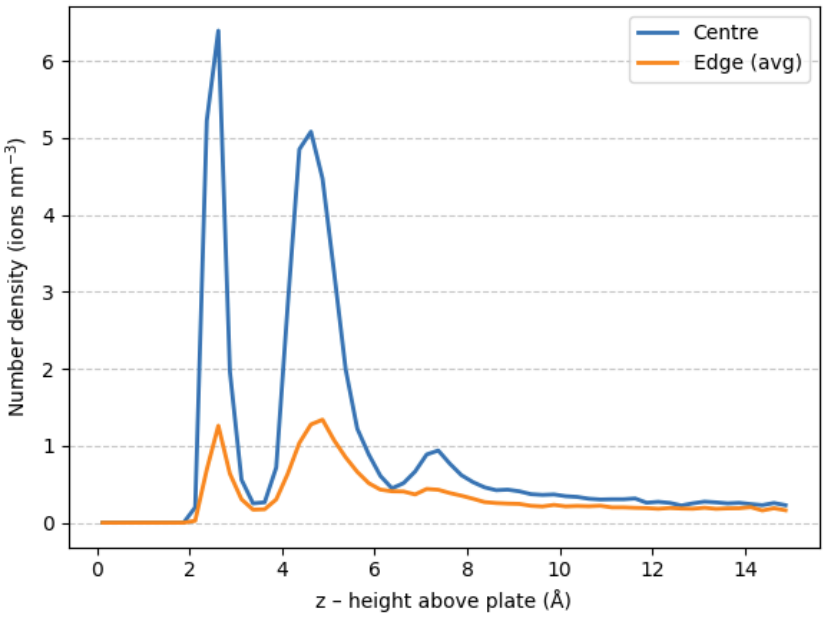

Figure 53: Region-resolved number density of K^+ ions (2 V).

In contrast, under CPM at 0 V, this trend reverses. The peak in the central hydrophilic region slightly exceeds that of the edge, and the distribution becomes more compressed. As the bias increases to 1 V and 2 V, this contrast becomes even more pronounced. At 1 V, the centre peak exceeds the edge by over a factor of two; at 2 V, the edge contribution is almost negligible while the centre exhibits multiple sharp features, including a double maximum around $z \approx 3$ Å and $z \approx 5$ Å, indicating multilayer structuring under strong fields.

Neutral CO_2, by contrast, displays the opposite spatial preference. Region-resolved one-dimensional z-profiles at 0 V (Fig. 54) show that CO_2 accumulates along the lateral edges of the hydrophilic plate rather than in the centre. While the central region exhibits a

broad and nearly flat profile, with concentrations barely exceeding 0.05 M near $z \approx 6$ Å, the edges display much sharper and more intense accumulation bands, reaching up to nearly 1.2 M. We believe this lateral segregation arises because CO_2, being uncharged, is disfavoured in regions of strong cation–anion correlations and instead tends to populate the less crowded edge corridors, where the local electric field is weaker and hydration environments may be more accommodating.

Thus far, we have systematically examined the spatial organization of K^+, HCO_3^-, and CO_2 within the confined electrolyte environment, uncovering how their distributions vary with applied potential and lateral surface patterning. By analyzing both averaged and region-resolved profiles, we identified key phenomena such as ion layering, electrostatic exclusion, and edge-enhanced CO_2 enrichment. In the subsequent section, we extend this molecular-scale understanding toward the functional level, drawing connections to experimentally observed electrochemical behavior and the design principles of CO_2 electrolyzers and fuel cell architectures.

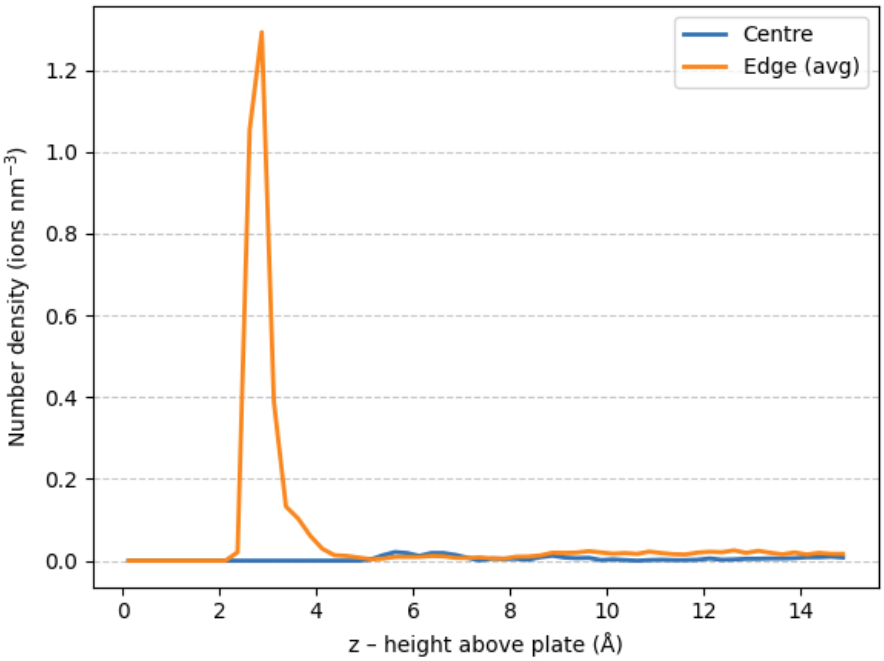

Figure 54: Region-resolved number density of CO_2(0V)

5.2.6 Consistencies with CO_2RR Experiments

Hydrophobic Interfaces Foster Triple-Phase CO_2 Enrichment Our simulations indicate that CO_2 molecules preferentially accumulate along the edges of the patterned surface, where a hydrophobic strip borders the aqueous electrolyte region. This edge-rich CO_2 distribution is localized at triple-phase boundaries (TPBs)—at the interface of hydrophobic and hydrophilic domains.

Such behavior closely parallels recent findings that strategic hydrophobic/hydrophilic patterning can modulate the CO_2 microenvironment. For instance, Wang et al. [53] showed that adding hydrophobic components (e.g., PTFE) to a gas diffusion electrode (GDE) causes water to recede and form gas–solid–liquid TPBs, thereby enriching CO_2 at specific catalyst sites. Their molecular dynamics simulations confirmed that hydrophobic surfaces repel H_2O and create CO_2-rich pockets along the triple-phase junctions, leading to higher local CO_2 concentrations.

This is consistent with our observations: the hydrophobic strip in our model effectively "funnels" CO_2 into interfacial regions, increasing its local availability where the catalyst, gas, and electrolyte meet. By fostering these CO_2-enriched TPBs, the patterned interface in our system could enhance reactant supply and suppress flooding, analogous to the microenvironment engineering reported in literature.

Triple-Phase Boundary Engineering Enhances CO_2RR Performance The link between TPB formation and improved CO_2 reduction reaction (CO_2RR) performance is further supported by experimental studies on engineered electrode architectures. Shi et al. (2022) [45] demonstrated that deliberately increasing the length and stability of triple-phase contact in a catalyst layer dramatically boosts CO_2RR outcomes. In their work, a hierarchical porous Bi catalyst (Bi nanosheet arrays on Cu foam) was functionalized with a hydrophobic silane, yielding an electrode with efficient and stable triple-phase interfaces. This design achieved over 90% formate selectivity over a wide potential window and high current density, far outperforming a non-modified electrode. The remarkable gains were ascribed by the authors to the presence of abundant and stable TPBs, which in their view provided simultaneous access of CO_2, electrolyte (protons), and active sites, thereby facilitating the targeted reaction.

In our simulation, we likewise find that CO_2 tends to migrate away from regions of high K^+ concentration and instead accumulates at the periphery of those ionic clusters—effectively along the interface or "edge" of the electrolyte-rich zone. This lateral CO_2 migration means that reactive CO_2 is concentrated at the boundary where the electrolyte concentration drops off, which is precisely where triple-phase contact with the gas phase can occur. Such an edge-driven enrichment aligns with the hypothesis that maximizing TPB length (for example, along the edges of porous structures or at electrolyte–gas boundaries) leads to greater CO_2 availability for reaction.

In essence, our findings mirror the experimental trend: structuring an electrode to promote more extensive TPBs, whether by micro-porosity and hydrophobic coatings in experiments or by patterned wetting properties in our model, tends to improve CO_2RR by locally increasing CO_2 concentration and reactant accessibility at active sites. This agreement not only validates our model's depiction of CO_2 piling up near hydrophobic edges, but also suggests that extending such triple-phase interface regions in practical systems could be a viable strategy to boost performance.

Parallels with Fuel Cell TPB Optimization The critical role of triple-phase boundaries is well-established in other electrochemical systems like fuel cells, and our results resonate with those principles. In solid-oxide and polymer electrolyte fuel cells, the electrochemical reactions occur exclusively at TPBs where an electron-conducting phase, an ion-conducting electrolyte, and the gaseous fuel/oxidant meet. Because these sites are the only places where all reactants and charges converge, the TPB length (or density) directly governs the reaction rate and overall performance.

In fact, even slight increases in TPB density can significantly enhance cell output; for example, Amitai et al. (2017) [5] showed that optimizing a porous electrode's grain sizes and morphology could triple the available TPB length, potentially boosting the electrochemical reaction rates by over 300%. These studies highlight that more and longer TPBs equate to more active sites and better mass/charge transfer, which in turn improves efficiency.

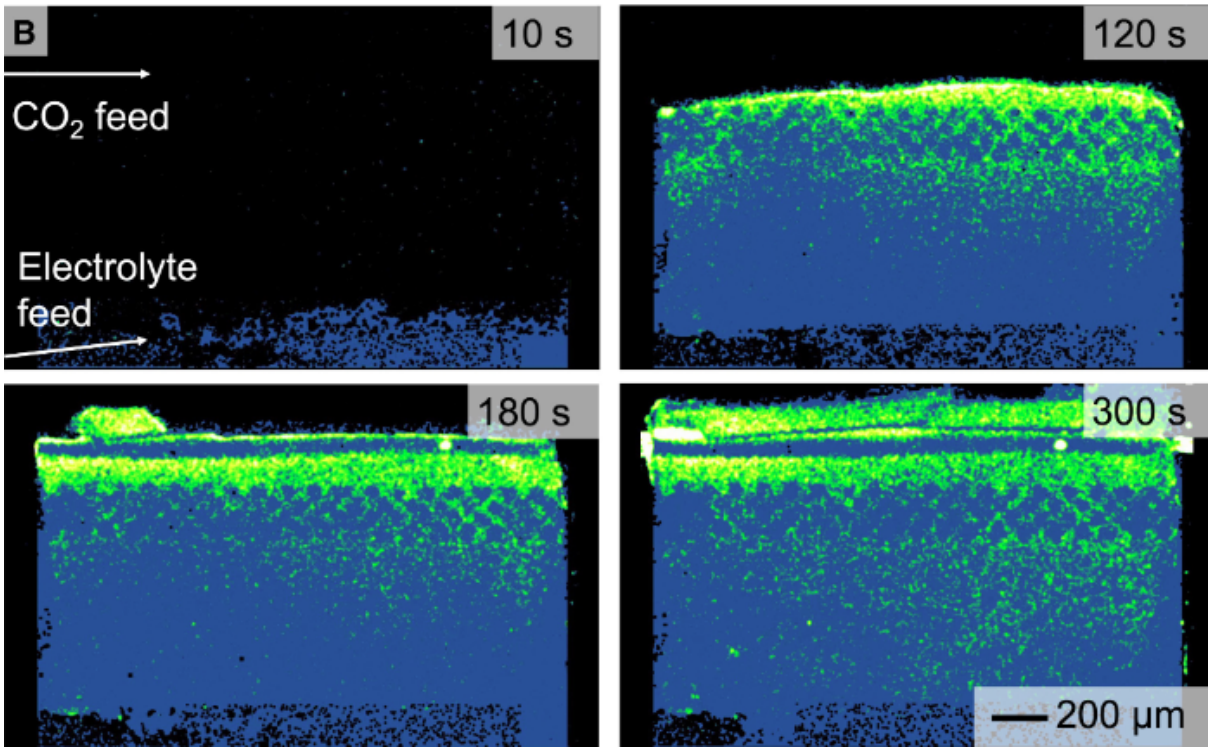

Figure 55: CLSM experimental images showing electrolyte breakthrough to the gas side after 180 s. The region exhibiting the highest reactivity was consistently observed near the triple-phase boundary (TPB)[9].

Experimental Evidence of TPB-Localized Activity Finally, it is insightful to compare our simulation predictions with direct experimental observations of where CO_2 reduction actually takes place in gas-fed systems. A recent study by Brosch et al. (2025) [9] employed a microfluidic CO_2 electrolyzer with spatially resolved analysis to visualize the formation of CO within a GDE catalyst layer. They found that the active reaction zones, where CO was generated, were not uniformly spread through the catalyst, but rather concentrated along the triple-phase boundaries in the porous electrode. Operando visualization images from their work (Fig. 55) clearly highlight these TPB-rich zones as CO generation hotspots.

In other words, the gas–liquid–solid junctions emerged as the primary sites of CO_2 conversion, while regions lacking one of the phases were comparatively inactive. This experimental insight aligns remarkably well with our findings of CO_2 accumulating at TPB-rich edge regions. Notably, our simulations further reveal that increasing the applied cathodic potential enhances CO_2 concentration specifically at these interfacial edge zones, indicating that the electric field reinforces reactant localization at TPBs.

This voltage-dependent accumulation provides additional support for the idea that TPBs are not only geometrically favorable but also electrostatically primed for enhanced CO_2 adsorption and reduction. It confirms the notion that having CO_2 and electrolyte in simultaneous contact with the catalyst (as occurs at the three-phase interface) is crucial for the reaction to proceed.

Indeed, it is broadly recognized that TPBs are the electrochemically active sites in heterogeneous electrode systems, and the work of Brosch et al. provides visual affirmation of this principle for CO_2RR. This convergence of modeling and experiment strengthens

our interpretation of the mechanism: the hydrophobic strip in our system creates a network of triple-phase contact lines that serve as hot-spots for CO_2 reduction, analogous to the active sites seen in *operando* visualizations. By connecting these dots, we can confidently state that strategies enhancing TPB areas, through material design or wettability engineering, are validated both by our molecular-level results and by macroscale experimental evidence as effective routes to improve CO_2 electroreduction performance.

5.3 Discussion

Our molecular dynamics simulations reveal a pronounced field-driven reorganization of ions, water, and CO_2 in the nanopore. Under an applied voltage, K^+ and HCO_3^- ions form stratified layers at the charged walls, creating a classic electric double layer. Cations (K^+) accumulate densely at the negatively charged surface. In fact, at 2 V bias they begin to partially shed hydration and adsorb directly onto lattice sites of the electrode, while anions (HCO_3^-) are largely repelled from the cathode and shifted outward into the diffuse layer. Notably, when comparing fixed-charge (NOP) and constant-potential (CPM) simulations at 0 V, a clear lateral redistribution of K^+ emerges. Under NOP, potassium accumulates preferentially along the edges of the hydrophilic plate, whereas under CPM, the peak density shifts toward the center. This contrast highlights the importance of including potential-dependent polarization in order to accurately capture lateral field heterogeneity and ion response, even in the absence of net charge.

Water molecules simultaneously align their dipoles in response to the field. Orientation profiles show that at higher voltages, a greater fraction of water molecules has its hydrogen atoms (positive end) turned toward the negative electrode, indicating dipole alignment with the electric field. This structuring of the interfacial water layer reinforces the electric double layer, creating a polarized solvent environment that strongly couples to ion behavior and further modifies local field distributions near the surface.

One conspicuous consequence of this interfacial restructuring is the behavior of CO_2 in the presence of a high-ion, high-field environment. The strong ion–water interactions "salt out" CO_2 from the electrolyte [63], decreasing its solubility in the bulk liquid and prompting a spatial redistribution of CO_2 molecules. In our simulations, CO_2 is observed to migrate away from the highly ionic regions and concentrate instead at their peripheries—essentially accumulating along the boundary between hydrophilic and hydrophobic region. These are precisely the locations of the triple-phase boundaries where solid, liquid, and gas meet. Notably, the CO_2 density at the negatively charged wall rises dramatically with applied bias (from roughly 0.5 M with no bias to nearly 3 M at 2 V), signifying enhanced CO_2 uptake at the interface under the electric field. This increase reflects the field-induced image-charge attraction of the quadrupolar CO_2 molecules to the cathode surface, which lowers the free energy barrier for CO_2 adsorption and effectively traps CO_2 in the interfacial region.

Importantly, the CO_2 does not distribute uniformly across the interface. 2D concentration maps show that under bias CO_2 organizes into patches and bands localized at the edges of the wetted regions, aligning with areas of concentrated negative surface charge on the electrode. In other words, CO_2 preferentially resides at the gas-liquid-solid contact lines, where the liquid film thins and the local electrostatic environment favors CO_2 retention.

Integrating these findings, a clear picture of interfacial restructuring in the CO_2–$KHCO_3$ system emerges. The applied electric field induces a highly structured double

layer (with K^+ and HCO_3^- layering) and aligns the water dipoles, while simultaneously expelling CO_2 from the ion-rich bulk and concentrating it at the edge of the spreading electrolyte. Such a configuration is highly significant. It suggests that ionic conductivity and CO_2 accessibility can coexist at the nanoscale under field control. In fact, this behavior echoes what experimental studies of gas-fed interfaces have hinted. For example, operando visualization in gas diffusion electrodes shows that CO_2 (and its reduction products) tend to concentrate near triple-phase boundaries in the catalyst layer, rather than deep in the flooded regions. Likewise, designs that maximize triple-phase boundary areas—via porous hydrophobic structures—are known to improve CO_2 utilization and reaction rates, which is consistent with our observation that CO_2 piles up at the electrolyte's edge. Our simulations now provide a molecular-level rationale for these observations.

6 Conclusion

This thesis has investigated the molecular-scale mechanisms by which applied surface potentials influence wettability and species distribution in confined nanoporous environments, with a specific focus on electrochemical CO_2 reduction (CO_2RR) systems. Through atomistic simulations using the Constant Potential Method (CPM), this study has illuminated how field-driven interfacial structuring governs the behavior of water, ions, and CO_2 near charged surfaces and triple-phase boundaries. The simulations revealed that electrode polarization induces a reorganization of the electrolyte interface, characterized by ion layering and water dipole alignment. Importantly, CO_2 was found to accumulate preferentially at the gas–liquid–solid contact lines, where local electric fields and geometric confinement promote its retention. These findings emphasize that triple-phase boundaries (TPBs) are not merely geometric features but play an active role in controlling reactant distribution under bias.

Beyond revealing these nanoscale phenomena, this thesis underscores the indispensable role of molecular dynamics in electrochemical interface modeling. Conventional continuum models fail to capture discrete ion structuring, oscillatory potentials, and image-charge effects that are essential for accurate descriptions of voltage-dependent wetting and species localization. By explicitly resolving the atomic-scale interactions between the electrode, solvent, and solutes, MD provides critical insight into interfacial phenomena that directly impact electrochemical performance. The implications of these results extend to the rational design of CO_2RR devices. The ability to maintain both high ionic conductivity and localized CO_2 availability under applied bias suggests that tailoring surface chemistry and electrode potential can be a powerful strategy to optimize conversion rates and suppress side reactions. Moreover, the observed behavior aligns closely with experimental findings in gas-fed electrolyzers, where CO_2 activity is often concentrated at TPBs, validating the predictive relevance of molecular simulations.

Looking ahead, future work should extend this framework by incorporating dynamic operating regimes such as oscillating fields, potential sweeps, and periodic electrolyte replenishment which can be studied at the atomistic level; however, due to the significant time-scale mismatch between these processes and accessible MD simulation windows, they can more practically be investigated by "freezing" the system at representative stages of the cycle and performing steady-state simulations for each condition. Exploring the effects of pore geometry and surface roughness could also reveal how confinement-induced field enhancement or spatial heterogeneity modulates interfacial reactivity. Additionally, future studies could examine the role of co-solvents, alternative ionic species, and pH gradients to simulate complex operational environments. Beyond atomistic simulations, the accuracy of mean-field continuum models could be improved by importing parameters like spatially resolved dielectric profiles and interfacial ion–surface exclusion distances extracted from MD. These parameters can refine Poisson–Nernst–Planck-type models to more accurately capture the influence of confinement and surface chemistry on macroscopic transport. On a broader scale, coupling these simulations to continuum models for mass transport or integrating them with data-driven approaches such as machine learning may accelerate the discovery of optimized electrode designs. Finally, validating these molecular insights against *operando* experimental techniques, such as *in situ* spectroscopy or electrochemical microscopy, will be essential to confirm their applicability and guide the development of high-efficiency CO_2 conversion technologies. This research highlights how bridging fundamental molecular behavior with device-scale performance

metrics can advance both scientific understanding and technological innovation in the field of electrochemical CO_2 conversion.

A Simulation Parameters

A.1 System Composition and Justification

Table 2: Summary of simulation composition and design rationale

Quantity	**Value Used in Simulation**	**Rationale**
Simulation box dimensions (Å)	x: -57.1032 to $+57.1032$ y: -20.394 to $+20.394$ z: -53.0244 to $+53.0244$	Box constructed as an integer multiple of Au lattice constant (4.0788 Å) to maintain FCC structure and avoid atomic overlaps under periodicity.
Total fluid volume	2.37×10^{-19} L	Computed from box dimensions in $Å^3$; used to calculate molar concentrations.
Water (SPC/E)	4990 molecules (55.5 M)	Replicates standard bulk water density ($\sim$0.99 g/cm^3) at 298 K under confined conditions.
Potassium ions (K^+)	45 ions (0.5 M[bulk])	–
Bicarbonate ions (HCO_3^-)	45 ions (0.5 M[bulk])	1:1 stoichiometry with K^+ ensures electroneutrality; common experimental choice for CO_2RR.
Carbon dioxide (CO_2)	12 molecules (0.075 M)	Henry's law solubility of CO_2 in 0.5 M $KHCO_3$ at 298 K and 1 bar yields $\sim$9 molecules; increased to 12 to enhance statistical sampling.
Wall structure	Two slabs of Au(100), 3 atomic layers each	Thin but electronically bulk-like; sufficient to screen image charges and mimic electrochemical surfaces.
Boundary conditions	Periodic in x and y; confined in z	Enables slab geometry; avoids unphysical dipole artifacts in confined direction while maintaining lateral homogeneity.

A.2 Wall Surface Functionalisation Parameters

Table 3: Lennard-Jones parameters used for chemically patterned wall surfaces

Region (along x)	**Atom type**	**LJ ε (kcal/-mol)**	**LJ σ (Å)**	**Justification / Source**
Hydrophilic core (-20.394 Å $\leq x \leq +20.394$ Å)	Au_{phil}	5.290	2.951	Heinz et al. (2008)[19]
Hydrophobic edges ($x < -20.394$ Å or $x > +20.394$ Å)	Hydrophobic additive	0.066	3.50	The values were selected based on hydrophobic parameters commonly used in research studies. The primary objective was to achieve sufficient hydrophobicity; therefore, only the parameter range was considered relevant [55, 10]

A.3 Atom Type Parameters Used in Simulations

Table 4: Lennard-Jones and charge parameters used in the simulation

Atom Type	ε (kcal/mol)	σ (Å)	q (e)	**Justification / Notes**
OW	0.1550	3.16557	–0.8476	Matches experimental water density, vaporization enthalpy[6].
HW	0	0	+0.4238	–
C (CO_2)	0.0550	2.80	+0.6512	Optimized to match CO_2 solubility in water[54].
O (CO_2)	0.1590	3.05	–0.3256	–
K^+	0.1000	3.396	+1.000	Reproduces hydration free energy with SPC/E water[27]
C (HCO_3^-)	0.1094	3.399	+0.823	Zeebe [61]
O (HCO_3^-)	0.1700	3.000	–0.620	–
H (HCO_3^-)	0.0157	2.500	+0.143	–
Au_{phil}	5.290	2.951	+0.05	Heinz et al.[19]
Au_{phob}	0.066	3.500	0.00	–

B Lennard–Jones Potential

The Lennard–Jones (LJ) potential is a commonly used model to describe short-range interactions between non-bonded atoms or molecules (Figure 56). It accounts for two main contributions[2]:

- A repulsive term ($\propto r^{-12}$) arising from Pauli repulsion when electron clouds overlap.
- An attractive term ($\propto r^{-6}$) representing van der Waals dispersion forces due to induced dipole interactions.

The potential between two particles i and j separated by a distance r_{ij} is:

$$U_{\mathrm{LJ}}(r_{ij}) = 4\epsilon_{ij}\left[\left(\frac{\sigma_{ij}}{r_{ij}}\right)^{12} - \left(\frac{\sigma_{ij}}{r_{ij}}\right)^{6}\right],$$

where:

ϵ_{ij}**:** Depth of the potential well, indicated in Figure 56; measures interaction strength.

σ_{ij}**:** Distance at which the potential crosses zero (see Figure 56); related to effective particle size.

The potential minimum occurs at:

$$r_{\min} = 2^{1/6}\sigma_{ij}, \quad U_{\mathrm{LJ}}(r_{\min}) = -\epsilon_{ij}.$$

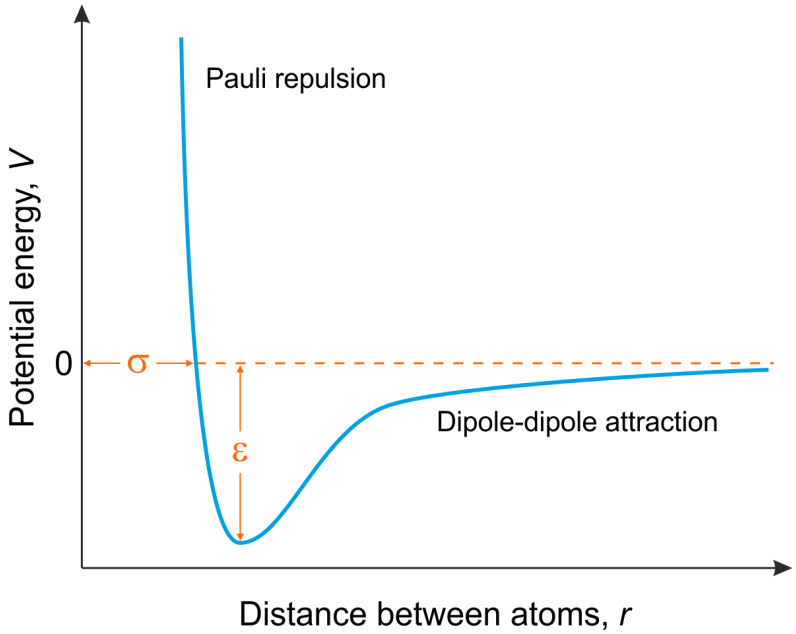

Figure 56: Graphical representation of the Lennard–Jones potential. The parameter σ is the zero-crossing distance, and ϵ is the depth of the potential well. The steep rise at short range corresponds to Pauli repulsion, while the long-range tail reflects van der Waals attraction[1].

C What is MD?

Molecular Dynamics (MD) is a computational technique used to model the time evolution of a system of atoms or molecules by integrating Newton's equations of motion. At its core, the method follows a simple cycle:

1. **Initialization**: Each atom is assigned an initial position and velocity. Positions are typically generated from a packing algorithm, while velocities are drawn from the Maxwell–Boltzmann distribution corresponding to the target temperature.

2. **Force calculation**: Interatomic forces are derived from a potential energy function $U(\mathbf{r})$(which are derived from interactions such as Coulombic and van der Waals), where the force on atom i is
$$\mathbf{F}_i = -\frac{\partial U}{\partial \mathbf{r}_i}.$$

3. **Integration of motion**: Using a discrete time step Δt, atomic positions and velocities are updated according to Newton's second law. Algorithms such as the velocity-Verlet scheme are commonly used:
$$\mathbf{r}_i(t+\Delta t) = \mathbf{r}_i(t) + \mathbf{v}_i(t)\Delta t + \frac{\mathbf{F}_i(t)}{2m_i}(\Delta t)^2,$$
$$\mathbf{v}_i(t+\Delta t2) = \mathbf{v}_i(t) + \frac{\mathbf{F}_i(t)}{2m_i}\Delta t,$$
$$\mathbf{v}_i(t+\Delta t) = \mathbf{v}_i(t+\Delta t2) + \frac{\mathbf{F}_i(t+\Delta t)}{2m_i}\Delta t.$$

4. **Iteration**: Steps (2) and (3) are repeated until the desired simulation time is reached. Along the trajectory, properties such as density profiles, diffusion coefficients, or structural correlations can be extracted by averaging over time.

Conceptually, MD provides a numerical microscope into molecular motion, bridging the gap between quantum-scale interactions (treated here through force fields) and experimentally observable properties.

D Nosé–Hoover Thermostat

The Nosé–Hoover thermostat is an extended–system method that enables molecular dynamics simulations to sample the canonical (NVT) ensemble. Unlike simple velocity–rescaling approaches, Nosé–Hoover generates not only the correct average temperature but also the correct distribution of thermal fluctuations.

Extended Equations of Motion

In the Nosé–Hoover formulation, the phase space is enlarged by introducing an additional thermostat variable ζ, which acts as a generalized, time–dependent friction coefficient. The instantaneous phase–space vector becomes

$$\Gamma = (r_1, \ldots, r_N,\ p_1, \ldots, p_N,\ \zeta),$$

leading to a set of $(6N + 1)$ coupled differential equations of motion:

$$\dot{r}_i = \frac{p_i}{m_i}$$

$$\dot{p}_i = F_i - \zeta p_i$$

$$\dot{\zeta} = \frac{1}{Q}\left(\sum_{i=1}^{N} \frac{p_i \cdot p_i}{m_i} - N_f k_B T\right)$$

Here:

- r_i, p_i, m_i are the position, momentum, and mass of particle i,
- F_i is the force on particle i,
- N_f is the number of degrees of freedom,
- T is the target temperature,
- Q is the thermostat "mass" parameter controlling the strength of coupling to the heat bath.

Interpretation

The additional variable ζ provides a feedback mechanism:

- If the instantaneous kinetic energy exceeds the target value, $\zeta > 0$ introduces damping, reducing the system's velocities.
- If the kinetic energy is too low, $\zeta < 0$ accelerates the particles.

E Code

E.1 Simulation Code

```
read_restart snapshotwithAu.restart

# Neighbor list settings
neighbor 2.0 bin
neigh_modify every 1 delay 0 check yes

######################### Masses and Force Field ########################################################
include in.parameters

########################## Simulation Inputs ############################################################

variable ts equal 1 # fs = one timestep
variable Temp equal 298.15 # K
variable Press equal 1.0 # atm

variable N_dump equal 1000 # timesteps
variable N_move equal 50000 # timesteps
variable N_equi equal 2000000/${ts} # timesteps

# Define lattice structure
variable lattice_constant equal 4.0788 # For gold FCC (Source: CRC Handbook with XRD data)
variable l_xy equal 5 # A
variable l_z equal 18 # A
variable l_fluid equal 8 # A
variable xhi equal ${l_xy}*${lattice_constant}
variable xlo equal -${l_xy}*${lattice_constant}
variable yhi equal ${l_xy}*${lattice_constant}
variable ylo equal -${l_xy}*${lattice_constant}
variable zhi equal ${l_z}*${lattice_constant}
variable zlo equal -${l_z}*${lattice_constant}
variable lfluidlo equal -${l_fluid}*${lattice_constant}
variable lfluidhi equal ${l_fluid}*${lattice_constant}

# New variables for Triple Phase system
variable l_x_new equal 10
lattice fcc $(v_lattice_constant)

# Limit for the top and bottom wall region
variable l_z_wall equal zhi/$(v_lattice_constant)-2

region BOTWALL block -${l_x_new} ${l_x_new} -${l_xy} ${l_xy} -$(v_l_z-1) -${l_z_wall}
region TOPWALL block -${l_x_new} ${l_x_new} -${l_xy} ${l_xy} ${l_z_wall} $(v_l_z-1)

region WALL union 2 TOPWALL BOTWALL

create_atoms 11 region WALL

# Grouping information
group TOPWALL region TOPWALL
group BOTWALL region BOTWALL
group WALL type 11
```

```
52
53 ######################### Refining Gold Regions: Hydrophilic vs. Hydrophobic
       ##########################
54
55 # Define regions for gold in contact with the fluid:
56 region gold_hydrophilic_top block -${l_xy} ${l_xy} -${l_xy} ${l_xy} ${l_z_wall} $(v_l_z-1)
57 region gold_hydrophilic_bot block -${l_xy} ${l_xy} -${l_xy} ${l_xy} -$(v_l_z-1)
       -${l_z_wall}
58 group gold_hydrophilic_top region gold_hydrophilic_top
59 group gold_hydrophilic_bot region gold_hydrophilic_bot
60 group gold_hydrophilic union gold_hydrophilic_top gold_hydrophilic_bot
61
62 # Subtract hydrophilic parts to define hydrophobic gold:
63 group gold_hydrophobic subtract WALL gold_hydrophilic
64
65 # Set the hydrophobic gold atoms to type 12:
66 set group gold_hydrophobic type 12
67
68 # Final cleanup and output
69 delete_atoms overlap 0.1 all all
70 run 0
71 dump 1 all custom 1 dump1.lammpstrj id type x y z
72 dump_modify 1 sort id
73 run 0
74 write_restart final_system.restart
75 write_data final_systemdata.data
```

Listing 1: LAMMPS input file for system creation

```
# distribute electrode atoms among all processors:
if "$(extract_setting(world_size) % 2) == 0" then "processors * * 2"

read_restart 11_2fs_nvt_conp_10ns_0V.lammpsrestart

# Neighbor list settings
neighbor 2.0 bin
neigh_modify every 1 delay 0 check yes

######################### Masses and Force Field ########################################################
include in.parameters

######################### Simulation Inputs #############################################################

variable ts equal 1 # fs = one timestep
variable Temp equal 298.15 # K
variable Press equal 1.0 # atm
variable potential index 0
variable N_dump equal 1000 # timesteps
variable N_move equal 2000000 # timesteps
variable N_equi equal 18000000/${ts} # timesteps

######################### Diagnostics files #############################################################

label potential_loop
dump dmp all custom ${N_dump} data/lammpstrj/1_1fs_dump_2ns_0V.lammpstrj id type x y z
dump_modify dmp sort 1
dump_modify dmp format line "%8d %5d %.3f %.3f %.3f"

# Box bounds
variable xlo equal xlo
variable xhi equal xhi
variable ylo equal ylo
variable yhi equal yhi
variable zlo equal zlo
variable zhi equal zhi

# Geometry definitions
variable lattice_constant equal 4.0788
variable l_xy equal 5
variable l_z equal 18
variable l_fluid equal 8
variable xhii equal ${l_xy}*${lattice_constant}
variable xloi equal -${l_xy}*${lattice_constant}
variable yhii equal ${l_xy}*${lattice_constant}
variable yloi equal -${l_xy}*${lattice_constant}
variable zhii equal ${l_z}*${lattice_constant}
variable zloi equal -${l_z}*${lattice_constant}

# System state variables
variable mype equal pe
variable mytemp equal temp

# Compute wall positions
```

```
variable wall_zmin equal bound(WALL,zmin)
variable wall_zmax equal bound(WALL,zmax)

print ""
print "Box z-dimension (START) = ${zlo} ${zhi} Angstrom"
print ""

group phophil type 11 12

# Center-of-mass tracking
compute z_com_topwall TOPWALL reduce ave z
compute z_com_botwall BOTWALL reduce ave z

# Thermodynamic and electrostatic monitoring
compute myTemp FLUID temp
compute myPress all pressure myTemp
variable q atom q
compute qtopwall TOPWALL reduce sum v_q
compute qbotwall BOTWALL reduce sum v_q

region TOPHALF block v_xlo v_xhi v_ylo v_yhi 0 v_zhi
region BOTHALF block v_xlo v_xhi v_ylo v_yhi v_zlo 0
group TOPHALF region TOPHALF
group TOPFLUID subtract TOPHALF TOPWALL H2O
group BOTHALF region BOTHALF
group BOTFLUID subtract BOTHALF BOTWALL H2O
compute qtopfluid TOPFLUID reduce sum v_q
compute qbotfluid BOTFLUID reduce sum v_q

# Output averages
fix myat1 all ave/time 1000 10 10000 c_myTemp file data/1_1fs_temperature_2ns_0V.dat
fix myat2 all ave/time 1000 10 10000 v_mype file data/1_1fs_potentialenergy_2ns_0V.dat
fix myat3 all ave/time 1000 10 10000 c_z_com_topwall c_z_com_botwall file
    data/1_1fs_wallposition_2ns_0V.dat
fix myat4 all ave/time 100 1 100 c_qtopwall c_qbotwall c_qtopfluid c_qbotfluid file
    data/1_1fs_charge_2ns_0V.dat

thermo ${N_dump}
thermo_style custom step c_myTemp c_myPress etotal c_z_com_botwall c_z_com_topwall
    c_qbotwall c_qtopwall c_qtopfluid c_qbotfluid

######################### Relaxation Procedure
    ####################################################

group HCO3 type 1 4 6 7 8
group H20 type 3 9
group k type 5
group A_CO2 type 2 10
group FLUID union H20 k A_CO2

fix shk H2O shake 1.0e-6 1000 0 b 5 a 2

timestep 1
fix rnvt1 TOPWALL rigid single force * off off on torque * off off off
fix mom1 TOPWALL momentum 1 linear 1 1 0 angular

fix conp1 BOTWALLPHILIC electrode/conp $(v_potential) 1.805 couple TOPWALLPHILIC
    $(-1*v_potential) symm on algo cg 1e-5
```

```
fix rnvtsmall HCO3 rigid/nvt/small molecule temp ${Temp} ${Temp} $(100.0*dt)
fix nvt1 FLUID nvt temp ${Temp} ${Temp} $(100.0*dt)

run $(v_N_move*1)

write_data data/lammpsdata/1_1fs_nvt_aveforce_2ns_0V.lammpsdata
write_restart data/lammpsrestart/1_1fs_nvt_aveforce_2ns_0V.lammpsrestart

undump dmp
unfix myat1
unfix myat2
unfix myat3
unfix myat4

dump dmp all custom ${N_dump} data/lammpstrj/1_2fs_dump_10ns_0V.lammpstrj id type x y z
dump_modify dmp sort 1
dump_modify dmp format line "%8d %5d %.3f %.3f %.3f"

fix myat1 all ave/time 1000 10 10000 c_myTemp file data/1_2fs_temperature_10ns_0V.dat
fix myat2 all ave/time 1000 10 10000 v_mype file data/1_2fs_potentialenergy_10ns_0V.dat
fix myat3 all ave/time 1000 10 10000 c_z_com_topwall c_z_com_botwall file
    data/1_2fs_wallposition_10ns_0V.dat
fix myat4 all ave/time 100 1 100 c_qtopwall c_qbotwall c_qtopfluid c_qbotfluid file
    data/1_2fs_charge_10ns_0V.dat
run $((v_N_equi)/2)

write_data data/lammpsdata/1_2fs_nvt_aveforce_10ns_0V.lammpsdata
write_restart data/lammpsrestart/1_2fs_nvt_aveforce_10ns_0V.lammpsrestart

undump dmp
unfix myat1
unfix myat2
unfix myat3
unfix myat4

dump dmp all custom ${N_dump} data/lammpstrj/1_2fs_dump_20ns_0V.lammpstrj id type x y z
dump_modify dmp sort 1
dump_modify dmp format line "%8d %5d %.3f %.3f %.3f"

fix myat1 all ave/time 1000 10 10000 c_myTemp file data/1_2fs_temperature_20ns_0V.dat
fix myat2 all ave/time 1000 10 10000 v_mype file data/1_2fs_potentialenergy_20ns_0V.dat
fix myat3 all ave/time 1000 10 10000 c_z_com_topwall c_z_com_botwall file
    data/1_2fs_wallposition_20ns_0V.dat
fix myat4 all ave/time 100 1 100 c_qtopwall c_qbotwall c_qtopfluid c_qbotfluid file
    data/1_2fs_charge_20ns_0V.dat
run $((v_N_equi)/2)

write_data data/lammpsdata/1_2fs_nvt_aveforce_20ns_0V.lammpsdata
write_restart data/lammpsrestart/1_2fs_nvt_aveforce_20ns_0V.lammpsrestart
```

Listing 2: LAMMPS production run script using the Constant Potential Method (CPM) at 0 V

E.2 Analysis Code

```python
#!/usr/bin/env python3
"""
density_profile_linear_viewer.py
--------------------------------
1D concentration (molL) vs z for CO, K, HCO, HO using
MDAnalysis.analysis.lineardensity.LinearDensity.

Outputs interactive Plotly HTML.
"""

import json
from pathlib import Path
import numpy as np
import MDAnalysis as mda
from MDAnalysis.analysis.lineardensity import LinearDensity
from plotly.utils import PlotlyJSONEncoder

DZ = 0.25 # slab thickness in
NA = 6.022_140_76e23 # Avogadro's number

# Molar masses (g/mol)
MOLAR = {
    "CO2": 44.0095,
    "K": 39.0983,
    "HCO3": 61.0168,
    "H2O": 18.0153,
}

# Atom selections by type ID
SEL = {
    "CO2": "type 2 10",
    "K": "type 5",
    "HCO3": "type 1 4 6 7 8",
    "H2O": "type 3 9",
}

# Trajectories and data files
runs = [
    ("12CO2_NOP",
     "wallmovement_Nopotential_20ns_corrparaco2/data/lammpsdata/"
     "1_2fs_nvt_aveforce_20ns_corrparaco2.lammpsdata",
     "wallmovement_Nopotential_20ns_corrparaco2/data/lammpstrj/"
     "1_2fs_dump_20ns_corrparaco2.lammpstrj"),

    ("12CO2_0V",
     "wallmovement_0V_20ns_corrparaco2/data/lammpsdata/"
     "1_2fs_nvt_aveforce_20ns_0V_corrparaco2.lammpsdata",
     "wallmovement_0V_20ns_corrparaco2/data/lammpstrj/"
     "1_2fs_dump_20ns_0V_corrparaco2.lammpstrj"),
```

```
50
51      ("12CO2_1V",
52       "wallmovement_1V_20ns_corrparaco2/data/lammpsdata/"
53       "1_2fs_nvt_aveforce_20ns_1V_corrparaco2.lammpsdata",
54       "wallmovement_1V_20ns_corrparaco2/data/lammpstrj/"
55       "1_2fs_dump_20ns_1V_corrparaco2.lammpstrj"),
56
57      ("12CO2_2V",
58       "wallmovement_2V_20ns_corrparaco2/data/lammpsdata/"
59       "1_2fs_nvt_aveforce_20ns_2V_corrparaco2.lammpsdata",
60       "wallmovement_2V_20ns_corrparaco2/data/lammpstrj/"
61       "1_2fs_dump_20ns_2V_corrparaco2.lammpstrj"),
62  ]
63
64  profiles = {sp: {} for sp in MOLAR}
65  z_centres = None
66
67  for label, dataf, dumpf in runs:
68      print(f" {label}")
69      u = mda.Universe(dataf, dumpf,
70                       topology_format="DATA", format="LAMMPSDUMP")
71
72      Lz = u.dimensions[2]
73      half_z = Lz / 2
74
75      if z_centres is None:
76          nbins = int(np.ceil(Lz / DZ))
77          z_edges = np.linspace(-half_z, half_z, nbins + 1)
78          z_centres = 0.5 * (z_edges[:-1] + z_edges[1:])
79
80      for sp, selstr in SEL.items():
81          sel = u.select_atoms(selstr)
82          if sel.n_atoms == 0:
83              continue
84          ld = LinearDensity(sel, delta=DZ, axis='z')
85          ld.run()
86          rho = ld.results['z']['mass_density'] # g/L
87          conc = 1000.0 * rho / MOLAR[sp] # mol/L
88          profiles[sp][label] = conc.tolist()
89
90  print(" all trajectories processed")
91
92  # Generate Plotly HTML
93  species_opts = ''.join(f'<option value="{sp}">{sp}</option>'
94                         for sp in MOLAR)
95  run_labels = [lab for lab, *_ in runs]
96
97  html = f"""
98  <!doctype html>
99  <html>
100 <head>
```

```
  <meta charset="utf-8">
  <title>1D concentration profiles (LinearDensity)</title>
  <script src="https://cdn.plot.ly/plotly-2.32.0.min.js"></script>
</head>
<body>
  <h2>Concentration vs z</h2>
  <p>Select molecule:</p>
  <select id="species" style="font-size:16px;margin-bottom:1rem">
    {species_opts}
  </select>
  <div id="plot" style="width:900px;height:550px"></div>
  <script>
    const z = {json.dumps(z_centres.tolist())};
    const dataDict = {json.dumps(profiles, cls=PlotlyJSONEncoder)};
    const runs = {json.dumps(run_labels)};
    const traces = [];
    Object.keys(dataDict).forEach((sp, i) => {{
      runs.forEach(r => {{
        traces.push({{
          x: z,
          y: dataDict[sp][r],
          mode: 'lines',
          name: r,
          visible: i === 0
        }});
      }});
    }});
    const layout = {{
      xaxis: {{title: 'z []'}},
      yaxis: {{title: 'Concentration [M]'}},
      legend: {{orientation: 'h'}},
      margin: {{t:50,l:60,r:10,b:60}}
    }};
    Plotly.newPlot('plot', traces, layout);
    document.getElementById('species').addEventListener('change', e => {{
      const sp = e.target.value;
      let idx = 0;
      Object.keys(dataDict).forEach(s => {{
        runs.forEach(_ => {{
          traces[idx].visible = (s === sp);
          idx++;
        }});
      }});
      Plotly.react('plot', traces, layout);
    }});
  </script>
</body>
</html>"""

Path("density_profile_viewer_INBUILDMETHOD-CORRPARA.html").write_text(html,
    ↪ encoding="utf-8")
```

```
print(" HTML saved  density_profile_viewer.html")
```

Listing 3: Python code for computing and visualizing 1D molar concentration profiles

```
import numpy as np
import MDAnalysis as mda
import json
from pathlib import Path

from plotly.utils import PlotlyJSONEncoder
import plotly.graph_objects as go

NA = 6.02214076e23
dx = dz = 0.25 #

runs = [
    ("3oco2",
     "30co2_corrpara/data/lammpsdata/"
     "1_2fs_nvt_aveforce_20ns_1V.lammpsdata",
     "30co2_corrpara/data/lammpstrj/"
     "1_2fs_dump_20ns_1V.lammpstrj")
]

all_data = {}
x_centers = z_centers = None

for label, datafile, dumpfile in runs:
    u = mda.Universe(datafile, dumpfile,
                     topology_format="DATA", format="LAMMPSDUMP")
    water = u.select_atoms("type 2") # Adjust type if needed

    if x_centers is None:
        Lx, Ly, Lz = u.dimensions[:3]
        half_x, half_z = Lx / 2, Lz / 2
        x_edges = np.arange(-half_x, half_x + dx, dx)
        z_edges = np.arange(-half_z, half_z + dz, dz)
        x_centers = x_edges[:-1] + dx / 2
        z_centers = z_edges[:-1] + dz / 2
        slab_area = Ly * dx
        voxel_vol = slab_area * dz

    counts = np.zeros((len(x_edges) - 1, len(z_edges) - 1))
    for ts in u.trajectory:
        xs = water.positions[:, 0] - half_x
        zs = water.positions[:, 2] - half_z
        H, _, _ = np.histogram2d(xs, zs, bins=[x_edges, z_edges])
        counts += H

    n_frames = len(u.trajectory)
    number_density = counts / (voxel_vol * n_frames)
    conc = number_density * (1e27 / NA) # mol/L
    all_data[label] = conc.tolist()
```

```
49
50 #  HTML with embedded Plotly and JS
51 html_template = f"""
52 <html>
53 <head>
54     <title>CO Concentration Viewer</title>
55     <script src="https://cdn.plot.ly/plotly-latest.min.js"></script>
56 </head>
57 <body>
58     <h2>Interactive CO Concentration (xz)</h2>
59     <select id="run-dropdown" style="font-size:16px;">
60         {''.join(f'<option value="{label}">{label}</option>' for label, *_ in
               ↪ runs)}
61     </select>
62
63     <div id="heatmap" style="width:600px;height:600px;"></div>
64     <div id="slice" style="width:1500px;height:500px;"></div>
65
66 <script>
67 const allConcMaps = {json.dumps(all_data, cls=PlotlyJSONEncoder)};
68 const x_centers = {json.dumps(x_centers.tolist())};
69 const z_centers = {json.dumps(z_centers.tolist())};
70
71 function makeHeatmap(label) {{
72     const z = allConcMaps[label];
73     const transposed = z[0].map((_, i) =>
74         z.map(row => row[i] < 3.0 ? row[i] : null));
75     const trace = {{
76         x: x_centers,
77         y: z_centers,
78         z: transposed,
79         type: 'heatmap',
80         colorscale: 'Viridis',
81         hovertemplate: 'x=%{{x:.2f}} <br>z=%{{y:.2f}} <br>conc=%{{z:.2f}} M',
82         colorbar: {{ title: 'Conc [M]' }}
83     }};
84     const layout = {{
85         title: 'CO Heatmap  ' + label,
86         xaxis: {{ title: 'x []' }},
87         yaxis: {{ title: 'z []', scaleanchor: 'x', scaleratio: 1 }}
88     }};
89     Plotly.newPlot('heatmap', [trace], layout);
90
91     document.getElementById('heatmap').on('plotly_click', function(event) {{
92         const xVal = event.points[0].x;
93         const idx = x_centers.map(x => Math.abs(x - xVal));
94         const ix = idx.indexOf(Math.min(...idx));
95         const yvals = allConcMaps[label][ix];
96         const sliceTrace = {{
97             x: z_centers,
98             y: yvals,
```

```
            mode: 'lines+markers',
            name: 'x = ' + x_centers[ix].toFixed(2) + ' '
        }};
        const sliceLayout = {{
            title: '1D Concentration at x = ' + x_centers[ix].toFixed(2) + ' ',
            xaxis: {{ title: 'z []' }},
            yaxis: {{ title: 'Concentration [M]' }}
        }};
        Plotly.newPlot('slice', [sliceTrace], sliceLayout);
    }});
}}

document.getElementById("run-dropdown").addEventListener("change", function(e) {{
    makeHeatmap(e.target.value);
}});
makeHeatmap("{runs[0][0]}");
</script>
</body>
</html>
"""

Path("30co2-2dNOTcorrpara.html").write_text(html_template, encoding='utf-8')
print("HTML saved: CO2-C_interactive_viewerCORRPARA.html")
```

Listing 4: Python code for computing and visualizing 2D molar concentration profiles

References

[1] Lennard-jones potential. https://glossary.periodni.com/glossary.php?en=Lennard-Jones+potential. Accessed: 2025-08-10.

[2] Lennard-jones potential. https://en.wikipedia.org/wiki/Lennard-Jones_potential. Accessed: 2025-08-10.

[3] Encyclopedia of microfluidics and nanofluidics — front matter. https://www.cytofluidix.com/wp-content/uploads/2015/06/Encyclopedia-Front-Matter.pdf, 2015. Accessed: 2024-03-22.

[4] Ludwig J. V. Ahrens-Iwers, Mathijs Janssen, Shern R. Tee, and Robert H. Meißner. Electrode: An electrochemistry package for atomistic simulations. *Journal of Chemical Physics*, 157(8):084801, 2022. Published online 25August 2022.

[5] Shahar Amitai, Antonio Bertei, and Raphael Blumenfeld. Theory-based design of sintered granular composites triples three-phase boundary in fuel cells. *Physical Review E*, 96(5):052903, 2017.

[6] H. J. C. Berendsen, J. R. Grigera, and T. P. Straatsma. The missing term in effective pair potentials. *The Journal of Physical Chemistry*, 91(24):6269–6271, 1987.

[7] BioLogic. What is CO_2 electrolysis? https://www.biologic.net/topics/what-is-co2-electrolysis/, n.d. Accessed: 2024-03-22.

[8] Mulatu Kassie Birhanu, Begüm Ünveroğlu Abdioglu, and Ahmet Uçar. Extrinsic and intrinsic factors for electrochemical reduction of carbon dioxide on heterogeneous metal electrocatalysts. *Catal. Sci. Technol.*, 15:262–317, 2025.

[9] Simon Brosch, Erik Häger, Oliver Frank, Philipp Scholz, Wolfgang Plischka, and Matthias Wessling. Visualization of CO formation at the triple-phase boundary in gas diffusion electrodes for ecCO_2RR. *Chem*, 11:102582, 2025.

[10] J.R. Choudhuri and P. Nath. Wetting transition of a nanodrop on switchable hydrophilic hydrophobic surfaces. *Surfaces and Interfaces*, 21:100628, 2020.

[11] Bert De Mot, Jonas Hereijgers, Miguel Duarte, and Tom Breugelmans. Influence of flow and pressure distribution inside a gas diffusion electrode on the performance of a flow-by CO_2 electrolyzer. *Chemical Engineering Journal*, 378:122224, 2019.

[12] Jiapei Du, Annan Zhou, Yu Zhong, and Shui-Long Shen. Molecular simulation on CO_2 adsorption heterogeneity in montmorillonite nanopores with different surface charges in presence of water. *Chemical Engineering Journal*, 482:148958, 2024.

[13] European Environment Agency. Climate change mitigation — reducing emissions. https://www.eea.europa.eu/en/topics/in-depth/climate-change-mitigation-reducing-emissions, 2024. Accessed: 2024-03-22.

[14] European Environment Agency. Policies and measures (pam) database. https://pam.apps.eea.europa.eu/, 2024. Accessed: 2024-03-22.

[15] Marco Favaro, Hai Xiao, Tao Cheng, William A. Goddard III, Junko Yano, and Ethan J. Crumlin. Subsurface oxide plays a critical role in CO_2 activation by Cu(111) surfaces to form chemisorbed CO_2, the first step in reduction of CO_2. *Proceedings of the National Academy of Sciences*, 114(26):6706–6711, 2017.

[16] Lipei Fu, Zhangkun Ren, Wenzhe Si, Qianli Ma, Weiqiu Huang, Kaili Liao, Zhoulan Huang, Yu Wang, Junhua Li, and Peng Xu. Research progress on co_2 capture and utilization technology, 12 2022.

[17] Guillermo Iván Guerrero-García, Enrique González-Tovar, Martín Chávez-Páez, Jacek Kłos, and Stanisław Lamperski. Quantifying the thickness of the electrical double layer neutralizing a planar electrode: The capacitive compactness. *Physical Chemistry Chemical Physics*, 20:262–275, 2017.

[18] Remco Hartkamp, Bertrand Siboulet, Jean-François Dufrêche, and Benoit Coasne. Ion-specific adsorption and electroosmosis in charged amorphous porous silica. *Physical Chemistry Chemical Physics*, 17:24683–24695, 2015.

[19] Hendrik Heinz, Richard A Vaia, Barry L Farmer, and Rajesh R Naik. Accurate simulation of surfaces and interfaces of face-centered cubic metals using 12-6 and 9-6 lennard-jones potentials. *The Journal of Physical Chemistry C*, 112(44):17281–17290, 2008.

[20] Thomas J. P. Hersbach, Ian T. McCrum, Dimitra Anastasiadou, Rianne Wever, Federico Calle-Vallejo, and Marc T. M. Koper. Alkali metal cation effects in structuring pt, rh, and au surfaces through cathodic corrosion. *ACS Applied Materials & Interfaces*, 10(45):39363–39379, 2018.

[21] W. A. Hika and A. R. Woldu. The impact of anode materials on the performance of electrochemical CO_2 reduction to carbon monoxide. *SN Applied Sciences*, 3:812, 2021.

[22] R.W. Hockney and J.W. Eastwood. *Computer Simulation Using Particles*. Taylor & Francis, New York, 1988.

[23] International Energy Agency. An energy sector roadmap to carbon neutrality in china. https://www.iea.org/reports/an-energy-sector-roadmap-to-carbon-neutrality-in-china, 2021. IEA, Paris. Licence: CC BY 4.0. Accessed: 2024-03-22.

[24] International Energy Agency. CO_2 capture and utilisation. https://www.iea.org/energy-system/carbon-capture-utilisation-and-storage/co2-capture-and-utilisation, 2024. Accessed: 2024-03-22.

[25] Evan Johnson and Sophia Haussener. Contrasting views of the electric double layer in electrochemical CO_2 reduction: Continuum models vs molecular dynamics. *The Journal of Physical Chemistry C*, 128(25):10450–10464, 2024.

[26] Christopher Jones and Andris Piebalgs. The role of ccus on the eu road to climate neutrality. https://data.europa.eu/doi/10.2870/30583, 2022. Accessed: 2024-03-22.

[27] In Suk Joung and Thomas E. Cheatham III. Determination of alkali and halide monovalent ion parameters for use in explicitly solvated biomolecular simulations. *The Journal of Physical Chemistry B*, 112(30):9020–9041, 2008. Received Jan 8, 2008; Revised Apr 30, 2008; Issue dated Jul 31, 2008.

[28] McLain E. Leonard, Michael J. Orella, Nicholas Aiello, Yuriy Román-Leshkov, Antoni Forner-Cuenca, and Fikile R. Brushett. On the role of electrode wettability in CO_2 electrolyzers that generate liquid products. *Journal of The Electrochemical Society*, 167(12):124521, aug 2020.

[29] Mengran Li, Mohamed Nazmi Idros, Yuming Wu, Thomas Burdyny, Sahil Garg, Xiu Song Zhao, Geoff Wang, and Thomas E. Rufford. The role of electrode wettability in electrochemical reduction of carbon dioxide. *J. Mater. Chem. A*, 9:19369–19409, 2021.

[30] David R. Lide. *CRC Handbook of Chemistry and Physics*. Taylor & Francis, 85th edition, 2004.

[31] Jiayi Lin, Yixiao Zhang, Pengtao Xu, and Liwei Chen. CO_2 electrolysis: Advances and challenges in electrocatalyst engineering and reactor design. *Materials Reports: Energy*, 3(2):100194, 2023.

[32] F. G. Mugele and J.-C. Baret. Electrowetting: from basics to applications. *Journal of Physics: Condensed Matter*, 17:R705–R774, 2005.

[33] Azeem Mustafa, Bachirou Guene Lougou, Yong Shuai, Zhijiang Wang, Samia Razzaq, Yanna Liang, and Mingbo Li. Theoretical insights into the factors affecting the electrochemical reduction of CO_2. *Sustainable Energy Fuels*, 4(9):4352–4369, 2020.

[34] Nathan T. Nesbitt, Thomas Burdyny, Hunter Simonson, Danielle Salvatore, Divya Bohra, Recep Kas, and Wilson A. Smith. Liquid–solid boundaries dominate activity of CO_2 reduction on gas-diffusion electrodes. *ACS Catalysis*, 10(23):14093–14106, 2020.

[35] Levi C. T. Pierce, Romelia Salomon-Ferrer, Cesar Augusto F. de Oliveira, J. Andrew McCammon, and Ross C. Walker. Routine access to millisecond time scale events with accelerated molecular dynamics. *Journal of Chemical Theory and Computation*, 8(9):2997–3002, 2012.

[36] Steve Plimpton. Fast parallel algorithms for short-range molecular dynamics. *Journal of Computational Physics*, 117(1):1–19, 1995.

[37] Jake W. Polster, Fikret Aydin, J. Pedro de Souza, Martin Z. Bazant, Tuan Anh Pham, and Zuzanna S. Siwy. Rectified and salt concentration dependent wetting of hydrophobic nanopores. *Journal of the American Chemical Society*, 144(26):11693–11705, 2022.

[38] Daniel J. Preston, Daniela L. Mafra, Nenad Miljkovic, Jing Kong, and Evelyn N. Wang. Scalable graphene coatings for enhanced condensation heat transfer. *Nano Letters*, 15(5):2902–2909, 2015.

[39] Zhen Qi, Ajay R. Kashi, Aya K. Buckley, John S. Miller, Jianchao Ye, Monika M. Biener, Alexandre C. Foucher, Eric A. Stach, Sichao Ma, Kendra P. Kuhl, and Juergen Biener. Effect of gold catalyst surface morphology on wetting behavior and electrochemical CO_2 reduction performance in a large-area zero-gap gas diffusion electrolyzer. *The Journal of Physical Chemistry C*, 126(46):19637–19646, 2022.

[40] Anthony Quinn, Rossen Sedev, and John Ralston. Influence of the electrical double layer in electrowetting. *The Journal of Physical Chemistry B*, 107(5):1163–1169, 2003.

[41] S. Realista, P. J. Costa, L. B. Maia, M. J. Calhorda, and P. N. Martinho. Mechanistic insights into the electrochemical reduction of CO to CO on Ni(salphen) complexes. *Inorganic Chemistry Frontiers*, 10(14):4175–4189, 2023.

[42] Hannah Ritchie and Max Roser. CO_2 emissions. *Our World in Data*, 2020. https://ourworldindata.org/co2-emissions.

[43] Alessandro Senocrate, Francesco Bernasconi, Daniel Rentsch, Kevin Kraft, Matthias Trottmann, Adrian Wichser, Davide Bleiner, and Corsin Battaglia. Importance of substrate pore size and wetting behavior in gas diffusion electrodes for CO_2 reduction. *ACS Applied Energy Materials*, 5(11):14504–14512, 2022.

[44] Rui Shi, Jing Guo, Xinyue Zhang, et al. Efficient wettability-controlled electroreduction of CO_2 to CO at Au/C interfaces. *Nature Communications*, 11:3028, 2020.

[45] Tianyi Shi, Dong Liu, Nan Liu, Ying Zhang, Hui Feng, and Qian Li. Triple phase interface engineered hierarchical porous electrode for CO_2 electroreduction to formate. *Advanced Science*, 9(30):e2204472, 2022.

[46] Alexander M. Smith, Alpha A. Lee, and Susan Perkin. Ion correlations drive charge overscreening and heterogeneous nucleation at solid–aqueous electrolyte interfaces. *Proceedings of the National Academy of Sciences*, 118(32):e2105154118, 2021.

[47] Fereshte Taherian, Frédéric Leroy, Lars-Oliver Heim, Elmar Bonaccurso, and Nico F. A. van der Vegt. Mechanism for asymmetric nanoscale electrowetting of an ionic liquid on graphene. *Langmuir*, 32(1):140–150, 2016.

[48] Fereshte Taherian, Frédéric Leroy, and Nico F. A. van der Vegt. Interfacial tension does not drive asymmetric nanoscale electrowetting on graphene. *Langmuir*, 31(16):4686–4695, 2015.

[49] Xiongwei Tian, Axel Tosello Gardini, Umberto Raucci, Hai Xiao, Yuqun Zhuo, and Michele Parrinello. Electrochemical potential-driven water dynamics control co_2 electroreduction at the ag/h_2o interface. *ChemRxiv*, 2025. Preprint, not peer-reviewed.

[50] United Nations Framework Convention on Climate Change. Summary of global climate action at cop 28. UNFCCC Publications, 2023. Published on 11 Dec 2023. Session: COP 28. Accessed: 2024-03-22.

[51] S. Vijay, W. Ju, S. Brückner, S.-C. Tsang, P. Strasser, and K. Chan. Unified mechanistic understanding of CO reduction to CO on transition metal and single atom catalysts. *Nature Catalysis*, 4(12):1024–1031, 2021.

[52] Ettore Virga, Evan Spruijt, Wiebe M. de Vos, and P. M. Biesheuvel. Wettability of amphoteric surfaces: The effect of ph and ionic strength on surface ionization and wetting. *Langmuir*, 34(50):15174–15180, 2018.

[53] Dan Wang, Junjun Mao, Chenchen Zhang, Jiawei Zhang, Junshan Li, Ying Zhang, and Yongfa Zhu. Modulating microenvironments to enhance CO_2 electroreduction performance. *eScience*, 3:100119, 2023.

[54] Dominika O. Wasik, H. Mert Polat, Mahinder Ramdin, Othonas A. Moultos, Sofia Calero, and Thijs J. H. Vlugt. Solubility of co in aqueous formic acid solutions and the effect of nacl addition: A molecular simulation study. *The Journal of Physical Chemistry C*, 126(45):19424–19434, 2022.

[55] Edward K. Watkins and William L. Jorgensen. Perfluoroalkanes: Conformational analysis and liquid-state properties from ab initio and monte carlo calculations. *The Journal of Physical Chemistry A*, 105(16):4118–4125, 2001.

[56] Lien-Chun Weng, Alexis T. Bell, and Adam Z. Weber. Modeling gas-diffusion electrodes for CO_2 reduction. *Phys. Chem. Chem. Phys.*, 20:16973–16984, 2018.

[57] Yuming Wu, Hesamoddin Rabiee, Xiu Song Zhao, Geoff Wang, and Yijiao Jiang. Insights into electrolyte flooding in flexible gas diffusion electrodes for CO_2 electrolysis: from mechanisms to effective mitigation strategies. *J. Mater. Chem. A*, 12:14206–14228, 2024.

[58] Zhenyu Xing, Longfei Hu, Daniel S. Ripatti, et al. Enhancing carbon dioxide gas-diffusion electrolysis by creating a hydrophobic catalyst microenvironment. *Nature Communications*, 12:136, 2021.

[59] Kailun Yang, Recep Kas, Wilson A. Smith, and Thomas Burdyny. Role of the carbon-based gas diffusion layer on flooding in a gas diffusion electrode cell for electrochemical CO_2 reduction. *ACS Energy Letters*, 6(1):33–40, 2021.

[60] I-Cheng Yeh and Max L Berkowitz. Ewald summation for systems with slab geometry. *The Journal of Chemical Physics*, 111(7):3155–3162, 1999.

[61] Richard E. Zeebe. On the molecular diffusion coefficients of dissolved CO_2, HCO_3^-, and CO_3^{2-} and their dependence on isotopic mass. *Geochimica et Cosmochimica Acta*, 75(9):2483–2498, May 2011.

[62] Juqin Zeng, Marco Fontana, Adriano Sacco, Daniele Sassone, and Candido F. Pirri. A study of the effect of electrode composition on the electrochemical reduction of CO_2. *Catalysis Today*, 397-399:463–474, 2022. SI:CCE-2021.

[63] X. Zhang, L. Zhang, T. Jin, Z.-J. Pan, Z.-N. Chen, Q. Zhang, and W. Zhuang. Salting in/salting out mechanism of carbon dioxide in aqueous electrolyte solutions. *Chinese Journal of Chemical Physics*, 30(6):811–816, 2017.